Homogenization and multi-scale analysis of locally resonant acoustic metamaterial plates

Lenders, T.

Award date:
2019

Master Thesis

HOMOGENIZATION AND MULTI-SCALE ANALYSIS OF LOCALLY RESONANT ACOUSTIC METAMATERIAL PLATES

Author
Tom Lenders - 0893926

Supervisors
dr. ir. V.G. Kouznetsova — Eindhoven University of Technology
ir. L. Liu — Eindhoven University of Technology

Eindhoven University of Technology
Department of Mechanical Engineering
Mechanics of Materials

Eindhoven, 5th December 2019

Graduation committee

prof. dr. ir. M.G.D. Geers	Department of Mechanical Engineering
prof. dr. ir. A.S.J. Suiker	Department of the Built Environment
dr. ir. V.G. Kouznetsova	Department of Mechanical Engineering
ir L. Liu	Department of Mechanical Engineering

Abstract

Low-frequent vibrations in lightweight thin structures such as beams or plates can cause large distortions. To prevent such structural distortions, flexural waves must be attenuated as they are known as dominant role in the low-frequency regime. In recent years, locally resonant acoustic metamaterial (LRAM) plate designs have been regarded as a potential solution. This type of material can open up frequency band-gaps in the low-frequency regime through local resonance effects. Within frequency band-gaps, flexural waves can be significantly attenuated do not propagate, effectively protecting thin structures from disastrous structural distortions.

Along with the increasing attention on LRAM plates, fast and accurate validation of novel designs becomes of great importance. LRAM plates are in general complicated and therefore direct numerical simulations (DNS) based on e.g. finite element method (FEM) are often employed for accurate concept validation. Nevertheless, as the dimension and design complexity of LRAM plate design increases, the computational cost of DNS increases rapidly and even become unbearable. These trigger the development of computational homogenization techniques for LRAM plates, such that these can capture the micro-inertia and thereby local resonance effects, and allow for simultaneous analysis of the macroscale and the microscale at low computational cost.

A general dynamic computational homogenization framework applicable to LRAM beams and plates was developed and validated on simple beam structures in [29]. This homogenization framework employs the thin continuum shell description on the macroscale and the full solid continuum at the microscale. By applying the Craig-Bampton mode synthesis under the long wavelength assumption, the internal dynamics at the microscale are described by a minimized set of eigenmodes. What remains is a macroscopic continuum shell description expressed in terms of the macroscopic degrees of freedom enriched by the emergent degrees of freedom that represent the internal dynamics at the microscale. Such a reduced dynamic description eventually leads to low computational cost, together with high accuracy on analysing LRAM plates.

This thesis presents the implementation and validation of the homogenization framework developed in [29] for three dimensional (3D) flat LRAM plates. The LRAM unit-cell is discretized within standard FEM after which the the unit-cell model reduction is performed. First, an infinite LRAM plate is investigated. The homogenization-based dispersion spectra are validated by comparing them to a reference solution obtained from Bloch analysis. Moreover, a finite LRAM plate is investigated. The macroscopic problem is implemented according to isogeometric analysis (IGA) and the finite LRAM plate is discretized using isogeometric elements. Two case-studies are introduced for which the the macroscopic steady-state and transient responses of the finite plate under certain loading conditions are analysed. For the sake of validation, the homogenized response is compared to the response of the full-scale analysis computed by FEM-based DNS. These validations indeed demonstrate the power of

the adopted homogenization framework on largely reducing computational costs while retaining comparable accuracy, in contrast to standard numerical techniques

Finally, the application potential of this homogenization framework is demonstrated through analyzing a finite LRAM plate subjected to a general excitation composed of multiple frequencies. This study is computationally prohibitive using standard numerical techniques. This study shows that the homogenization framework is able to capture the attenuating performance for LRAM plates of large macroscopic dimensions at relatively low computational costs.

Contents

List of Figures

List of Tables

Nomenclature

Symbols

[1]

Scalars		
A	[m^2]	Surface area
h	[m]	Thickness
H	[m]	Macroscopic thickness
l	[-]	Representative length
L	[m]	Microscopic unit-cell length
m	[kg]	Mass
N	[-]	Uni-variate basis function
M	[-]	Uni-variate basis function
r	[m]	Core radius
R	[m]	Coating outer radius or bi-variate basis function
S	[m]	Contour
T	[-]	Tying constraint
U	[m]	Amplitude
w	[m]	Weight factor
W	[m]	Microscopic unit-cell width
δ	[-]	Small variation
ζ	[-]	Eigenmode displacement amplitude
η	[m]	Out-of-plane spatial coordinate
θ	[rad]	Rotation
λ	[m]	Wavelength
μ	[-]	Modal fraction
ξ	[m]	In-plane spatial coordinate
ρ	[kgm^{-3}]	Mass density
τ	[-]	test function of ζ
χ	[-]	Parametric coordinate
ψ	[-]	Parametric coordinate
ω	[$rad \cdot s^{-1}$]	Angular frequency
Vectors		
$\vec{b}$	[m]	Bending displacement
$\vec{c}$	[-]	Bending displacement test function
$\vec{d}$	[m]	Current director
$\vec{D}$	[m]	Reference director

[1] The SI-units for of each symbol denoted here but may vary throughout the thesis.

$\vec{e}$	[m]	Base vector
$\vec{f}$	$[\mathrm{kg} \cdot \mathrm{m}^{-1} \cdot \mathrm{s}^{2}]$	Reaction force
$\vec{j}$	$[\mathrm{kg}^{-\frac{1}{2}}]$	Modal kinematic coupling
$\vec{n}$	[m]	Normal vector
$\vec{p}$	$[\mathrm{kg} \cdot \mathrm{m}^{-2}\mathrm{s}^{-1}]$	Linear momentum
$\vec{P}$	$[\mathrm{kg} \cdot \mathrm{m}^{-1}\mathrm{s}^{-1}]$	Linear momentum resultant
$\vec{Q}$	$[\mathrm{kg} \cdot \mathrm{s}^{-1}]$	Rotational momentum resultant
$\vec{t}$	$[\mathrm{kg} \cdot \mathrm{m}^{-1} \cdot \mathrm{s}^{2}]$	Traction
$\vec{u}$	[m]	Displacement
$\vec{v}$	[-]	Displacement test function
$\vec{w}$	[-]	Micro-fluctuation
$\vec{W}$	$[\mathrm{kg} \cdot \mathrm{m}]$	Coupling relation
$\vec{x}$	[m]	Current position
$\vec{X}$	[m]	Reference position
$\vec{\phi}$	[m]	Modal displacement field
$\vec{\nabla}$	[-]	Spatial gradient
$\vec{X}$	[-]	Knot vector
$\vec{\Psi}$	[-]	Knot vector
Tensors		
$\mathbb{B}$	$[\mathrm{kg} \cdot \mathrm{s}^{2}]$	Stiffness
$\mathbb{F}$	[-]	Deformation gradient
$\mathbf{h}$	$[\mathrm{kg}^{-\frac{1}{2}} \cdot \mathrm{m}^{2}]$	Modal stress coupling
$\mathbb{H}$	[-]	In-plane displacement gradient
$\mathbb{I}$	[-]	Unit tensor
$\mathbb{K}$	[-]	Deformation curvature
$\mathbb{M}$	$[\mathrm{kg} \cdot \mathrm{m}^{-1} \cdot \mathrm{s}^{2}]$	Couple-stress resultant
$\mathbb{N}$	$[\mathrm{kg} \cdot \mathrm{m}^{-2} \cdot \mathrm{s}^{2}]$	Stress resultant
$\mathbb{O}$	[-]	Zero tensor
$\mathbb{S}$	[-]	Static condensate
$\mathbb{W}$	[kg]	Mass
$\boldsymbol{\varepsilon}$	[-]	Strain
$\boldsymbol{\rho}$	$[\mathrm{kg} \cdot \mathrm{m}^{-2}]$	Mass density
$\boldsymbol{\sigma}$	$[\mathrm{kg} \cdot \mathrm{m}^{-3} \cdot \mathrm{s}^{2}]$	Stress
${}^{4}\mathbb{C}$	$[\mathrm{kg} \cdot \mathrm{m}^{-3} \cdot \mathrm{s}^{2}]$	Fourth-order elasticity
${}^{4}\mathbb{D}$	[kg]	Fourth-order elastic inertia density
Domains		
$\mathcal{A}$	$[\mathrm{m}^{\cdot 2}]$	Lamina surface domain
$\mathcal{C}$	[m]	Lamina surface contour
$\mathcal{H}$	[m]	Thickness domain
$\mathcal{S}$	$[\mathrm{m}^{\cdot 2}]$	Surface domain
$\mathcal{V}$	$[\mathrm{m}^{\cdot 3}]$	Volume domain
Others		
$\mathcal{B}$	[-]	Generalized stiffness matrix
$\mathcal{F}$	[-]	Generalized force column
$\mathcal{U}$	[-]	Generalized displacement column or Sobolev function space
$\mathcal{W}$	[-]	Generalized mass matrix

Markers

Subscripts	
0	Initial configuration
amp	Amplitude
d	Dependent quantity
f	Free quantity
het	Heterogeneity
i	Independent quantity
in	Input quantity
m	Microscopic scale
M	Macroscopic scale
mat	Matrix material
n	Mode n quantity
out	Output quantity
p	Prescribed quantity
r	Reference domain
res	Resonance
tr	Transformed quantity
Superscripts	
amb	Ambient
A	Lamina-level
b	Bending deformation
bo	Body wave
B	Back boundary
c	Co-rotational lamina-level coordinate basis
D	Bottom boundary
dy	Dynamic response
fl	Flexural wave
F	Front boundary
h	Approximation
lm	Linear motion
loc	Local
L	Left boundary
LB	Edge between left and back boundary
LF	Edge between left and front boundary
m	Membrane deformation
qs	Quasi-static
rt	Rotation
R	Right boundary
RB	Edge between right and back boundary
RF	Edge between right and front boundary
ss	Steady-state quantity
T	Top boundary
+	Tied boundary
−	Tied boundary

$*$	Reduced quantity
Operators	
$\hat{\bullet}$	In-plane component
$\tilde{\bullet}$	Out-of-plane product
$\dot{\bullet}$	Order 1 time derivative
$\ddot{\bullet}$	Order 2 time derivative
$\bullet^{\mathrm{C}}$	Conjugate
$\bullet^{\mathrm{CT}}$	Conjugate transpose
$\bullet^{\mathrm{T}}$	Transpose
$\underset{\sim}{\bullet}$	Column notation
$\underline{\bullet}$	Matrix notation
$\bullet\bullet$	Dyadic product
$\bullet \cdot \bullet$	Dot product
$\bullet : \bullet$	Double dot product
Abbreviations	
1D	One dimensional
2D	Two dimensional
3D	Three dimensional
BVP	Boundary Value Problem
CBMS	Craig-Bampton Mode Synthesis
DNS	Direct Numerical Simulation
DOF	Degree of freedom
FEM	Finite Element Method
LRAM	Locally Resonant Acoustic Metamaterial

Chapter 1

Introduction

1.1 Locally resonant acoustic metamaterials

The design of lightweight materials is a trending field of research within numerous industries. Not only due to the economic benefits of lighter and stronger materials, but also to their environmental benefits. In the transport sector for example, lightweight composite materials are already used, such as honeycomb sandwich panels in the aviation industry or composite plates for shipping containers [1, 2]. Nevertheless, an undesirable property of most lightweight materials is their poor vibrational performance in the low-frequency regime, caused by the high specific stiffness. Conventional designs of lightweight materials usually present a trade-off between weight reduction and vibration attenuation. An innovative solution is needed to overcome such a trade-off and enable the design of a lightweight material with the ability to attenuate structural vibrations.

Many lightweight structures are composed of a variety of thin structures (plates/-beams) in which multiple wave types can occur in nature, e.g. body waves or flexural waves [3, 4]. In Fig. 1.1 the deformation due to body (compression and shear) and flexural waves is illustrated. Note that the deformation is magnified. In the low-frequency regime, flexural waves are dominant over body waves due to their relatively short wavelength in that frequency range [5]. Hence, the existence of low-frequent flexural waves in thin structures can cause large structural deformations. Due to their dominance, the need for attenuating flexural waves in the low-frequency regime is of great importance. As illustrated in Fig. 1.1c, the flexural wave is composed of an out-of-plane linear motion and an out-of-plane rotation. Hence, attenuating flexural waves in thin structures can be achieved by cancelling either the out-of-plane linear or rotational motion.

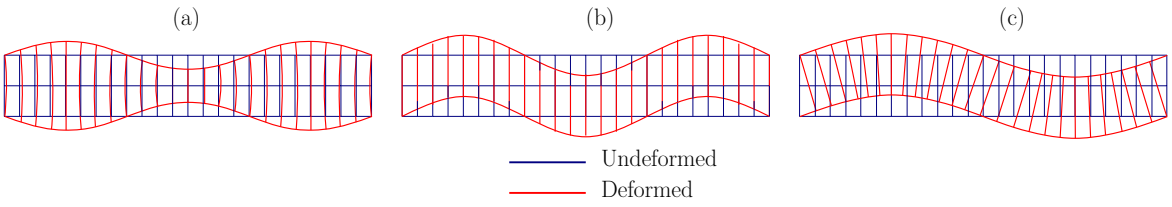

Figure 1.1: *An undeformed beam (blue) and the magnified deformation (red) due to compression (a), shear (b) and flexural (c) waves.*

A novel material that is able to cancel these distortions are locally resonant acoustic metamaterials (LRAMs). This new type of material owes its favourable acoustic/vibrational properties to the interaction between inclusions of sub-wavelength dimensions and a stiff and

relatively lightweight host matrix. LRAM plates are able to open up frequency band-gaps, i.e., frequency zones in which free wave propagation is not possible as a result of the interaction between inclusion and host. Inside these frequency band-gaps, the linear or rotational motion caused by body or flexural waves is cancelled. This can be attributed to the negative effective mass and negative effective bending stiffness of the LRAM, respectively [6–12]. The meaning of these negative effective properties will be explained briefly.

The dispersion spectrum and a simple unit-cell configuration employing the negative effective mass effect are illustrated in Fig. 1.2(a). The frequency band-gap is denoted by the red-marked area. This dispersion spectrum shows the frequency response of an infinite medium to a certain wavetype as function of the wavenumber. Consider a plate of mass m_1 and a resonator of mass m_2 connected through a linear spring. When the plate is subjected to a flexural wave, the linear out-of-plane motion of the plate ($\vec{u}_1$) will intuitively activate an out-of-plane motion of the resonator ($\vec{u}_2$). Once the frequency of the flexural wave reaches the resonance frequency of mass m_2, the effective mass density of the LRAM unit-cell becomes negative and the resonator and the plate move in opposite phase, actively attenuating the out-of-plane linear motion. The resonance frequency is indicated by the lower limit of the frequency band-gap. As the frequency of the wave increases, the effective mass of the unit-cell will become positive again and the flexural wave can propagate again. This frequency is marked by the upper limit of the frequency band-gap.

The dispersion spectrum and the unit-cell configuration employing the negative effective bending stiffness are illustrated in Fig. 1.2(b). The frequency band-gap is denoted by the red-marked area. Consider again a plate of mass m_1 and to this plate a flat cylindrical resonator of mass m_2 is attached by two in-plane aligned collinear springs. The flexural wave imposes a bending moment (M) on the unit-cell resulting in out-of-plane bending. Accordingly, the top surface of the unit-cell will alternately compress and elongate, activating in-plane rotation θ of the resonator. For frequencies below the rotational resonance frequency, the bending motion of the plate and the rotation of mass m_2 occur in opposite phase and the effective bending stiffness becomes negative. This frequency is indicated by the upper limit of the band-gap. As the frequency decreases, the effective bending stiffness becomes positive again and the frequency band-gap is closed. This frequency is indicated by the lower limit of the band-gap in Fig. 1.2(b).

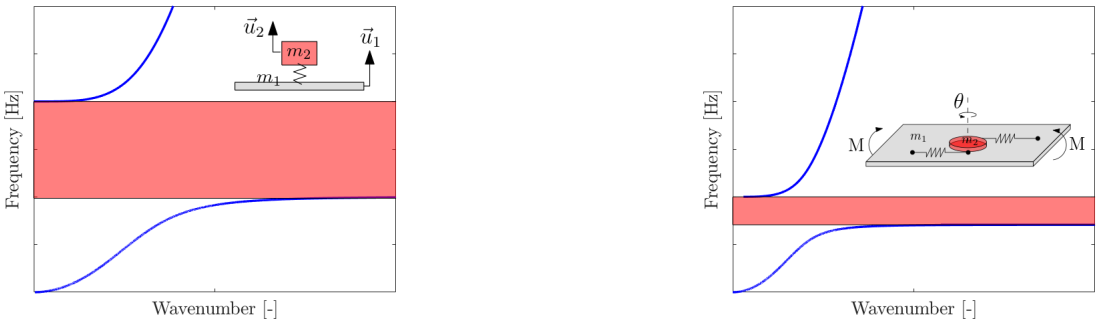

(a) (b)

Figure 1.2: *Dispersion spectra showing negative effective mass (a) and negative effective bending stiffness induced bang-gaps (b) together with the corresponding unit-cell configurations.*

A difference is observed between the frequency range of both band-gaps in Fig. 1.2. The range of the negative mass-induced band-gap is mainly defined by the ratio of the

resonator mass and the mass of the plate. Regarding the range of the negative effective bending stiffness-induced band-gap, it is both defined by the resonance frequency and the ratio of the resonator bending stiffness and the bending stiffness of the plate [9]. Hence, in the low-frequency regime a negative mass-induced band-gap is more likely to open up compared to the negative stiffness-induced band-gap if the resonator mass is the same for both cases. Therefore, the negative effective mass effects of LRAMs are more attractive in the investigation of low-frequency vibration attenuation in thin structures.

1.2 Analysing LRAM plates

To show the concept of the negative effective properties of LRAMs and the existence of frequency band-gaps, analytical models have been derived and validated [13–15]. Also for the analysis of simple LRAM designs analytical models have been developed. These analytic models however, are not generally applicable to any LRAM design. Since the potential of LRAMs is not restricted to simple unit-cell designs or straightforward macroscopic structures, one should be able to analyse more complex geometries, e.g. curved panels or cylindrical rods [16, 17]. In many cases it is possible to analyse the attenuation performance of LRAMs by means of experiments. Yet, this often is a time consuming and expensive solution, requiring state-of-the-art production and testing facilities. Especially when designing new LRAM applications, validating these designs by means of experiments can be extremely cumbersome. Therefore, numerical methods are used nowadays to analyse LRAM designs.

Using numerical methods for the analysis of LRAMs yields more freedom with respect to designing the unit-cell or the macroscopic structure and the application of boundary conditions. In various numerical studies, the finite element method (FEM) has been employed to analyse LRAMs. In several studies, the outcome of numerical analysis techniques were compared to experimental results and an excellent agreement exists between the two methods [18–21]. To properly analyse LRAMs it is important that the microstructure is modelled accurately to capture the local resonance effects, responsible for wave attenuation. This implies that the number of degrees of freedom (DOFs) increases rapidly if the macrostructure is composed of multiple unit-cells. Take for example the unit-cell design in Fig. 1.3. Discretising this unit-cell would already lead to a large number of degrees of freedom. Imagine the computational costs if one wanted to analyse an LRAM plate composed of these unit-cells. High computational costs and a high demand on data storage are often the reason that in many numerical studies, structures of only a few unit-cells can be analysed [22–25]. This means that for LRAM structures of large macroscopic dimensions with even simple unit-cell designs, new numerical methods are necessary to enable its numerical analysis.

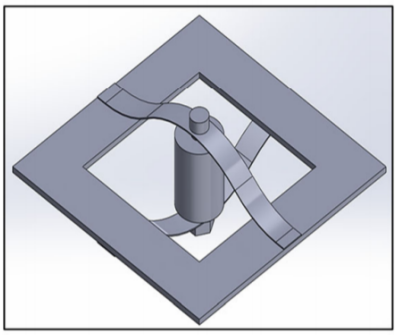

Figure 1.3: *Unit-cell design of a thin homogeneous plate with an embedded resonator [21].*

1.3 Computational homogenization for LRAM plates

A promising numerical technique for the analysis of LRAM plates is computational homogenization. This numerical technique can describe the constitutive response of a material at the macroscale based on a detailed model of the heterogeneous material at the microscale. The macroscopic loading conditions are used to define boundary conditions applicable to the microscopic unit-cell, resulting in a microscopic boundary value problem. Solving this boundary value problem and applying an up-scaling transition, leads to the macroscopic effective quantities of the material. With these quantities, the response at the macroscale can be obtained.

Many homogenization frameworks have been developed to analyse LRAMs but a general framework able to capture both body and flexural waves under the subwavelength range did not exist [26–28]. To this extent, a new multi-scale homogenization framework was developed in [29]. The developed method is based on a homogenization method for heterogeneous thin sheets [30] and the homogenization scheme in [31], in which an enriched macroscopic shell continuum description was developed. The homogenization scheme in [30] is used to describe a macroscopic heterogeneous thin sheet by means of a homogenized thin continuum shell description. A through-thickness full continuum solid unit-cell at the microscale is used to determine the constitutive response of the macroscopic shell. The deformation of the macroscopic shell is expressed in terms of the membrane deformation and bending of a reference surface. Through a down-scaling relation, the macroscopic deformation can be imposed on the unit-cell in terms of periodic boundary conditions. Upscaling the unit-cell response yields the macroscopic resultant quantities in terms of the membrane deformation and the homogenized effective tangents. A through-thickness integration at the macroscale is not needed because of the employed unit-cell configuration.

Solving the microscopic boundary valie problem can be time consuming, especially for a time-dependent problem with many degrees of freedom. To avoid this issue, the micrscopic description is reduced by applying the Craig-Bampton mode synthesis [31]. This approach enables the description of the full continuum microscopic response by superposing the quasi-static unit-cell response to prescribed boundary nodes and the dynamic unit-cell response resulting in a reduced microscopic dynamic model. Combining the frameworks from [30] and [31], results in a homogenized thin continuum shell description enriched by the contribution of local resonance effects developed in [29].

1.4 Towards a 3D implementation

The newly developed homogenization method in [29] enables the user to implement any material model as well as any microscopic and macroscopic design accompanied by appropriate boundary conditions. Moreover, it enables one to capture both body and flexural waves in the low-frequency regime and it simultaneously yields an accurate description of the internal dynamics. The developed homogenization framework has been validated on flat LRAM beams in [29]. Yet, the potential of locally resonant acoustic metamaterials is not restricted to beam structures. Hence, to give a more general validation of the developed framework, its implementation is extended from 2D LRAM beams towards 3D flat LRAM plates in this thesis. Furthermore, a case study on the potential applications of the homogenization framework is performed.

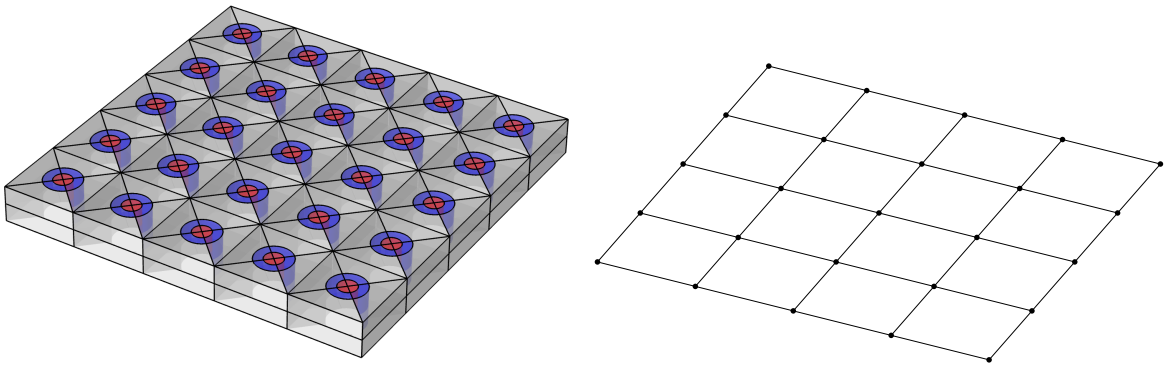

(a) (b)

Figure 1.4: *Full-scale representation of an LRAM plate composed of 25 unit-cells (a) and the corresponding enriched thin continuum shell representation (b).*

In conclusion, the main objective of this master thesis is to extend the implementation of the developed homogenization framework for LRAM beams in [29] such that it can be used to analyse flat LRAM plates in a computationally cheap manner.
The outline of this thesis is planned as follows:

- In Chapter 2 the dynamic computational homogenization framework is introduced after which in Chapter 3 the enriched thin continuum shell description is introduced. These two chapters form a summary of the derivation of the homogenization framework developed in [29]. The result is the enriched macroscopic continuum shell description applicable to LRAMs.

- In Chapter 4, the 3-dimensional implementation of the framework is validated by analysing an infinite flat LRAM plate. This will be done by comparing the dispersion spectra computed by the homogenization method to a reference solution. The reference solution for the infinite LRAM plate is obtained by the Bloch analysis.

- In Chapter 5, isogeometric analysis is used to analyse a finite LRAM plate. To this extent, the framework to discretize the finite plate using isogeometric finite elements is implemented first. Subsequently, the macroscopic response of the LRAM plate under certain loading conditions is compared to the reference solution obtained from FEM-based Direct Numerical Simulation (DNS). This concludes the implementation and validation of the homogenization framework from two to three dimensional space.

- In Chapter 6 the homogenization framework is used to analyse a finite LRAM plate subjected to more general excitations. Here, a Gaussian input signal is subjected to an LRAM plate and the attenuating performance of the plate is analysed using the homogenization framework. This study shows the potential of the framework.

- In Chapter 7, some conclusions and recommendations are given.

Chapter 2

Dynamic computational homogenization framework

In this chapter the dynamic computational homogenization framework developed in [29] is explained. The computational homogenization framework applicable to heterogeneous thin sheets in [30] is extended towards a dynamic computational homogenization framework by taking into account the micro and macroscopic inertia. To this extent, the continuum shell description to be employed at the macroscale and the full continuum description to be employed at the microscale are introduced. Accordingly, a relaxed separation of scales will define the range of applicability of the homogenization scheme. Only the most important derivations are shown in this thesis and for a more detailed description, the reader is referred to [29].

2.1 Macroscale - Continuum shell description

2.1.1 Kinematic description

In Fig. 2.1 the macroscopic configuration of the continuum shell is shown with shell thickness H. In the remainder of this thesis, the subscript $(\bullet)_{\mathrm{M}}$ denotes a variable with respect to the macroscale. For the continuum shell description, a reference plane is defined as the plane located in the middle between the top and bottom surface. All points located at equal out-of-plane distance from the reference plane form a surface referred to as a lamina. All points on a line perpendicular to the reference plane in the initial configuration form a fibre. The reference plane is indicated by the dash-dotted surface in Fig. 2.1 and the fibre is indicated by the dark blue lines. A material point in the initial configuration $\vec{X}_{\mathrm{M}}$ is described by a point on the initial reference plane $\vec{X}_{\mathrm{M,r}}$ and its point along the initial director $\vec{D}$. Correspondingly, a material point in the current configuration $\vec{x}_{\mathrm{M}}$ is described by a point on the current reference plane $\vec{x}_{\mathrm{M,r}}$ and a point on the current director $\vec{d}$. Subtracting the current position from the reference position yields the displacement field of a point in the continuum shell as

$$\vec{u}_{\mathrm{M}} = \vec{u}_{\mathrm{M,r}} + \eta\vec{b}_{\mathrm{M}} \tag{2.1}$$

with $\vec{u}_{\mathrm{M,r}}$ the displacement of the a point due to linear motion of the reference plane (related to body and flexural waves) and $\eta\vec{b}_{\mathrm{M}}$ the bending deformation due to rotation of the fibre (related to the flexural wave). η defines the out-of-plane coordinate along a fibre within the shell thickness domain $\mathcal{H} \in [-H/2, H/2]$.

The framework is only valid for continuum shells with a thickness much smaller than the out-of-plane radius of curvature, enabling one to employ the Kirchhoff-Love theory [32].

This theory makes use of the assumption that fibres remain straight, are inextensible and remain perpendicular to the reference plane during deformation.

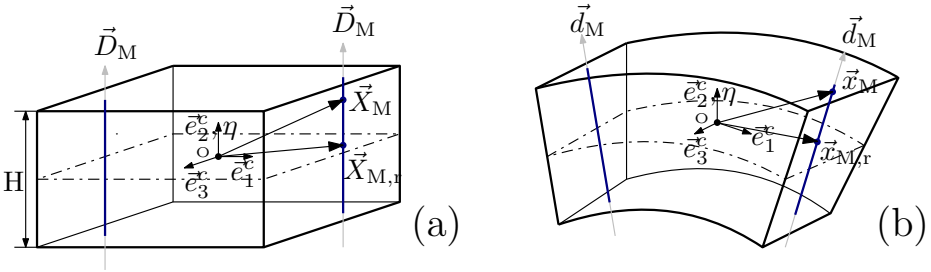

Figure 2.1: *Macroscopic continuum shell description in initial (a) and current (b) configuration.*

In Fig. 2.1 the corotational basis $\{\vec{e}_1^{\,\mathrm{c}}, \vec{e}_2^{\,\mathrm{c}}, \vec{e}_3^{\,\mathrm{c}}\}$ is introduced. This corotational basis rotates rigidly with the shell deformation and can therefore be seen as a local Cartesian basis. The plane spanned by $\{\vec{e}_1^{\,\mathrm{c}}, \vec{e}_3^{\,\mathrm{c}}\}$ is tangent to the reference plane and the vector $\vec{e}_2^{\,\mathrm{c}}$ is orthogonal to the reference plane. In the remainder of this thesis, variables are often decomposed into an in-plane and out-of-plane component. For an arbitrary vector $\vec{a}$, the in-plane and out-of-plane component are denoted as $\tilde{\vec{a}} = \vec{a} \cdot \vec{e}_2^{\,\mathrm{c}} \vec{e}_2^{\,\mathrm{c}}$ and $\hat{\vec{a}} = \vec{a} \cdot [\mathbb{I} - \vec{e}_2^{\,\mathrm{c}} \vec{e}_2^{\,\mathrm{c}}]$, respectively, and $\mathbb{I}$ is a second-order unit tensor. Furthermore, an arbitrary tensor $\mathbb{A}$ composed of two decomposed in-plane or out-of-plane vectors or a combination of the two and is defined as $\hat{\tilde{\mathbb{A}}} = \hat{\tilde{a}}\hat{\tilde{a}}$ and $\tilde{\hat{\mathbb{A}}} = \tilde{\hat{a}}\hat{\tilde{a}}$.

The infinitesimal material line in the current configuration $\mathrm{d}\vec{x}_{\mathrm{M}}$ is defined by transforming the infinitesimal material line in the initial configuration $\mathrm{d}\vec{X}_{\mathrm{M}}$ via the macroscopic deformation tensors. Under the corotational decomposition, this can be written as

$$\mathrm{d}\hat{\tilde{\vec{x}}}_{\mathrm{M}} = \left[\hat{\tilde{\mathbb{F}}}_{\mathrm{M}} + \eta \hat{\tilde{\mathbb{K}}}_{\mathrm{M}}\right] \cdot \mathrm{d}\hat{\tilde{\vec{X}}}_{\mathrm{M}} \tag{2.2a}$$

$$\mathrm{d}\tilde{\hat{\vec{x}}}_{\mathrm{M}} = -\frac{1}{2} \vec{e}_2^{\,\mathrm{c}} \tilde{\hat{\mathbb{K}}}_{\mathrm{M}} : \mathrm{d}\hat{\tilde{\vec{X}}}_{\mathrm{M}} \mathrm{d}\hat{\tilde{\vec{X}}}_{\mathrm{M}} \tag{2.2b}$$

with $\hat{\tilde{\mathbb{F}}}_{\mathrm{M}} = [\hat{\tilde{\nabla}}_{\mathrm{M},0} \hat{\tilde{x}}_{\mathrm{M,r}}]^{\mathrm{T}}$ the in-plane deformation gradient tensor and $\hat{\tilde{\mathbb{K}}}_{\mathrm{M}} = [\hat{\tilde{\nabla}}_{\mathrm{M},0} \hat{\tilde{d}}_{\mathrm{M}}]^{\mathrm{T}}$ the in-plane deformation curvature tensor under the small deformation assumption. The superscript $(\bullet)^{\mathrm{T}}$ denotes the transpose. In eq. (2.2) the transverse shear deformation gradient is neglected according to the Kirchhoff-Love theory, i.e., each fibre must remain normal to the reference lamina during deformation. Also the in-plane gradient of the out-of-plane position component $\tilde{\hat{\mathbb{F}}}_{\mathrm{M}} = \mathbb{O}$ since the corotational basis is employed.

2.1.2 Strong form problem

The linear balance of momentum for the continuum shell in absence of body forces is decomposed under the corotational basis. After subsequent integration along η and assuming stress-free top and bottom surfaces, the balance equations of linear and rotational momentum resultants are defined as

$$\hat{\tilde{\nabla}}_{\mathrm{M}} \cdot \left[\hat{\tilde{\mathbb{N}}}_{\mathrm{M}}(\vec{x}_{\mathrm{M,r}}) + \hat{\tilde{\mathbb{N}}}_{\mathrm{M}}(\vec{x}_{\mathrm{M,r}})\right] - \dot{\vec{P}}_{\mathrm{M}}(\vec{x}_{\mathrm{M,r}}) = \vec{0}, \ \forall \vec{x}_{\mathrm{M,r}} \in \mathcal{A}_{\mathrm{M,r}} \tag{2.3a}$$

$$\hat{\tilde{\nabla}}_{\mathrm{M}} \cdot \left[\hat{\tilde{\mathbb{M}}}_{\mathrm{M}}(\vec{x}_{\mathrm{M,r}}) + \hat{\tilde{\mathbb{M}}}_{\mathrm{M}}(\vec{x}_{\mathrm{M,r}})\right] - \tilde{\hat{e}}^{\mathrm{c}} \cdot \tilde{\hat{\mathbb{N}}}_{\mathrm{M}}(\vec{x}_{\mathrm{M,r}}) - \dot{\vec{Q}}_{\mathrm{M}}(\vec{x}_{\mathrm{M,r}}) = \vec{0}, \ \forall \vec{x}_{\mathrm{M,r}} \in \mathcal{A}_{\mathrm{M,r}} \tag{2.3b}$$

where $\hat{\tilde{\nabla}}_{\mathrm{M}} = \partial(\bullet)/\partial \vec{x}_{\mathrm{M,r}}$. The macroscopic stress resultant is denoted as $\mathbb{N}_{\mathrm{M}}$, $\dot{\vec{P}}_{\mathrm{M}}$ denotes the linear inertia resultant, $\mathbb{M}_{\mathrm{M}}$ the couple-stress resultant, $\dot{\vec{Q}}_{\mathrm{M}}$ the rotational inertia resultant

and $\mathcal{A}_{\mathrm{M,r}}$ the domain spanned by the reference plane. The resultant quantities are defined as

$$\mathbb{N}_{\mathrm{M}} = \int_{\mathcal{H}} \boldsymbol{\sigma}_{\mathrm{M}} \mathrm{d}\eta \tag{2.4a}$$

$$\mathbb{M}_{\mathrm{M}} = \int_{\mathcal{H}} \eta \boldsymbol{\sigma}_{\mathrm{M}} \mathrm{d}\eta \tag{2.4b}$$

$$\dot{\vec{P}}_{\mathrm{M}} = \int_{\mathcal{H}} \dot{\vec{p}}_{\mathrm{M}} \mathrm{d}\eta \tag{2.4c}$$

$$\dot{\vec{Q}}_{\mathrm{M}} = \int_{\mathcal{H}} \eta \dot{\vec{p}}_{\mathrm{M}} \mathrm{d}\eta \tag{2.4d}$$

with $\boldsymbol{\sigma}_{\mathrm{M}}$ the Cauchy stress tensor and $\dot{\vec{p}}_{\mathrm{M}} = \rho_{\mathrm{M}} \ddot{\vec{u}}_{\mathrm{M}}$. $\vec{p}_{\mathrm{M}}$ is the linear momentum and ρ the mass density. A plane-stress state is considered when employing the Kirchoff-Love theory, implying no out-of-plane shear deformation. Yet, this is in contradiction with the balance equations where the out-of-plane inertia is also taken into account. To this extent, the assumption of zero out-of-plane shear deformation is only employed in the kinematic relations but relaxed in the balance equations.

The balance equations in eq. (2.3) must be solved for the unknowns $\vec{u}_{\mathrm{M,r}}$ and $\vec{b}_{\mathrm{M}}$. Together with the appropriate boundary conditions, the balance equations form the strong form problem of the macroscopic continuum shell description, written as

$$\text{find } (\vec{u}_{\mathrm{M,r}}, \vec{b}_{\mathrm{M}}) \in (\mathcal{U}^1, \mathcal{U}^1), \text{ such that:} \tag{2.5a}$$

$$\hat{\vec{\nabla}}_{\mathrm{M}} \cdot \left[\hat{\mathbb{N}}_{\mathrm{M}} + \hat{\mathbb{N}}_{\mathrm{M}} \right] - \dot{\vec{P}}_{\mathrm{M}} = \vec{0} \tag{2.5b}$$

$$\hat{\vec{\nabla}}_{\mathrm{M}} \cdot \left[\hat{\mathbb{M}}_{\mathrm{M}} + \hat{\mathbb{M}}_{\mathrm{M}} \right] - \tilde{\vec{e}}^{\mathrm{c}} \cdot \tilde{\mathbb{N}}_{\mathrm{M}} - \dot{\vec{Q}}_{\mathrm{M}} = \vec{0}, \ \forall \vec{x}_{\mathrm{M,r}} \in \mathcal{A}_{\mathrm{M,r}} \tag{2.5c}$$

$$\vec{u}_{\mathrm{M,r}} = \vec{u}^{\mathrm{p}}_{\mathrm{M,r}} \text{ on } \mathcal{C}_{\mathrm{M,r},u} \qquad \vec{b}_{\mathrm{M}} = \vec{b}^{\mathrm{p}}_{\mathrm{M}} \text{ on } \mathcal{C}_{\mathrm{M,r},b} \tag{2.5d}$$

$$\vec{t}_{\mathrm{M}} = \vec{t}^{\mathrm{p}}_{\mathrm{M}} \text{ on } \mathcal{C}_{\mathrm{M,r},t} \qquad \vec{m}_{\mathrm{M}} = \vec{m}^{\mathrm{p}}_{\mathrm{M}} \text{ on } \mathcal{C}_{\mathrm{M,r},m} \tag{2.5e}$$

where $\vec{t}_{\mathrm{M}}$ and $\vec{m}_{\mathrm{M}}$ are the traction and couple-traction resultant, $\mathcal{U}^1$ is the first Sobolev function space and $\mathcal{C}_{\mathrm{M,r}}$ denotes the contour of the reference plane. The superscript $(\bullet)^{\mathrm{p}}$ indicates a prescribed quantity on the corresponding range of the contour $\mathcal{C}_{\mathrm{M,r}}$.

2.1.3 Weak form problem

By employing the weak form, the pointwise satisfaction of eq. (2.5) is relaxed. To arrive at the weak form problem, the weighted residuals approach is applied by multiplying eq. (2.5(b)) with $\vec{v}_{\mathrm{M,r}}$, the test function of $\vec{u}_{\mathrm{M,r}}$. Consequently, eq. (2.5(c)) is multiplied by $\vec{c}_{\mathrm{M}}$, the test-function of $\vec{b}_{\mathrm{M}}$. Subsequent application of the chain-rule and Gauss's theorem, results in the weak form problem defined in terms of the internal, external and kinematic weighted residuals. The out-of-plane stress and stress-couple resultants, $\hat{\mathbb{N}}$, $\tilde{\mathbb{N}}$ and $\hat{\mathbb{M}}$ are negligible compared to the in-plane stress and couple resultants, $\hat{\mathbb{N}}$ and $\hat{\mathbb{M}}$ for the thin continuum shell description. Finally, the weak form problem is written as

$$\text{find } (\vec{u}_{\mathrm{M,r}}, \vec{b}_{\mathrm{M}}) \in (\mathcal{U}^1, \mathcal{U}^1), \text{ such that:} \tag{2.6a}$$

$$W_{\mathrm{int}} + W_{\mathrm{kin}} = W_{\mathrm{ext}}, \ \forall (\vec{v}_{\mathrm{M,r}}, \vec{c}_{\mathrm{M}}) \in (\mathcal{U}^1, \mathcal{U}^1) \tag{2.6b}$$

with the internal, kinematic and external weighted residuals formulated as

$$W_{\text{int}} = \int_{\mathcal{A}_{\text{M,r}}} \left[\hat{\tilde{\nabla}}_{\text{M}} \vec{v}_{\text{M,r}}\right]^{\text{T}} : \hat{\mathbb{N}}_{\text{M}} \text{d}A_{\text{M}} + \int_{\mathcal{A}_{\text{M,r}}} \left[\hat{\tilde{\nabla}}_{\text{M}} \vec{c}_{\text{M}}\right]^{\text{T}} : \hat{\mathbb{M}}_{\text{M}} \text{d}A_{\text{M}} \tag{2.7a}$$

$$W_{\text{kin}} = \int_{\mathcal{A}_{\text{M,r}}} \vec{v}_{\text{M,r}} \cdot \dot{\vec{P}}_{\text{M}} \text{d}A_{\text{M}} + \int_{\mathcal{A}_{\text{M,r}}} \vec{c}_{\text{M}} \cdot \dot{\vec{Q}}_{\text{M}} \text{d}A_{\text{M}} \tag{2.7b}$$

$$W_{\text{ext}} = \int_{\mathcal{C}_{\text{M,r},t}} \vec{v}_{\text{M,r}} \cdot \vec{t}_{\text{M}} \text{d}C_{\text{M}} + \int_{\mathcal{C}_{\text{M,r},m}} \vec{c}_{\text{M}} \cdot \vec{m}_{\text{M}} \text{d}C_{\text{M}} \tag{2.7c}$$

The out-of-plane stress and couple-stress resultants are removed from the internal weighted residual since they are dominated by their in-plane counterparts in the thin continuum shell description. In the formulation of the weighted residuals, it can be seen that the the boundary conditions defined in eq. (2.5(d-e)) have already been implemented. Furthermore, the test-functions must vanish at the Dirichlet boundaries since $\vec{u}_{\text{M,r}}$ and $\vec{b}_{\text{M}}$ are already defined there. The weak form problem must be complemented by the inertial and constitutive relations, which couple the resultant quantities to the deformation field. These relations are derived during the up-scaling transition of the dynamic homogenization framework and will be described in Section 2.4.2.

2.2 Microscale - Full continuum description

2.2.1 Kinematic description

To each macroscopic fibre a microscopic unit-cell is appointed as illustrated in Fig. 2.2. In this unit-cell representation, all heterogeneities are omitted. In the remainder of this thesis, variables related to the microstructure are denoted by the subscript $(\bullet)_{\text{m}}$. Notice that the macroscopic shell thickness is equal to the microscopic unit-cell height. This means that the effective properties of the unit-cell are through-thickness homogenized quantities. The macroscopic corotational basis intersects with the microscopic Cartesian basis as it rotates rigidly with the deformation, provided that the out-of-plane radius of curvature of the unit-cell is much larger than its in-plane dimensions.

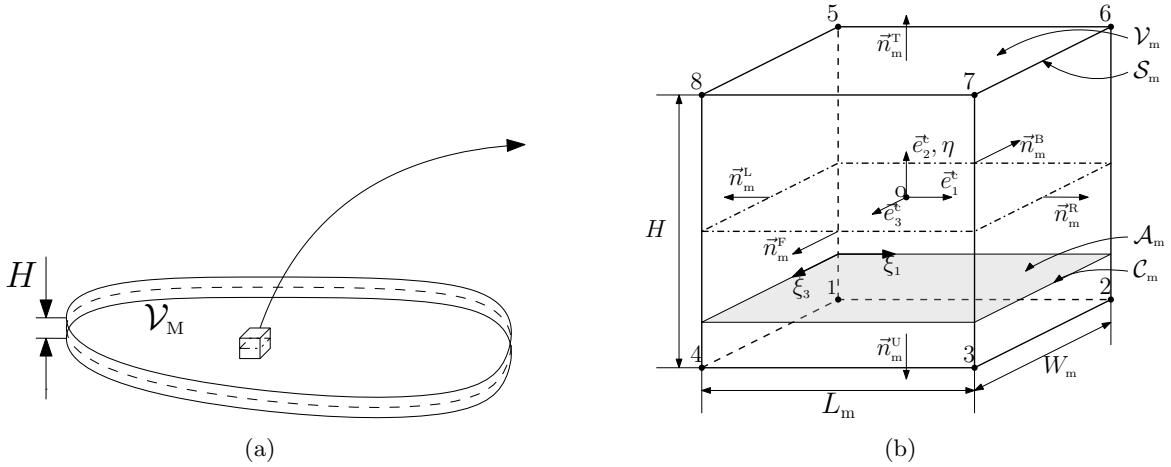

Figure 2.2: *The macroscopic thin continuum shell (a) and the microscopic full 3D unit-cell (b) corresponding to a macroscopic fibre.*

The full continuum solid description is employed here, which means that the current

configuration of an infinitesimal material line $\mathrm{d}\vec{x}_\mathrm{m}$ is related to the material line in the initial configuration $\mathrm{d}\vec{X}_\mathrm{m}$ as

$$\mathrm{d}\vec{x}_\mathrm{m} = \mathbb{F}_\mathrm{m} \cdot \mathrm{d}\vec{X}_\mathrm{m} \tag{2.8}$$

with $\mathbb{F}_\mathrm{m} = [\vec{\nabla}_{\mathrm{m},0}\vec{x}_\mathrm{m}]^\mathrm{T}$ the microscopic deformation gradient tensor under the small deformation assumption. The microscopic displacement field $\vec{u}_\mathrm{m}$ and linear strain $\boldsymbol{\varepsilon}_\mathrm{m}$ are related to one another following the small deformation assumption as well, reading

$$\boldsymbol{\varepsilon}_\mathrm{m} = \frac{1}{2}\left[(\vec{\nabla}_\mathrm{m}\vec{u}_\mathrm{m}) + (\vec{\nabla}_\mathrm{m}\vec{u}_\mathrm{m})^\mathrm{T}\right] - \mathbb{I}_\mathrm{m} \tag{2.9}$$

2.2.2 Strong form problem

Essential for the homogenization of LRAMs is capturing the local resonance effects at the microscale. Therefore, the microscopic balance of momentum is written as

$$\vec{\nabla}_\mathrm{m} \cdot \boldsymbol{\sigma}_\mathrm{m}(\vec{x}_\mathrm{m}) - \dot{\vec{p}}_\mathrm{m}(\vec{x}_\mathrm{m}) = \vec{0},\ \forall \vec{x}_\mathrm{m} \in \mathcal{V}_\mathrm{m} \tag{2.10}$$

where the microscopic inertia of the heterogeneities is captured in $\dot{\vec{p}}_\mathrm{m}(\vec{x}_\mathrm{m}) = \rho_\mathrm{m}(\vec{x}_\mathrm{m})\ddot{\vec{u}}_\mathrm{m}(\vec{x}_\mathrm{m})$ with ρ_m the mass density. This balance of momentum is complemented by a general material law described in eq. (2.11). This material law enables the description of non-linear and time-dependent material .

$$\boldsymbol{\sigma}_\mathrm{m}(\vec{x}_\mathrm{m}, t) = \mathcal{F}_\mathrm{m}\left[\mathbb{F}_\mathrm{m}(\vec{x}_\mathrm{m}, t)\right] \tag{2.11}$$

where t is a point in time. It is assumed that a perfect bonding condition exists between constituents, hence, no void nucleation during deformation. The material law to be used in the validation of the LRAM plate will be discussed later on. The strong form problem of the microscopic description must be complemented with appropriate boundary conditions which follow from the down-scaling transition in Sec. 2.4.1.

2.2.3 Weak form problem

To arrive at the microscopic weak form problem, eq. (2.10) is multiplied by $\vec{v}_\mathrm{m}$, the test-function of the displacement vector $\vec{u}_\mathrm{m}$. Making use of the chain rule and applying Gauss's theorem one may arrive at the weak form problem of the microscopic description, defined as

$$\int_{\mathcal{V}_\mathrm{m}} \left[\vec{\nabla}_\mathrm{m}\vec{v}_\mathrm{m}\right]^\mathrm{T} : \boldsymbol{\sigma}_\mathrm{m}\mathrm{d}V_\mathrm{m} + \int_{\mathcal{V}_\mathrm{m}} \vec{v}_\mathrm{m} \cdot \dot{\vec{p}}_\mathrm{m}\mathrm{d}V_\mathrm{m} = \int_{\mathcal{S}_{\mathrm{m},t}} \vec{v}_\mathrm{m} \cdot \vec{t}_\mathrm{m}\mathrm{d}S_\mathrm{m},\ \forall \vec{v}_\mathrm{m} \in \mathcal{U}^1 \tag{2.12}$$

with $\mathcal{S}_\mathrm{m}$ the surface enclosing the unit-cell volume $\mathcal{V}_\mathrm{m}$ and $\vec{t}_\mathrm{m}$ the traction on the boundaries. Again, the test-function $\vec{v}_\mathrm{m}$ should vanish at the Dirichlet boundaries. To solve the microscopic weak form problem, the appropriate boundary conditions are defined by the downscaling transition, which will be discussed in the next section.

2.3 Lamina-level separation of scales

The key principle in homogenization is the of separation of scales. In [26] a relaxed separation of scales is introduced applicable to LRAMs which was also implemented in [30, 31]. The relaxed separation of scales applies a long-wavelength assumption on the matrix, enforcing

it to be sufficiently stiff at the microscale. This restriction is relaxed with respect to the heterogeneities. This means that the structural waves can interfere with the heterogeneities. For the current framework, the scale separation must be extended with respect to the flexural wavelength. Therefore an extended separation of scales was proposed in [29], written as

$$\text{Matrix:} \qquad l^{\mathrm{A}}_{\mathrm{mat}} \ll \min\{\lambda^{\mathrm{bo}}_{\mathrm{mat}}, \lambda^{\mathrm{fl}}_{\mathrm{mat}}\},\ h_{\mathrm{mat}} \ll \min \lambda^{\mathrm{fl}}_{\mathrm{M}} \tag{2.13a}$$

$$\text{Heterogeneities:} \qquad l^{\mathrm{A}}_{\mathrm{het}} \leq \min\{\lambda^{\mathrm{bo}}_{\mathrm{het}}, \lambda^{\mathrm{fl}}_{\mathrm{het}}\},\ h_{\mathrm{het}} \ll \min \lambda^{\mathrm{fl}}_{\mathrm{M}} \tag{2.13b}$$

where l and h correspond to the representative in-plane and out-of-plane microscopic length-scales, respectively, λ the characteristic wavelength in either the matrix $(\bullet)_{\mathrm{mat}}$ or the heterogeneities $(\bullet)_{\mathrm{het}}$. The superscript $(\bullet)^{\mathrm{A}}$ denotes the lamina scale and $(\bullet)^{\mathrm{bo}}$ corresponds to body waves as $(\bullet)^{\mathrm{fl}}$ corresponds to flexural waves.

The first part of eq. (2.13) defines a limitation on the representative in-plane dimension. In each lamina, the matrix is treated under the long-wavelength assumption whereas the heterogeneities can interact with the flexural or body waves capturing the local resonance effects. The second part of eq. (2.13) defines a limitation on the representative out-of-plane dimension of the unit-cell. By enforcing this limit on the thickness, the thin continuum shell description can be employed. As the body or flexural wavelength increases, the separation of scales in eq. (2.13) will eventually be violated. Since the wavelength is directly related to the frequency, the separation of scales imposes a limitation on the frequency for which the dynamic homogenization framework is still applicable. How to determine this range of homogenizability will be discussed in Chap. 4.

2.4 Dynamic homogenization framework

The scale transition relations are used to couple the macroscale to the microscale and vice versa. First of all, the macro-to-micro (downscaling) transition is used to define lamina-level periodic boundary conditions applicable to the microscopic unit-cell, complementing the microscopic boundary value problem (BVP). Accordingly, the micro-to-macro (upscaling) transition is applied to the solution of the BVP resulting in an expression for the homogenized macroscopic resultants in terms of effective material properties and the macroscopic kinematics.

2.4.1 Downscaling transition

The downscaling transition is initiated by applying the decomposed macroscopic deformation tensors $\hat{\bar{\mathbb{F}}}_{\mathrm{M}}$, $\hat{\bar{\mathbb{K}}}_{\mathrm{M}}$ and $\hat{\tilde{\mathbb{F}}}_{\mathrm{M}}$ to the unit-cell. This leads to a microscopic relative position field of the unit-cell in terms of the macroscopic deformation as

$$\Delta\hat{\tilde{x}}_{\mathrm{m}} = \left[\hat{\bar{\mathbb{F}}}_{\mathrm{M}} + \eta\hat{\bar{\mathbb{K}}}_{\mathrm{M}}\right] \cdot \Delta\hat{\tilde{X}}_{\mathrm{m}} + \Delta\hat{\tilde{w}}_{\mathrm{m}} \tag{2.14a}$$

$$\Delta\hat{\tilde{x}}_{\mathrm{m}} = \hat{\tilde{\mathbb{F}}}_{\mathrm{M}} \cdot \Delta\hat{\tilde{X}}_{\mathrm{m}} - \frac{1}{2}\tilde{e}^{\,\mathrm{c}}\hat{\bar{\mathbb{K}}}_{\mathrm{M}} : \Delta\hat{\tilde{X}}_{\mathrm{m}}\Delta\hat{\tilde{X}}_{\mathrm{m}} + \Delta\hat{\tilde{w}}_{\mathrm{m}} \tag{2.14b}$$

where $\Delta(\vec{\bullet})_{\mathrm{m}} = (\vec{\bullet})_{\mathrm{m}} - (\vec{\bullet})_{\mathrm{m,r}}$. $\Delta\vec{w}_{\mathrm{m}}$ denotes a microscopic fluctuation field accounting for the displacements induced by heterogeneities. As mentioned in Sec. 2.1, the deformation gradient $\hat{\tilde{\mathbb{F}}}_{\mathrm{M}}$ is zero under the corotational laminar basis. Substitution of eq. (2.14) into $\mathbb{F}_{\mathrm{m}} = [\vec{\nabla}_{\mathrm{m},0}\vec{x}_{\mathrm{m}}]^{\mathrm{T}}$ yields an expression for the microscopic lamina-level deformation gradients $\hat{\bar{\mathbb{F}}}^{\,\mathrm{A}}_{\mathrm{m}}(\eta)$ and $\hat{\tilde{\mathbb{F}}}^{\,\mathrm{A}}_{\mathrm{m}}(\eta)$ in terms of the macroscopic deformation gradients and the microscopic fluctuation field $\Delta\vec{w}_{\mathrm{m}}$.

A commonly used relation for scale transition within computational homogenization

is the kinematical averaging relation over the unit-cell volume [28]. However, within the developed framework, only an in-plane avergaging is required since the unit-cell height is equal to the continuum shell thickness. The in-plane kinematic averaging relation states that the macroscopic lamina-level deformation gradient tensor ($\mathbb{F}^{\mathrm{A}}_{\mathrm{M}}(\eta)$) should be equal to the surface average microscopic lamina-level deformation gradient tensor ($\mathbb{F}^{\mathrm{A}}_{\mathrm{m}}(\eta)$) for a lamina at height η. The lamina-level micro-macro coupling of the deformation gradient is then defined as

$$\hat{\mathbb{F}}^{\,\mathrm{A}}_{\mathrm{M}}(\eta) = \frac{1}{A_{\mathrm{m}}(\eta)} \int_{\mathcal{A}_{\mathrm{m}}} \hat{\mathbb{F}}^{\,\mathrm{A}}_{\mathrm{m}}(\eta) \mathrm{d}A_{\mathrm{m}}, \ \forall\ \eta \in \mathcal{H} \tag{2.15a}$$

$$\tilde{\mathbb{F}}^{\,\mathrm{A}}_{\mathrm{M}}(\eta) = \frac{1}{A_{\mathrm{m}}(\eta)} \int_{\mathcal{A}_{\mathrm{m}}} \tilde{\mathbb{F}}^{\,\mathrm{A}}_{\mathrm{m}}(\eta) \mathrm{d}A_{\mathrm{m}}, \ \forall\ \eta \in \mathcal{H} \tag{2.15b}$$

with A_{m} the lamina surface in the initial configuration.

If it is stated that the reference position $\vec{X}_{\mathrm{M,r}}$ is located at the center of the unit-cell and the unit-cell is said to be rectangular, there is an in-plane geometric symmetry for each lamina. Subsequently, η is set to zero and Gauss's theorem is applied to the surface integral to convert it into an integral along the contour of the lamina ($\mathcal{C}_{\mathrm{m}}$ in Fig. 2.2). Eventually, applying the in-plane geometrical symmetry to the integral, one is able to retrieve the in-plane and out-of-plane lamina-level constraint on the micro-fluctuation $\Delta\vec{w}_{\mathrm{m}}$ as

$$\int_{\mathcal{C}_{\mathrm{m}}} \Delta\hat{\vec{w}}_{\mathrm{m}} \hat{\vec{n}}_{\mathrm{m}} \mathrm{d}C_{\mathrm{m}} = \mathbb{O} \tag{2.16a}$$

$$\int_{\mathcal{C}_{\mathrm{m}}} \Delta\tilde{\vec{w}}_{\mathrm{m}} \hat{\vec{n}}_{\mathrm{m}} \mathrm{d}C_{\mathrm{m}} = \mathbb{O} \tag{2.16b}$$

where $\vec{n}_{\mathrm{m}}$ is the normal vector pointing in the outward direction.

In order to satisfy eq. (2.16), periodic boundary conditions are applied to the unit-cell. Other methods can also be applied like uniform displacement boundary conditions. Yet, periodic boundary conditions have proven to show great results for equal unit-cell sizes compared to other approaches [33]. It should be noted that the periodic boundary conditions are only valid as long as the separation of scales is satisfied. Considering the unit-cell shown in Fig. 2.2b, two sets of opposing in-plane boundaries can be defined, namely the left-right set and the back-front set, denoted by the outward directed normal vectors $\vec{n}^{\mathrm{L}}_{\mathrm{m}}$, $\vec{n}^{\mathrm{R}}_{\mathrm{m}}$ and $\vec{n}^{\mathrm{B}}_{\mathrm{m}}$, $\vec{n}^{\mathrm{F}}_{\mathrm{m}}$, respectively. For these boundary pairs, there is an in-plane geometric periodicity on one hand and on the other hand, there is the anti-periodicity of the normal vectors. This means that eq. (2.16) is satisfied if the following requirement on $\Delta\vec{w}_{\mathrm{m}}$ holds

$$\Delta\hat{\vec{w}}^{+}_{\mathrm{m}}(\xi,\eta) = \Delta\hat{\vec{w}}^{+}_{\mathrm{m}}(\xi,\eta) \tag{2.17a}$$

$$\Delta\tilde{\vec{w}}^{+}_{\mathrm{m}}(\xi,\eta) = \Delta\tilde{\vec{w}}^{+}_{\mathrm{m}}(\xi,\eta), \forall(\xi,\eta) \in (\mathcal{C}_{\mathrm{m}}, \mathcal{H}) \tag{2.17b}$$

Here, the superscript $(\bullet)^{-}$ can be replaced by $(\bullet)^{\mathrm{L}}$ and $(\bullet)^{\mathrm{B}}$ and superscript $(\bullet)^{+}$ can be replaced by $(\bullet)^{\mathrm{R}}$ and $(\bullet)^{\mathrm{F}}$, respectively and ξ denotes the in-plane coordinate along the lamina contour (Fig. 2.2). Hence, eq. (2.17) can be considered as the periodic boundary conditions applicable to the unit-cell due to its geometric periodicity. A more detailed description of the periodic boundary conditions will be given in Chap. 3.

The microscopic displacement field is computed by solving the microscopic weak form in eq. (2.12). To this extent, eq. 2.14 is used to express the periodic boundary conditions in terms of the unit-cell boundary displacement. Furthermore, the plane stress state is assumed in the Kirchoff-Love theory which implies that the top and bottom surface are traction free.

The top and bottom surface are denoted by the outward directed normal vectors $\vec{n}_{\mathrm{m}}^{\mathrm{T}}$ and $\vec{n}_{\mathrm{m}}^{\mathrm{D}}$ in Fig. 2.2. The traction-free requirement is written as

$$\vec{t}_{\mathrm{m}}^{\,\mathrm{T}} = \vec{0} \wedge \vec{t}_{\mathrm{m}}^{\,\mathrm{D}} = \vec{0} \tag{2.18}$$

with the superscripts $(\bullet)^{\mathrm{T}}$ and $(\bullet)^{\mathrm{D}}$ for the top and bottom surface of the unit-cell respectively. With these boundary conditions, the microscopic BVP is completed and it can be solved for the microscopic stresses and kinematics.

2.4.2 Upscaling transition

A modified Hill-Mandel condition is used to upscale the microscopic kinematics and stresses towards macroscopic resultant quantities. In general, the Hill-Mandel condition states that the microscopic volume average of virtual work on the unit-cell must equate the virtual work on the corresponding macroscopic point [34]. For a shell continuum, the resultant quantities are determined after a through thickness integration. Hence, for the shell continuum the Hill-Mandel principle is considered as the surface average of virtual work on the unit-cell reference plane $\delta W_{\mathrm{m}}^{\mathrm{A}}$ being equal to the virtual work along the corresponding macroscopic fibre $\delta W_{\mathrm{M}}^{\mathrm{A}}$ [30]. This is defined as

$$\delta W_{\mathrm{m}}^{\mathrm{A}}(\delta\vec{u}_{\mathrm{M}}) = \delta W_{\mathrm{M}}^{\mathrm{A}}(\delta\vec{u}_{\mathrm{M}}), \qquad \forall\ \delta\vec{u}_{\mathrm{m}} \in \mathcal{U}^1 \tag{2.19}$$

The surface average of virtual work on the unit-cell reference lamina can be decomposed in an ambient and local term. The ambient work on the unit-cell is related to the macroscopic displacement field. The local work on the unit-cell is related to the microscopic deformation and can be defined from the weak form problem (eq. (2.12)). Expanding the virtual work on the unit-cell reference lamina into the local and ambient terms and applying Gauss's theorem, one obtains the microscopic virtual work in terms of quantities on the transverse unit-cell boundaries. The macroscopic virtual work is obtained from the macroscopic weak form eq. (2.6). The virtual work on micro and macroscale is then written as

$$\delta W_{\mathrm{m}}^{\mathrm{A,loc}} = \frac{1}{A_{\mathrm{m,r}}} \int_{\tilde{\mathcal{S}}_{\mathrm{m}}} \vec{t}_{\mathrm{m}} \cdot \delta\Delta\vec{x}_{\mathrm{m}} \mathrm{d}S_{\mathrm{m}} \tag{2.20a}$$

$$\delta W_{\mathrm{m}}^{\mathrm{A,amb}} = \frac{1}{A_{\mathrm{m,r}}} \int_{\tilde{\mathcal{S}}_{\mathrm{m}}} \vec{t}_{\mathrm{m}} \cdot \delta\vec{u}_{\mathrm{M}} \mathrm{d}S_{\mathrm{m}} \tag{2.20b}$$

$$\delta W_{\mathrm{M}}^{\mathrm{A}} = \hat{\hat{\mathbb{N}}}_{\mathrm{M}} : \delta\hat{\hat{\vec{\nabla}}}_{\mathrm{M}}\hat{\vec{u}}_{\mathrm{M,r}} + \hat{\hat{\mathbb{M}}}_{\mathrm{M}} : \delta\hat{\hat{\vec{\nabla}}}_{\mathrm{M}}\hat{\vec{b}}_{\mathrm{M}} + \dot{\vec{P}}_{\mathrm{M}} \cdot \delta\vec{u}_{\mathrm{M,r}} + \dot{\vec{Q}}_{\mathrm{M}} \cdot \delta\vec{b}_{\mathrm{M}} \tag{2.20c}$$

Here, the superscripts $(\bullet)^{\mathrm{loc}}$ and $(\bullet)^{\mathrm{amb}}$ denote the local and ambient contribution to the total virtual work. The fields $\delta\Delta\vec{x}_{\mathrm{m}}$ and $\delta\vec{u}_{\mathrm{M}}$ denote the local and ambient term of the virtual displacement $\delta\vec{u}_{\mathrm{m}}$, respectively. The lamina-level relative position field $\Delta\vec{x}_{\mathrm{m}}$ defined in the downscaling transition can be inserted in eq. (2.20(a)). The macroscopic virtual displacement $\delta\vec{u}_{\mathrm{M}}$ is split into a virtual reference plane displacement and virtual fibre rotation. Finally, the rewritten eqs. (2.20(a-b)) and eq. (2.20(c)) are substituted into eq. (2.19). This concludes the upscaling and results in the homogenized macroscopic resultants in terms of

the microscopic kinematics and stresses on the transverse unit-cell boundaries as

$$\hat{\mathbb{N}}_{\mathrm{M}} = \frac{1}{A_{\mathrm{m,r}}} \int_{\tilde{\mathcal{S}}_{\mathrm{m}}} \hat{\vec{t}}_{\mathrm{m}} \Delta \hat{\vec{X}}_{\mathrm{m}} \mathrm{d}S_{\mathrm{m}} \tag{2.21a}$$

$$\hat{\mathbb{M}}_{\mathrm{M}} = \frac{1}{A_{\mathrm{m,r}}} \int_{\tilde{\mathcal{S}}_{\mathrm{m}}} \eta \hat{\vec{t}}_{\mathrm{m}} \Delta \hat{\vec{X}}_{\mathrm{m}} \mathrm{d}S_{\mathrm{m}} \tag{2.21b}$$

$$\dot{P}_{\mathrm{m}} = \frac{1}{A_{\mathrm{m,r}}} \int_{\tilde{\mathcal{S}}_{\mathrm{m}}} \hat{\vec{t}}_{\mathrm{m}} \mathrm{d}S_{\mathrm{m}} \tag{2.21c}$$

$$\dot{Q}_{\mathrm{m}} = \frac{1}{A_{\mathrm{m,r}}} \int_{\tilde{\mathcal{S}}_{\mathrm{m}}} \eta \hat{\vec{t}}_{\mathrm{m}} \mathrm{d}S_{\mathrm{m}} \tag{2.21d}$$

where $\tilde{\mathcal{S}}_{\mathrm{m}}$ denotes the transverse boundary of the unit-cell. This means that only the stresses and kinematic states at the unit-cell boundary are necessary for computing the macroscopic resultants. The out-of-plane traction in eq. (2.21b) is neglected with respect to the in-plane tractions. This is done since the out-of-plane traction is related to the transverse shear deformation in the shell and this was assumed to be zero. Yet, for the linear and rotational momentum, this assumption on the transverse shear deformation is ignored. The out-of-plane traction is important in the kinematic description since it encompasses the out-of-plane inertia. Hence, the macroscopic stress and couple-stress resultants are defined in terms of in-plane traction only, whereas for the linear and rotational momentum the full traction-term is taken into account.

Chapter 3

Enriched continuum shell description

The microscopic boundary value problem will be implemented within a finite element - framework (FEM). To this extent, the kinematic description and the microscopic weak form are discretised after which the periodic boundary conditions are applied. Subsequently, the Craig-Bampton mode synthesis is applied to the system of equations to efficiently capture the micro-inertia effects of the LRAM unit-cell [35]. Since the periodic boundary conditions are applied to the unit-cell, the macroscopic quantities can be expressed by the kinematics and stresses of those prescribed nodes only. What remains is a set of expressions for the macroscopic resultant quantities in terms of the macroscopic kinematics and the effective material properties corresponding to the LRAM unit-cell. A mode selection criterion is used to determine the minimal number of eigenmodes required to capture the internal dynamics. The result is an enriched single-scale continuum shell description on the macroscale.

3.1 Implementing the microscopic BVP

3.1.1 Finite element discretisation

The analysis of the microscopic unit-cell is restricted to small deformations. Both the matrix and the heterogeneities are modelled as linear elastic material. This means that the constitutive material law introduced in eq. 2.11 is written as

$$\boldsymbol{\sigma}_{\mathrm{m}}(\vec{x}_{\mathrm{m}}) =^{4} \mathbb{C}_{\mathrm{m}}(\vec{x}_{\mathrm{m}}) : \boldsymbol{\varepsilon}_{\mathrm{m}}(\vec{x}_{\mathrm{m}}) \tag{3.1}$$

with ${}^{4}\mathbb{C}_{\mathrm{m}}$ the fourth-order material elasticity tensor and $\boldsymbol{\varepsilon}_{\mathrm{m}}$ the microscopic strain tensor. By applying the standard finite element discretization to the microscopic balance of linear momentum (eq. (2.12)), one obtains a set of discrete balance equations written as

$$\underline{\mathbb{B}}_{\mathrm{m}} \cdot \underset{\sim}{\vec{u}}_{\mathrm{m}} + \underline{\mathbb{W}}_{\mathrm{m}} \cdot \underset{\sim}{\ddot{\vec{u}}}_{\mathrm{m}} = \underset{\sim}{\vec{f}}_{\mathrm{m}} \tag{3.2}$$

where $\underline{\mathbb{B}}_{\mathrm{m}}$ is the assembled stiffness tensor matrix, $\underline{\mathbb{W}}_{\mathrm{m}}$ the assembled mass tensor matrix and $\underset{\sim}{\vec{u}}_{\mathrm{m}}$ and $\underset{\sim}{\vec{f}}_{\mathrm{m}}$ denote the vector column with nodal values of respectively linear displacements and forces. For computational efficiency, the isoparametric mapping is used to analyse each element in terms of normalized coordinates. Numerical integration is used to compute the stiffness and mass tensor matrices and the force vector columns according to the Gauss quadrature rule. Hereafter, boundary conditions defined in eq. (2.17-2.18)) must be applied to the discretized unit-cell. Applying stress-free top and bottom surface is relatively easy. The derivation of the lamina-level periodic boundary conditions (PBCs) is elaborated next.

3.1.2 Lamina-level periodic boundary conditions

To solve the discretised balance equations in eq. (3.2), the lamina-level periodic boundary conditions are applied to the unit-cell. These boundary conditions connect displacements of opposing unit-cell boundaries shown in Fig. 2.2. The lamina-level periodic boundary conditions are enforced by satisfying the periodicity of the microfluctuation field $\Delta\vec{w}_{\mathrm{m}}$ between opposite boundaries. First of all eq. (2.14) is substituted into eq. (2.17), resulting in the following expression which relates the displacements of opposing boundaries to each other. This is written as

$$\hat{\tilde{u}}_{\mathrm{m}}^{+} - \hat{\tilde{u}}_{\mathrm{m}}^{-} = \left[\hat{\mathbb{H}}_{\mathrm{M}} + \eta\hat{\mathbb{K}}_{\mathrm{M}}\right] \cdot \left[\hat{\tilde{X}}_{\mathrm{m}}^{+} - \hat{\tilde{X}}_{\mathrm{m}}^{-}\right] \tag{3.3a}$$

$$\tilde{\tilde{u}}_{\mathrm{m}}^{+} - \tilde{\tilde{u}}_{\mathrm{m}}^{-} = -\frac{1}{2}\vec{e}_2^{\,\mathrm{t}}\hat{\mathbb{K}}_{\mathrm{M}} : \left[\hat{\tilde{X}}_{\mathrm{m}}^{+}\hat{\tilde{X}}_{\mathrm{m}}^{+} - \hat{\tilde{X}}_{\mathrm{m}}^{-}\hat{\tilde{X}}_{\mathrm{m}}^{-}\right] \tag{3.3b}$$

Here $\hat{\mathbb{H}}_{\mathrm{M}} = \hat{\mathbb{F}}_{\mathrm{M}} - \hat{\mathbb{I}}$ denotes the in-plane displacement gradient tensor and $(\bullet)^{+}$ and $(\bullet)^{-}$ denote a pair of tied opposite unit-cell boundaries. To prevent rigid body motions, the micro-fluctuations of two nodes are fixed. The nodes must satisfy the following conditions. First of all, the nodes must not be located on the heterogeneities since these heterogeneities might exert large fluctuations at the microscale as a result of the local resonance effects. Secondly, the nodes must be located on separate laminae such that rotation around the longitudinal axis of the fibre is not possible. Satisfying both criteria, the micro-fluctuations of nodes 1 and 5 in Fig. 2.2 are fixed. This means that the displacements of these nodes are written as $\vec{u}_{\mathrm{m},1} = \vec{u}_{\mathrm{M},1} + \mathbb{H}_{\mathrm{M},1} \cdot \vec{X}_{\mathrm{m},1}$ and $\vec{u}_{\mathrm{m},5} = \vec{u}_{\mathrm{M},5} + \mathbb{H}_{\mathrm{M},5} \cdot \vec{X}_{\mathrm{m},5}$. Employing the in-plane lamina-level geometric symmetry of the unit-cell and substituting the expression for $\vec{u}_{\mathrm{m},1}$ into eq. (3.3) results in an expression for the prescribed displacements of nodes 1, 2 and 4 written as

$$\hat{\tilde{u}}_{\mathrm{m},i} = \left[\hat{\mathbb{H}}_{\mathrm{M}} + \eta_1\hat{\mathbb{K}}_{\mathrm{M}}\right] \cdot \hat{\tilde{X}}_{\mathrm{m},i} + \hat{\tilde{u}}_{\mathrm{M},1} \tag{3.4a}$$

$$\tilde{\tilde{u}}_{\mathrm{m},i} = -\frac{1}{2}\vec{e}_2^{\,\mathrm{t}}\hat{\mathbb{K}}_{\mathrm{M}} : \left[\hat{\tilde{X}}_{\mathrm{m},i}\hat{\tilde{X}}_{\mathrm{m},i}\right] + \tilde{\tilde{u}}_{\mathrm{M},1} \tag{3.4b}$$

with $i = 1, 2, 4$ all located at the bottom lamina. To obtain the prescribed displacements of nodes 5, 6 and 8, the expression for $\vec{u}_{\mathrm{m},5}$ is substituted into eq. (3.3). The prescribed displacements of nodes 5, 6 and 8 are then written as

$$\hat{\tilde{u}}_{\mathrm{m},i} = \left[\hat{\mathbb{H}}_{\mathrm{M}} + \eta_5\hat{\mathbb{K}}_{\mathrm{M}}\right] \cdot \hat{\tilde{X}}_{\mathrm{m},i} + \hat{\tilde{u}}_{\mathrm{M},5} \tag{3.5a}$$

$$\tilde{\tilde{u}}_{\mathrm{m},i} = -\frac{1}{2}\vec{e}_2^{\,\mathrm{t}}\hat{\mathbb{K}}_{\mathrm{M}} : \left[\hat{\tilde{X}}_{\mathrm{m},i}\hat{\tilde{X}}_{\mathrm{m},i}\right] + \tilde{\tilde{u}}_{\mathrm{M},5} \tag{3.5b}$$

with $i = 5, 6, 8$ all located at the top lamina. Eqs. (3.4) and (3.5) are substituted into eq. (3.3). Re-arranging the equations then eventually results in the lamina-level tying constraints between opposite unit-cell boundaries in terms of the prescribed corner nodes and macroscopic deformation gradients. The in-plane and out-of-plane tying constraints on transverse boundaries are written as

$$\hat{\tilde{u}}_{\mathrm{m}}^{\mathrm{F}} = \hat{\tilde{u}}_{\mathrm{m}}^{\mathrm{B}} + \left[\frac{1}{2} - \frac{\eta}{H}\right]\left[\hat{\tilde{u}}_{\mathrm{m},4} - \hat{\tilde{u}}_{\mathrm{m},1}\right] + \left[\frac{1}{2} + \frac{\eta}{H}\right]\left[\hat{\tilde{u}}_{\mathrm{m},8} - \hat{\tilde{u}}_{\mathrm{m},5}\right] \tag{3.6a}$$

$$\hat{\tilde{u}}_{\mathrm{m}}^{\mathrm{R}} = \hat{\tilde{u}}_{\mathrm{m}}^{\mathrm{L}} + \left[\frac{1}{2} - \frac{\eta}{H}\right]\left[\hat{\tilde{u}}_{\mathrm{m},2} - \hat{\tilde{u}}_{\mathrm{m},1}\right] + \left[\frac{1}{2} + \frac{\eta}{H}\right]\left[\hat{\tilde{u}}_{\mathrm{m},6} - \hat{\tilde{u}}_{\mathrm{m},5}\right] \tag{3.6b}$$

$$\tilde{\tilde{u}}_{\mathrm{m}}^{\mathrm{F}} = \tilde{\tilde{u}}_{\mathrm{m}}^{\mathrm{B}} - \frac{2\xi_1}{L_{\mathrm{m}}}\left[\tilde{\tilde{u}}_{\mathrm{m},4} - \tilde{\tilde{u}}_{\mathrm{m},1}\right] \tag{3.6c}$$

$$\tilde{\tilde{u}}_{\mathrm{m}}^{\mathrm{R}} = \tilde{\tilde{u}}_{\mathrm{m}}^{\mathrm{L}} - \frac{2\xi_3}{W_{\mathrm{m}}}\left[\tilde{\tilde{u}}_{\mathrm{m},2} - \tilde{\tilde{u}}_{\mathrm{m},1}\right] \tag{3.6d}$$

with ξ_1 and ξ_3 denoting the in-plane coordinates along the $\vec{e}_1^{\,\mathrm{t}}$- and $\vec{e}_3^{\,\mathrm{t}}$-direction, respectively, as indicted in Fig. 2.2. The tying relations applicable to the opposing edges of the unit-cell are slightly different from those applicable to the opposing boundaries and they are written as

$$\hat{\tilde{u}}_{\mathrm{m}}^{\mathrm{RB}} = \hat{\tilde{u}}_{\mathrm{m}}^{\mathrm{LB}} + \left[\frac{1}{2} - \frac{\eta}{H}\right]\left[\hat{\tilde{u}}_{\mathrm{m},2} - \hat{\tilde{u}}_{\mathrm{m},1}\right] + \left[\frac{1}{2} + \frac{\eta}{H}\right]\left[\hat{\tilde{u}}_{\mathrm{m},6} - \hat{\tilde{u}}_{\mathrm{m},5}\right] \tag{3.7a}$$

$$\hat{\tilde{u}}_{\mathrm{m}}^{\mathrm{LF}} = \hat{\tilde{u}}_{\mathrm{m}}^{\mathrm{LB}} + \left[\frac{1}{2} - \frac{\eta}{H}\right]\left[\hat{\tilde{u}}_{\mathrm{m},4} - \hat{\tilde{u}}_{\mathrm{m},1}\right] + \left[\frac{1}{2} + \frac{\eta}{H}\right]\left[\hat{\tilde{u}}_{\mathrm{m},8} - \hat{\tilde{u}}_{\mathrm{m},5}\right] \tag{3.7b}$$

$$\hat{\tilde{u}}_{\mathrm{m}}^{\mathrm{RF}} = \hat{\tilde{u}}_{\mathrm{m}}^{\mathrm{LB}} + \left[\frac{1}{2} - \frac{\eta}{H}\right]\left[\hat{\tilde{u}}_{\mathrm{m},4} + \hat{\tilde{u}}_{\mathrm{m},2} - 2\hat{\tilde{u}}_{\mathrm{m},1}\right] + \left[\frac{1}{2} + \frac{\eta}{H}\right]\left[\hat{\tilde{u}}_{\mathrm{m},8} + \hat{\tilde{u}}_{\mathrm{m},6} - 2\hat{\tilde{u}}_{\mathrm{m},5}\right] \tag{3.7c}$$

$$\tilde{\tilde{u}}_{\mathrm{m}}^{\mathrm{RB}} = \tilde{\tilde{u}}_{\mathrm{m}}^{\mathrm{LB}} - \frac{2\xi_3}{W_{\mathrm{m}}}\left[\tilde{\tilde{u}}_{\mathrm{m},2} - \tilde{\tilde{u}}_{\mathrm{m},1}\right] \tag{3.7d}$$

$$\tilde{\tilde{u}}_{\mathrm{m}}^{\mathrm{LF}} = \tilde{\tilde{u}}_{\mathrm{m}}^{\mathrm{LB}} - \frac{2\xi_1}{L_{\mathrm{m}}}\left[\tilde{\tilde{u}}_{\mathrm{m},4} - \tilde{\tilde{u}}_{\mathrm{m},1}\right] \tag{3.7e}$$

$$\tilde{\tilde{u}}_{\mathrm{m}}^{\mathrm{RF}} = \tilde{\tilde{u}}_{\mathrm{m}}^{\mathrm{LB}} - \frac{2\xi_1}{L_{\mathrm{m}}}\left[\tilde{\tilde{u}}_{\mathrm{m},4} - \tilde{\tilde{u}}_{\mathrm{m},1}\right] - \frac{2\xi_3}{W_{\mathrm{m}}}\left[\tilde{\tilde{u}}_{\mathrm{m},2} - \tilde{\tilde{u}}_{\mathrm{m},1}\right] \tag{3.7f}$$

with the subscript $(\bullet)_{\mathrm{RB}}$ indicating the edge between the right and back boundary of the unit-cell, $(\bullet)_{\mathrm{LF}}$ the edge between the left and front boundary etc. Note that in eq. (3.7(f)) the coordinate ξ_1 corresponds to the opposite node on the LF-edge and ξ_3 corresponds to the unknown node on the RF-edge.

Summarizing eqs. (3.4)-(3.7), the prescribed displacements of the unit-cell are expressed in terms of the macroscopic kinematic fields $\vec{u}_{\mathrm{M,r}}$ and $\vec{b}_{\mathrm{M}}$, the in-plane macroscopic deformation gradient tensors $\hat{\tilde{\mathbb{H}}}_{\mathrm{M}}$ and $\hat{\tilde{\mathbb{K}}}_{\mathrm{M}}$ and the in-plane coordinates of the prescribed nodes. The tying relations between independent and dependent nodes can be re-arranged into a so-called dependency matrix $\underline{\mathbf{T}}_{\mathrm{m,di}}$ as $\vec{\underset{\sim}{u}}_{\mathrm{m,d}} = \underline{\mathbf{T}}_{\mathrm{m,di}}\vec{\underset{\sim}{u}}_{\mathrm{m,i}}$ with subscripts $(\bullet)_{\mathrm{i}}$ and $(\bullet)_{\mathrm{d}}$ denoting the independent and dependent nodes, respectively. The independent nodes are defined at the right-hand side of the equal sign in eq. (3.6-3.7) whereas the dependent nodes are defined at the left-hand side. Then by partitioning eq. (3.2) into the independent and dependent nodes and substituting the dependency matrix, one can obtain the reduced discretised balance equations merely in terms of independent nodes, reading

$$\underline{\mathbb{B}}_{\mathrm{m}}^{*} \cdot \vec{\underset{\sim}{u}}_{\mathrm{m,i}} + \underline{\mathbb{W}}_{\mathrm{m}}^{*} \cdot \ddot{\underset{\sim}{u}}_{\mathrm{m,i}} = \vec{\underset{\sim}{f}}_{\mathrm{m,i}}^{*} \tag{3.8}$$

with the reduced stiffness and mass tensor matrix and the reduced external force vector column written as

$$\underline{\mathbb{B}}_{\mathrm{m}}^{*} = \underline{\mathbb{B}}_{\mathrm{m,ii}} + \underline{\mathbf{T}}_{\mathrm{m,di}}^{\mathrm{T}}\underline{\mathbb{B}}_{\mathrm{m,di}} + \underline{\mathbb{B}}_{\mathrm{m,id}}\underline{\mathbf{T}}_{\mathrm{m,di}} + \underline{\mathbf{T}}_{\mathrm{m,di}}^{\mathrm{T}}\underline{\mathbb{B}}_{\mathrm{m,dd}}\underline{\mathbf{T}}_{\mathrm{m,di}} \tag{3.9a}$$

$$\underline{\mathbb{W}}_{\mathrm{m}}^{*} = \underline{\mathbb{W}}_{\mathrm{m,ii}} + \underline{\mathbf{T}}_{\mathrm{m,di}}^{\mathrm{T}}\underline{\mathbb{W}}_{\mathrm{m,di}} + \underline{\mathbb{W}}_{\mathrm{m,id}}\underline{\mathbf{T}}_{\mathrm{m,di}} + \underline{\mathbf{T}}_{\mathrm{m,di}}^{\mathrm{T}}\underline{\mathbb{W}}_{\mathrm{m,dd}}\underline{\mathbf{T}}_{\mathrm{m,di}} \tag{3.9b}$$

$$\vec{\underset{\sim}{f}}_{\mathrm{m,i}}^{*} = \vec{f}_{\mathrm{m,i}} + \underline{\mathbf{T}}_{\mathrm{m,di}}^{\mathrm{T}}\vec{f}_{\mathrm{m,d}} \tag{3.9c}$$

3.2 Craig-Bampton mode synthesis

To solve the discretised microscopic BVP, one might simply insert the prescribed displacements defined in eq. (3.4-3.5) into the discretised system in eq. (3.9). Yet, due to the time-dependency of the simulation and the large number of degrees of freedom of the unit-cell, the computational expense might still be large. To this extent, the Craig-Bampton mode synthesis (CBMS) is introduced. It describes the internal dynamic response to prescribed

boundary conditions on the unit-cell boundary. Considering the unit-cell as a building block of the macroscopic structure, the global response of the macroscopic structure can be captured by assembling the individual response of each unit-cell at its boundaries. This method is applicable to LRAMs, provided that the matrix is sufficiently stiff and does not respond to local dynamic response of the heterogeneities at the microscale. Due to the long-wavelength assumption on the matrix this is valid for the current framework. Since the unit-cell can be treated as a building block of the macroscopic structure, the CBMS is applied to the multi-scale description of LRAM plates.

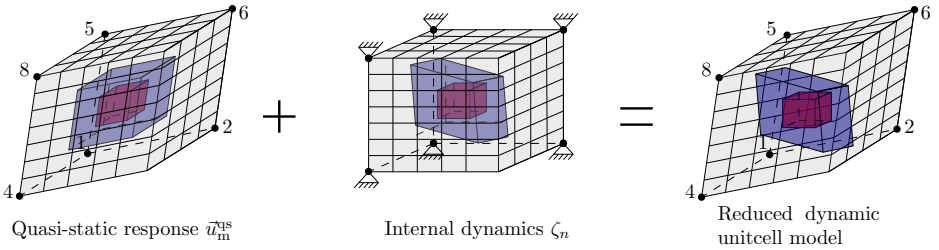

Figure 3.1: *Schematic representation of the Craig Bampton mode synthesis for the LRAM unit-cell.*

In Fig. 3.1 the mode synthesis is illustrated. It shows that the total dynamic response of the unit-cell under prescribed displacements is a superposition of two components. The first one is the quasi-static response under the prescribed displacements where local inertia effects are not taken into account. The other component is a reduced basis of eigenmodes representing the internal dynamics in each unit-cell with the prescribed nodes fixed. To define the reduced dynamic unit-cell model, first the independent nodes are split into prescribed and free nodes, indicated by the subscripts $(\bullet)_{\mathrm{p}}$ and $(\bullet)_{\mathrm{f}}$, respectively. The partitioned system of equations is then written as

$$\begin{bmatrix} \underline{\mathbb{B}}^*_{\mathrm{m,pp}} & \underline{\mathbb{B}}^*_{\mathrm{m,pf}} \\ \underline{\mathbb{B}}^*_{\mathrm{m,fp}} & \underline{\mathbb{B}}^*_{\mathrm{m,ff}} \end{bmatrix} \cdot \begin{bmatrix} \vec{u}_{\mathrm{m,p}} \\ \vec{u}_{\mathrm{m,f}} \end{bmatrix} + \begin{bmatrix} \underline{\mathbb{W}}^*_{\mathrm{m,pp}} & \underline{\mathbb{W}}^*_{\mathrm{m,pf}} \\ \underline{\mathbb{W}}^*_{\mathrm{m,fp}} & \underline{\mathbb{W}}^*_{\mathrm{m,ff}} \end{bmatrix} \cdot \begin{bmatrix} \ddot{\vec{u}}_{\mathrm{m,p}} \\ \ddot{\vec{u}}_{\mathrm{m,f}} \end{bmatrix} = \begin{bmatrix} \vec{f}_{\mathrm{m,p}} \\ \vec{0}_{\mathrm{m,f}} \end{bmatrix} \tag{3.10}$$

Note that in the resulting eq. (3.10) the external forces on the free nodes $\underset{\sim}{\vec{f}}_{\mathrm{m,f}}$ are 0 since the tying constraints are removed. The individual components of the reduced dynamic description are evaluated separately first after which they are superposed to yield the full response.

3.2.1 Quasi-static response

The quasi-static response is obtained by neglecting the inertia contributions of the unit-cell. The prescribed corner nodes lie on the matrix, hence the quasi-static response of these nodes is equal to the prescribed displacements. To compute the quasi-static response of the free nodes, the static condensate tensor matrix $\underline{\mathbb{S}}$ of the reduced stiffness tensor matrix $\underline{\mathbb{B}}^*_{\mathrm{m}}$ is used. The quasi-static response of the unit-cell can be written as

$$\begin{bmatrix} \vec{u}^{\mathrm{qs}}_{\mathrm{m,p}} \\ \vec{u}^{\mathrm{qs}}_{\mathrm{m,f}} \end{bmatrix} = \begin{bmatrix} \underline{\mathbb{I}}_{\mathrm{m,p}} \\ \underline{\mathbb{S}} \end{bmatrix} \cdot \underset{\sim}{\vec{u}}_{\mathrm{m,p}} \tag{3.11}$$

where the static condensate tensor matrix is defined as

$$\underline{\mathbb{S}} = -\left[\underline{\mathbb{B}}^*_{\mathrm{m,ff}}\right]^{-1} \cdot \underline{\mathbb{B}}^*_{\mathrm{m,fp}} \tag{3.12}$$

and the supercript $(\bullet)^{\mathrm{qs}}$ denotes the quasi-static response. Then by substituting eq. (3.11) into eq. (3.10), the set of discretised balance equations for the quasi-static response is expressed merely in terms of the prescribed nodes as

$$\underline{\mathbb{B}}_{\mathrm{m}}^{\mathrm{qs}} \cdot \underset{\sim}{\vec{u}}_{\mathrm{m,p}} + \underline{\mathbb{W}}_{\mathrm{m}}^{\mathrm{qs}} \cdot \underset{\sim}{\ddot{\vec{u}}}_{\mathrm{m,p}} = \underset{\sim}{\vec{f}}^{*}_{\mathrm{m,p}} \tag{3.13}$$

with

$$\underline{\mathbb{B}}_{\mathrm{m}}^{\mathrm{qs}} = \underline{\mathbb{B}}^{*}_{\mathrm{m,pp}} + \underline{\mathbb{B}}^{*}_{\mathrm{m,pf}} \cdot \underline{\mathbb{S}} \tag{3.14a}$$

$$\underline{\mathbb{W}}_{\mathrm{m}}^{\mathrm{qs}} = \underline{\mathbb{W}}^{*}_{\mathrm{m,pp}} + 2\underline{\mathbb{W}}^{*}_{\mathrm{m,pf}} \cdot \underline{\mathbb{S}} + \underline{\mathbb{S}}^{\mathrm{T}} \cdot \underline{\mathbb{W}}^{*}_{\mathrm{m,ff}} \cdot \underline{\mathbb{S}} \tag{3.14b}$$

3.2.2 Internal dynamics

The micro-inertia effects of the heterogeneities are not taken into account in the quasi-static response. Since these effects are the cornerstone for the attenuating performance of LRAMs, it is important to capture them accurately. To incorporate the inertia effects of the heterogeneities, its inertial response is added to the quasi-static response as a set of N_{d} eigenmodes. These eigenmodes can be determined by fixing the prescribed nodes, located at the matrix. The displacement field of the unit-cell can then be described as

$$\begin{bmatrix} \vec{u}^{\mathrm{dy}}_{\mathrm{m,p}} \\ \vec{u}^{\mathrm{dy}}_{\mathrm{m,f}} \end{bmatrix} = \begin{bmatrix} \vec{0}_{\mathrm{m,p}} \\ \underline{\vec{\phi}} \end{bmatrix} \underset{\sim}{\zeta} \tag{3.15}$$

where the superscript $(\bullet)^{\mathrm{dy}}$ denotes dynamic response. The vector matrix $\underline{\vec{\phi}}$, contains the normalized modal displacement field of the free nodes in which each column represents the displacement field ($\underset{\sim}{\vec{\phi}}n$) corresponding to eigenmode n with $n = 1, 2, ..., N_{\mathrm{d}}$. The column vector $\underset{\sim}{\zeta}$ represents the displacement amplitude with each entry ζ_n corresponding to eigenmode n. By fixing the prescribed nodes and substituting a harmonic solution for the free displacements into eq. (3.10), the eigenvalue problem together with the normalized mass condition is formulated as

$$\left[\underline{\mathbb{B}}^{*}_{\mathrm{m,ff}} - \omega_n^2 \underline{\mathbb{W}}^{*}_{\mathrm{m,ff}}\right] \cdot \underset{\sim}{\vec{\phi}}_n = \underset{\sim}{\vec{0}}_{m,f} \tag{3.16a}$$

$$\underset{\sim}{\vec{\phi}}_n^{\mathrm{T}} \cdot \underline{\mathbb{W}}^{*}_{\mathrm{m,ff}} \cdot \underset{\sim}{\vec{\phi}}_n = 1 \tag{3.16b}$$

for $n = 1, 2, ..., N_{\mathrm{d}}$. Then the resonance frequency corresponding to eigenmode n is given by ω_n. The CBMS is used in this framework to reduce computational costs of analysing the time-dependent problem. Therefore, the number of eigenmodes is minimized, resulting in a reduced basis of eigenmodes containing only those eigenmodes with lowest eigenfrequencies. To this extent, a mode selection criterion was introduced in [31] and extended towards double negative LRAMs in [29] and [36].

3.2.3 Full dynamic response

Superposing eqs. (3.11) and (3.15) results in the full dynamic response of the independent nodes of the unit-cell, reading

$$\begin{bmatrix} \vec{u}_{\mathrm{m,p}} \\ \vec{u}_{\mathrm{m,f}} \end{bmatrix} = \begin{bmatrix} \underline{\mathbb{I}}_{\mathrm{m,p}} & \vec{0}_{\mathrm{m,p}} \\ \underline{\mathbb{S}} & \underline{\vec{\phi}} \end{bmatrix} \cdot \begin{bmatrix} \vec{u}_{\mathrm{m,p}} \\ \underset{\sim}{\zeta} \end{bmatrix} \tag{3.17}$$

Substituting eq. (3.17) into the partitioned set of balance equations (eq. (3.10)), results in the reduced coupled dynamic description of the microscopic unit-cell, reading

$$\underset{\sim}{\omega}^2_{\mathrm{res}}\underset{\sim}{\zeta} + \underset{\sim}{\ddot{\zeta}} = -\left[\underline{\vec{W}}\right]^{\mathrm{T}} \cdot \underset{\sim}{\ddot{u}}_{\mathrm{m,p}} \tag{3.18a}$$

$$\underline{\mathbb{B}}^{\mathrm{qs}}_{\mathrm{m}} \cdot \underset{\sim}{\vec{u}}_{\mathrm{m,p}} + \underline{\mathbb{W}}^{\mathrm{qs}}_{\mathrm{m}} \cdot \underset{\sim}{\ddot{\vec{u}}}_{\mathrm{m,p}} + \underline{\vec{W}}\underset{\sim}{\ddot{\zeta}} = \underset{\sim}{\vec{f}}_{\mathrm{m,p}} \tag{3.18b}$$

with $\underline{\vec{W}}$ the coupling vector matrix which provides the coupling between equations (3.18(a)) and (3.18(b)). $\underline{\vec{W}}$ is defined as

$$\underline{\vec{W}} = \underline{\mathbb{S}}^{\mathrm{CT}} \cdot \underline{\mathbb{W}}^{*}_{\mathrm{m,ff}} \cdot \underline{\vec{\phi}} + \underline{\mathbb{I}}_{\mathrm{m,p}} \cdot \underline{\mathbb{W}}^{*}_{\mathrm{m,pf}} \cdot \underline{\vec{\phi}} \tag{3.19}$$

The matrix $\underline{\omega}_{\mathrm{res}}$ is an (N_{d} x N_{d}) diagonal matrix containing the resonance frequencies ω_n.

3.3 Upscaling the microscopic kinematics and stress states

The macroscopic resultants in eqs. (2.21) can be expressed in terms of the microscopic response, computed after application of the Craig-Bampton mode synthesis. Since the unit-cell is subjected to periodic boundary conditions, the surface integral in eq. (2.21) can be simplified since all external forces act on the transverse unit-cell boundaries according to these PBCs. At the 6 prescribed corner nodes, there are non-zero external reaction forces. Besides these external reaction forces, tying tractions exist between opposite boundaries. Each pair of tied nodes at opposing boundaries is therefore subjected to the external forces at the prescribed nodes $\vec{f}_{\mathrm{m,e},i}$ ($i = 1, 2, 4, 5, 6, 8$) and the tying tractions between the opposing nodes to satisfy the periodic boundary conditions. Then for each tying relation between opposing nodes, a zero virtual work condition is defined. After substitution of eqs. (3.6)-(3.7) into the zero virtual work expressions, tractions on the opposing boundaries are related to each other by the following relations as

$$\hat{\vec{t}}^{\mathrm{F}}_{\mathrm{m}} = -\hat{\vec{t}}^{\mathrm{B}}_{\mathrm{m}} = \frac{\hat{\vec{t}}^{\mathrm{B}}_{\mathrm{m},1}}{\frac{1}{2} - \frac{\eta}{H}} = -\frac{\hat{\vec{t}}^{\mathrm{B}}_{\mathrm{m},4}}{\frac{1}{2} - \frac{\eta}{H}} = \frac{\hat{\vec{t}}^{\mathrm{B}}_{\mathrm{m},5}}{\frac{1}{2} + \frac{\eta}{H}} = -\frac{\hat{\vec{t}}^{\mathrm{B}}_{\mathrm{m},8}}{\frac{1}{2} + \frac{\eta}{H}} \tag{3.20a}$$

$$\hat{\vec{t}}^{\mathrm{R}}_{\mathrm{m}} = -\hat{\vec{t}}^{\mathrm{L}}_{\mathrm{m}} = \frac{\hat{\vec{t}}^{\mathrm{L}}_{\mathrm{m},1}}{\frac{1}{2} - \frac{\eta}{H}} = -\frac{\hat{\vec{t}}^{\mathrm{L}}_{\mathrm{m},2}}{\frac{1}{2} - \frac{\eta}{H}} = \frac{\hat{\vec{t}}^{\mathrm{L}}_{\mathrm{m},5}}{\frac{1}{2} + \frac{\eta}{H}} = -\frac{\hat{\vec{t}}^{\mathrm{L}}_{\mathrm{m},6}}{\frac{1}{2} + \frac{\eta}{H}} \tag{3.20b}$$

$$\tilde{\vec{t}}^{\mathrm{F}}_{\mathrm{m}} = -\tilde{\vec{t}}^{\mathrm{B}}_{\mathrm{m}} = -\frac{L_{\mathrm{m}}\tilde{\vec{t}}^{\mathrm{B}}_{\mathrm{m},1}}{2\xi_1} = \frac{L_{\mathrm{m}}\tilde{\vec{t}}^{\mathrm{B}}_{\mathrm{m},4}}{2\xi_1} \tag{3.20c}$$

$$\tilde{\vec{t}}^{\mathrm{R}}_{\mathrm{m}} = -\tilde{\vec{t}}^{\mathrm{L}}_{\mathrm{m}} = -\frac{W_{\mathrm{m}}\tilde{\vec{t}}^{\mathrm{L}}_{\mathrm{m},1}}{2\xi_3} = \frac{W_{\mathrm{m}}\tilde{\vec{t}}^{\mathrm{L}}_{\mathrm{m},2}}{2\xi_3} \tag{3.20d}$$

Recalling the low out-of-plane curvature and inserting eq. (3.20) into eq. (2.21), the surface integral can be omitted and the macroscopic resultants are fully defined in terms of kinematics and stress states of the prescribed nodes. Accordingly, the prescribed displacements (eq. (3.4-3.5) and the reduced dynamic problem (eq. (3.18) are substituted into the macroscopic

resultant expressions, yielding the homogenized constitutive and inertial relations as

$$\hat{\hat{\mathbb{N}}}_{\,\mathrm{M}} = {}^{4}\,\mathbb{C}_{\mathrm{M}}^{\mathrm{mm}} : \hat{\hat{\mathbb{H}}}_{\mathrm{M}}^{\mathrm{C}} + {}^{4}\,\mathbb{D}_{\mathrm{M}}^{\mathrm{ll}} : \ddot{\hat{\hat{\mathbb{H}}}}_{\mathrm{M}}^{\mathrm{C}} + \frac{1}{A_{\mathrm{m,r}}} \sum_{n=1}^{N_{\mathrm{d}}} \mathbf{h}_{n}^{\mathrm{lm}} \ddot{\zeta}_{n} \tag{3.21a}$$

$$\hat{\hat{\mathbb{M}}}_{\,\mathrm{M}} = {}^{4}\,\mathbb{C}_{\mathrm{M}}^{\mathrm{bb}} : \hat{\hat{\mathbb{K}}}_{\mathrm{M}}^{\mathrm{C}} + {}^{4}\,\mathbb{D}_{\mathrm{M}}^{\mathrm{rr}} : \ddot{\hat{\hat{\mathbb{K}}}}_{\mathrm{M}}^{\mathrm{C}} + \frac{1}{A_{\mathrm{m,r}}} \sum_{n=1}^{N_{\mathrm{d}}} \mathbf{h}_{n}^{\mathrm{rt}} \ddot{\zeta}_{n} \tag{3.21b}$$

$$\dot{P}_{\mathrm{m}} = \boldsymbol{\rho}_{\mathrm{M}}^{\mathrm{ll}} \cdot \ddot{\vec{u}}_{\mathrm{M,r}} + \frac{1}{A_{\mathrm{m,r}}} \sum_{n=1}^{N_{\mathrm{d}}} \vec{j}_{n}^{\mathrm{lm}} \ddot{\zeta}_{n} \tag{3.21c}$$

$$\dot{Q}_{\mathrm{m}} = \boldsymbol{\rho}_{\mathrm{M}}^{\mathrm{rr}} \cdot \ddot{\vec{b}}_{\mathrm{M}} + \frac{1}{A_{\mathrm{m,r}}} \sum_{n=1}^{N_{\mathrm{d}}} \vec{j}_{n}^{\mathrm{rt}} \ddot{\zeta}_{n} \tag{3.21d}$$

with the effective material properties defined as

$${}^{4}\mathbb{C}_{\mathrm{M}}^{\mathrm{mm}} = \frac{1}{A_{\mathrm{m,r}}} \left[\underset{\sim}{\hat{\hat{X}}}^{\mathrm{T}}_{\mathrm{m,p}} \underline{\hat{\hat{\mathbb{B}}}}^{\mathrm{qs}}_{\mathrm{m}} \underset{\sim}{\hat{\hat{X}}}_{\mathrm{m,p}} \right]^{\mathrm{LT}} \tag{3.22a}$$

$${}^{4}\mathbb{D}_{\mathrm{M}}^{\mathrm{ll}} = \frac{1}{A_{\mathrm{m,r}}} \left[\underset{\sim}{\hat{\hat{X}}}^{\mathrm{T}}_{\mathrm{m,p}} \underline{\hat{\hat{\mathbb{W}}}}^{\mathrm{qs}}_{\mathrm{m}} \underset{\sim}{\hat{\hat{X}}}_{\mathrm{m,p}} \right]^{\mathrm{LT}} \tag{3.22b}$$

$${}^{4}\mathbb{C}_{\mathrm{M}}^{\mathrm{bb}} = \frac{1}{A_{\mathrm{m,r}}} \left[\left(\underset{\sim}{\eta} \underset{\sim}{\hat{\hat{X}}}_{\mathrm{m,p}} \right)^{\mathrm{T}} \underline{\hat{\hat{\mathbb{B}}}}^{\mathrm{qs}}_{\mathrm{m}} \left(\underset{\sim}{\eta} \underset{\sim}{\hat{\hat{X}}}_{\mathrm{m,p}} \right) \right]^{\mathrm{LT}} \tag{3.22c}$$

$${}^{4}\mathbb{D}_{\mathrm{M}}^{\mathrm{rr}} = \frac{1}{A_{\mathrm{m,r}}} \left[\left(\underset{\sim}{\eta} \underset{\sim}{\hat{\hat{X}}}_{\mathrm{m,p}} \right)^{\mathrm{T}} \underline{\hat{\hat{\mathbb{W}}}}^{\mathrm{qs}}_{\mathrm{m}} \left(\underset{\sim}{\eta} \underset{\sim}{\hat{\hat{X}}}_{\mathrm{m,p}} \right) \right]^{\mathrm{LT}} \tag{3.22d}$$

$$\boldsymbol{\rho}_{\mathrm{M}}^{\mathrm{ll}} = \frac{1}{A_{\mathrm{m,r}}} \underset{\sim}{\mathbb{I}}^{\mathrm{T}}_{\mathrm{m,p}} \cdot \underline{\mathbb{W}}^{\mathrm{qs}}_{\mathrm{m}} \cdot \underset{\sim}{\mathbb{I}}_{\mathrm{m,p}} \tag{3.22e}$$

$$\boldsymbol{\rho}_{\mathrm{M}}^{\mathrm{rr}} = \frac{1}{A_{\mathrm{m,r}}} \left(\underset{\sim}{\eta} \underset{\sim}{\mathbb{I}}_{\mathrm{m,p}} \right)^{\mathrm{T}} \cdot \underline{\mathbb{W}}^{\mathrm{qs}}_{\mathrm{m}} \cdot \left(\underset{\sim}{\eta} \underset{\sim}{\mathbb{I}}_{\mathrm{m,p}} \right) \tag{3.22f}$$

$$\mathbf{h}_{\mathrm{n}}^{\mathrm{lm}} = \left[\underset{\sim}{\hat{\hat{W}}}_{n} \right]^{\mathrm{T}} \underset{\sim}{\hat{\hat{X}}}_{\mathrm{m,p}} \tag{3.22g}$$

$$\mathbf{h}_{\mathrm{n}}^{\mathrm{rt}} = \left[\underset{\sim}{\hat{\hat{W}}}_{n} \right]^{\mathrm{T}} \left[\underset{\sim}{\eta} \underset{\sim}{\hat{\hat{X}}}_{\mathrm{m,p}} \right] \tag{3.22h}$$

$$\vec{j}_{\mathrm{n}}^{\mathrm{lm}} = \underset{\sim}{\mathbb{I}}^{\mathrm{T}}_{\mathrm{m,p}} \cdot \underset{\sim}{\hat{\hat{W}}}_{n} \tag{3.22i}$$

$$\vec{j}_{\mathrm{n}}^{\mathrm{rt}} = \left[\underset{\sim}{\eta} \underset{\sim}{\mathbb{I}}_{\mathrm{m,p}} \right]^{\mathrm{T}} \cdot \underset{\sim}{\hat{\hat{W}}}_{n} \tag{3.22j}$$

Here ${}^{4}\mathbb{C}_{\mathrm{M}}$ is the 4th-order quasi-static effective elasticity tensor, ${}^{4}\mathbb{D}_{\mathrm{M}}$ is the 4th-order quasi-static effective elastic inertia density tensor. $\boldsymbol{\rho}_{\mathrm{M}}$ is the 2nd-order quasi-static effective mass density tensor. $\mathbf{h}_{n}$ is the 2nd-order coupling tensor which the couples emergent degree of freedom corresponding to mode n to the macroscopic stress resultants and $\vec{j}_{n}$ is a coupling vector which couples the emergent degree of freedom corresponding to mode n to the macroscopic kinematic states. The superscripts $(\bullet)^{\mathrm{m}}$ an $(\bullet)^{\mathrm{b}}$ denote membrane and bending deformation, respectively, and $(\bullet)^{\mathrm{lm}}$ and $(\bullet)^{\mathrm{rt}}$ denote linear motion and rotation. The double superscripts $(\bullet)^{\mathrm{mm}}$, $(\bullet)^{\mathrm{ll}}$, $(\bullet)^{\mathrm{bb}}$ and $(\bullet)^{\mathrm{rr}}$ indicate self couplings. The quantities shown in eq. (3.22) are the effective material properties of the unit-cell.

To arrive at the expressions for the homogenized constitutive and inertial relations in eq. (3.21), some higher-order terms are equal to zero or can be neglected. The first-order terms are zero since they are related to the rigid-body linear motion or rigid-body rotation resulting from the prescribed displacements. Second-order terms are related to the coupling of macroscopic resultants and the macroscopic kinematics. These terms can be set to zero if $\vec{X}_{\mathrm{m,r}}$ is set at the inertial center of the unit-cell and the unit-cell is symmetric in the in-plane

and out-of-plane directions. In the validation of the homogenization framework, a symmetric unit-cell is used which means that these terms reduce to zero. The third-order terms reflect the out-of-plane elastic inertia and they can only be neglected if the relaxed separation of scales is satisfied. Due to the relaxed separation of scales, the microscopic variation of the out-of-plane elastic inertia is much smaller than the macroscopic variation in the matrix.

The mode selection criterion introduced in [36] is used to determine the reduced basis composed of N_{d}^{*} localized eigenmodes. Once the mode selection criterion is performed, the prescribed displacements defined in eqs. (3.4-3.5) are substituted into eq. (3.18) which leads to the upscaled microscopic balance of linear momentum, reading

$$\omega_n^2\zeta_n + \ddot{\zeta}_n + \vec{j}_n^{\mathrm{rt}} \cdot \ddot{\vec{b}}_{\mathrm{M}} + \vec{j}_n^{\mathrm{lm}} \cdot \ddot{u}_{\mathrm{M,r}} + \mathbf{h}_n^{\mathrm{lm}} : \ddot{\hat{\mathbb{H}}}_{\mathrm{M}}^{\mathrm{C}} + \mathbf{h}_n^{\mathrm{rt}} : \ddot{\hat{\mathbb{K}}}_{\mathrm{M}}^{\mathrm{C}} = 0,\ n = 1, 2, .., N_{\mathrm{d}}^{*} \tag{3.23}$$

Solving this equation will yield the unknown emergent degrees of freedom ζ_n.

3.4 The homogenization framework in conclusion

In conclusion, the steps to obtain the enriched homogenized continuum shell description is shown once more. A schematic overview is given in Fig. 3.2.

To each macroscopic fibre in the continuum shell, a full through-thickness microscopic unit-cell is appointed. The unit-cell geometry and the microscopic balance of linear momentum are discretised using standard finite element discretisation. The lamina level periodic boundary conditions are employed on the unit-cell. These periodic boundary conditions are defined in terms of the prescribed displacements of 6 corner nodes and the tying relations between opposing boundaries. The top and bottom surface remain traction free. A set of microscopic balance equations in terms of independent nodes is obtained.

The Craig-Bampton mode synthesis is employed on the discretised system. The quasi-static response of the matrix is superposed to a minimised set of eigenmodes representing the internal dynamics. This results in the total dynamic response of the unit-cell. The reduced unit-cell model is used to upscale the microscopic balance of linear momentum.

The macroscopic resultant quantities are expressed in terms of the effective material properties of the unit-cell and the macroscopic displacement field. The macroscopic governing equations are then expressed in terms of the macroscopic resultants. Together with the upscaled microscopic balance of linear momentum, an enriched homogenized description of the macroscopic continuum shell is obtained.

When performing the Craig-Bampton mode synthesis, the eigenvalue problem (eq. (3.16(a)) only has to be solved once and this is mostly done off-line on beforehand. This way, the multi-scale homogenization framework reduces to a single-scale time-dependent framework in which one only has to solve for the macroscopic response. This scale-reduction eventually leads to lower computational costs. When analysing large scale LRAM-structures this advantage will be even higher.

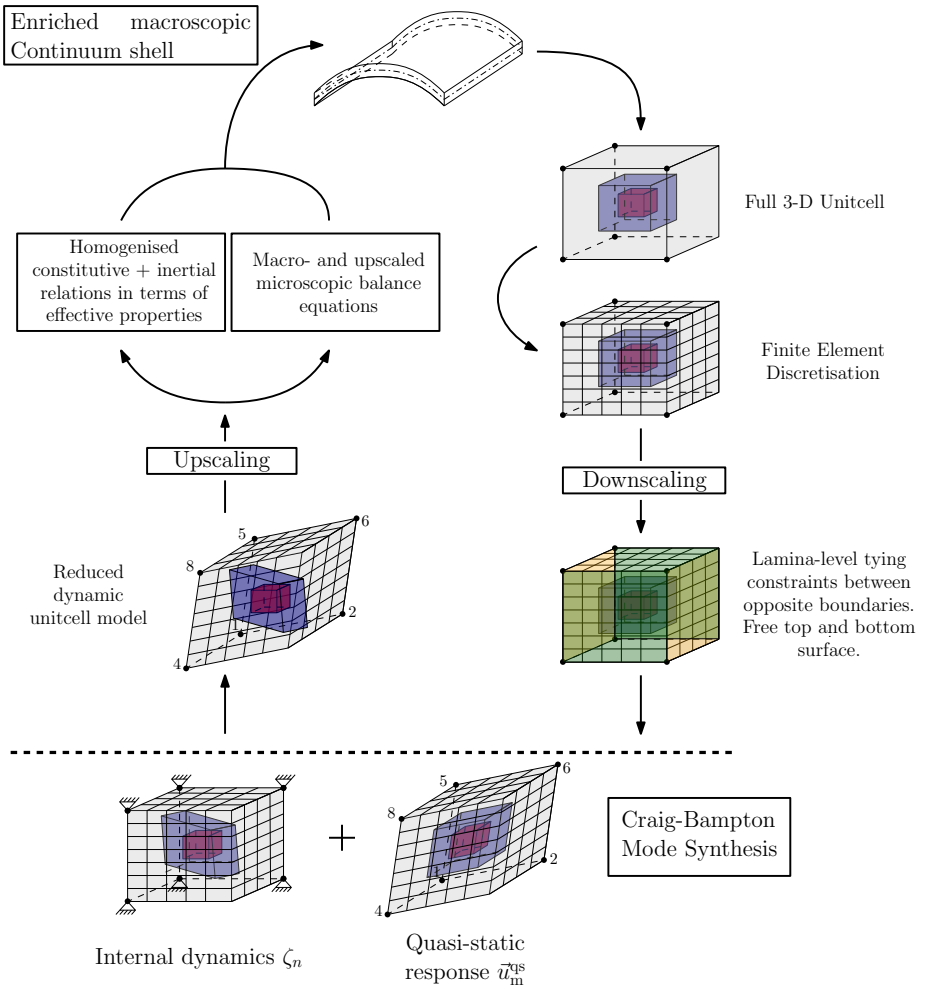

Figure 3.2: *Schematic representation of the enriched continuum shell description-based homogenization framework.*

Chapter 4

Validation on an infinite LRAM plate

To validate the implementation of the homogenization framework, the response of an infinite LRAM plate subjected to certain wave types is analysed. First of all, the macroscopic governing equations are relaxed by decomposing them into the in-plane and out-of-plane components and thereafter crossing out some negligible terms. Accordingly, the plane wave transformation is applied to the relaxed governing equations, resulting in an eigenvalue problem in terms of the effective material properties of the unit-cell, the macroscopic and emergent displacement fields and the wave vector $\vec{k}$. This eigenvalue problem is employed on a symmetric LRAM unit-cell. The homogenizability of the framework is evaluated to determine the frequency range for which the framework is valid. Once this range is determined, the dispersion spectrum computed by the homogenization framework is compared to the ones computed by a reference solution that is yet to be introduced.

4.1 Dispersion analysis

4.1.1 Eigenvalue problem formulation

The macroscopic governing equations in eq. (2.5) are decomposed into the in-plane and out-of-plane components, respectively. By separating these equations, the out-of-plane macroscopic resultants $\hat{\mathbb{N}}_{\mathrm{M}}$ and $\hat{\mathbb{M}}_{\mathrm{M}}$ appear, which were neglected in the macroscopic balance equations due to the assumption of zero out-of-plane shear deformation. Therefore, some assumptions are made, enabling one to find a solution for the desired quantities without taking into account these out-of-plane resultants. This results in the relaxed form of the governing equations and the relaxed upscaled microscopic balance of momentum written as

$$\hat{\vec{\nabla}}_{\mathrm{M}} \cdot \hat{\mathbb{N}}_{\mathrm{M}} - \dot{\hat{\vec{P}}}_{\mathrm{M}} = \vec{0} \tag{4.1a}$$

$$\hat{\vec{\nabla}}_{\mathrm{M}} \hat{\vec{\nabla}}_{\mathrm{M}} : \hat{\mathbb{M}}_{\mathrm{M}} - \tilde{\vec{e}}^{\,\mathrm{c}} \cdot \dot{\hat{\vec{P}}}_{\mathrm{M}} = 0 \tag{4.1b}$$

$$\omega_{\mathrm{n}}^2 \zeta_{\mathrm{n}} + \ddot{\zeta}_{\mathrm{n}} + \vec{j}_{\mathrm{n}}^{\mathrm{lm}} \cdot \ddot{u}_{\mathrm{M,r}} + \mathbf{h}_{\mathrm{n}}^{\mathrm{lm}} : \ddot{\hat{\mathbb{H}}}^{\mathrm{C}}_{\mathrm{M}} + \mathbf{h}_{\mathrm{n}}^{\mathrm{rt}} : \ddot{\hat{\mathbb{K}}}^{\mathrm{C}}_{\mathrm{M}} = 0 \tag{4.1c}$$

for $\mathrm{n} = 1, 2, .., N_{\mathrm{d}}^{*}$. These equations result when applying the following assumptions to eqs. (2.3(b-c)) and eq. (3.23). First of all, in the strong form of the continuum shell description, the zero transverse shear deformation is only implemented in the kinematic relations and relaxed in the balance equations. This means that the out-of-plane balance of momentum resultants ($\hat{\mathbb{N}}_{\mathrm{M}}$ and $\hat{\mathbb{M}}_{\mathrm{M}}$) are neglected. Secondly, by applying the small thickness assumption

to the inertia terms ($\dot{\vec{P}}_{\mathrm{M}}$ and $\dot{\vec{Q}}_{\mathrm{M}}$), the in-plane rotational inertia can be neglected with respect to the out-of-plane linear inertia. Applying these assumptions results in the The macroscopic constitutive and inertial relations defined in eq. (3.21) also have to be relaxed. What is left are the constitutive relations for the macroscopic stress and couple-stress resultants and the inertial relation for macroscopic linear momentum. Due to the relaxation of the governing equations, the inertial relation for the macroscopic rotational inertia is omitted.

4.1.2 Plane wave transformation

For an infinite structure composed of periodic substructures, the displacement field can be split into spatial and time-dependent components. This means that the reference displacement $\vec{u}_{\mathrm{M,r}}$ and the modal displacement amplitude ζ_n in the infinite plate can be written as

$$\begin{bmatrix}\vec{u}_{\mathrm{M}}(\vec{x},t)\\ \zeta_{\mathrm{n}}(\vec{x},t)\end{bmatrix} = \begin{bmatrix}\vec{u}_{\mathrm{M,tr}}\\ \zeta_{\mathrm{n,tr}}\end{bmatrix} e^{i(\vec{k}\cdot\vec{x}-\omega t)} = \underset{\sim}{\mathcal{U}}_{\mathrm{M,tr}} e^{i(\vec{k}\cdot\vec{x}-\omega t)} \tag{4.2}$$

where the subscript $(\bullet)_{\mathrm{tr}}$ denotes the transformed quantity. The wave vector is defined as $\vec{k} = k\vec{e}_{\mathrm{w}}$ with the wave number $k(\lambda)$ and the wave direction $\vec{e}_{\mathrm{w}}$. ω denotes the angular frequency and t the time. The wave vector accounts for the spatial harmonic displacement and the time-dependency is captured in the ωt-component of the exponential term. Applying the plane wave transformation to eq. (4.1) results in the transformed set of equations as

$$i\hat{\vec{k}}\cdot\hat{\mathbb{N}}_{\mathrm{M,tr}} - \dot{\hat{\vec{P}}}_{\mathrm{M,tr}} = \vec{0} \tag{4.3a}$$

$$i\hat{\vec{k}}\cdot i\hat{\vec{k}}\cdot\hat{\mathbb{M}}_{\mathrm{M,tr}} - \tilde{\vec{e}}^{\mathrm{c}}\cdot\dot{\tilde{\vec{P}}}_{\mathrm{M,tr}} = 0 \tag{4.3b}$$

$$\omega_n^2\zeta_{n\mathrm{tr}} - \omega^2\left[\zeta_{n\mathrm{tr}} + \hat{\vec{j}}_n^{\mathrm{lm}}\cdot\hat{\vec{u}}_{\mathrm{M,r,tr}} + \tilde{\vec{j}}_n^{\mathrm{lm}}\cdot\tilde{\vec{u}}_{\mathrm{M,r,tr}} + \mathbf{h}_n^{\mathrm{lm}} : i\hat{\vec{k}}\hat{\vec{u}}_{\mathrm{M,r,tr}} + \mathbf{h}_n^{\mathrm{rt}} : i\hat{\vec{k}}\hat{\vec{b}}_{\mathrm{M,tr}}\right] = 0 \tag{4.3c}$$

for $n = 1, 2, .., N_{\mathrm{d}}^*$. Eq. (4.1) is also applied to the relaxed set of constitutive and inertial relations. These are written as

$$\hat{\mathbb{N}}_{\mathrm{M,tr}} = \left[{}^4\mathbb{C}_{\mathrm{M}}^{\mathrm{mm}} - \omega^2\ {}^4\mathbb{D}_{\mathrm{M}}^{\mathrm{ll}}\right] : i\hat{\vec{k}}\hat{\vec{u}}_{\mathrm{M,r,tr}} - \omega^2\frac{1}{A_{\mathrm{M,r}}}\sum_{n=1}^{N_{\mathrm{d}}*}\mathbf{h}_n^{\mathrm{lm}}\zeta_{n\mathrm{tr}} \tag{4.4a}$$

$$\hat{\mathbb{M}}_{\mathrm{M,tr}} = \left[{}^4\mathbb{C}_{\mathrm{M}}^{\mathrm{bb}} - \omega^2\ {}^4\mathbb{D}_{\mathrm{M}}^{\mathrm{rr}}\right] : i\hat{\vec{k}}\hat{\vec{b}}_{\mathrm{M,tr}} - \omega^2\frac{1}{A_{\mathrm{M,r}}}\sum_{n=1}^{N_{\mathrm{d}}*}\mathbf{h}_n^{\mathrm{rt}}\zeta_{n\mathrm{tr}} \tag{4.4b}$$

$$\dot{\hat{\vec{P}}}_{\mathrm{M,tr}} = -\omega^2\left[\hat{\boldsymbol{\rho}}_{\mathrm{M}}^{\mathrm{ll}}\cdot\hat{\vec{u}}_{\mathrm{M,r,tr}} + \frac{1}{A_{\mathrm{M,r}}}\sum_{n=1}^{N_{\mathrm{d}}*}\hat{\vec{j}}_n^{\mathrm{lm}}\zeta_{n\mathrm{tr}}\right] \tag{4.4c}$$

$$\dot{\tilde{\vec{P}}}_{\mathrm{M,tr}} = -\omega^2\left[\tilde{\boldsymbol{\rho}}_{\mathrm{M}}^{\mathrm{ll}}\cdot\tilde{\vec{u}}_{\mathrm{M,r,tr}} + \frac{1}{A_{\mathrm{M,r}}}\sum_{n=1}^{N_{\mathrm{d}}*}\tilde{\vec{j}}_n^{\mathrm{lm}}\zeta_{n\mathrm{tr}}\right] \tag{4.4d}$$

The angular displacement of the fibre, expressed by $\hat{\vec{b}}_{\mathrm{M}}$ can be eliminated in eq. (4.4) by applying the assumption of zero transverse shear deformation and small deformation. This way, it can be expressed in terms of the membrane displacement and after application of eq. (4.4), it can be expressed as

$$\hat{\vec{b}}_{\mathrm{M,tr}} = -i\hat{\vec{k}}\tilde{\vec{e}}^{\mathrm{c}}\cdot\hat{\vec{u}}_{\mathrm{M,r,tr}} \tag{4.5}$$

Then, substituting eq. (4.5) into eq. (4.3), the $\omega(\vec{k})$-eigenvalue problem is defined in terms of the effective properties, the macroscopic and emergent displacement fields and the wave

vector as

$$\left[\underline{\mathcal{B}}_{\mathrm{M}}^{\omega(\vec{k})}(\vec{k}) - \omega^2 \underline{\mathcal{W}}_{\mathrm{M}}^{\omega(\vec{k})}(\vec{k})\right] \cdot \underline{\mathcal{U}}_{\mathrm{M,tr}}^{\omega(\vec{k})} = \underline{\mathcal{Q}} \tag{4.6}$$

The superscript $(\bullet)^{\omega(\vec{k})}$ indicates that the terms are a function of the wave vector $\vec{k}$. For a given wave vector $\vec{k}$, the system can be solved for the frequencies ω, the corresponding displacement field of the reference lamina $\vec{u}_{\mathrm{M,r,tr}}$ and the modal displacement amplitudes $\zeta_{n\mathrm{tr}}$ for $n = 1, 2, .., N_{\mathrm{d}}^*$. The dynamic stiffness and mass matrices and the dynamic displacement vector column for the $\omega(\vec{k})$-form eigenvalue problem defined as

$$\underline{\mathcal{B}}_{\mathrm{M}}^{\omega(\vec{k})}(\vec{k}) = \begin{bmatrix} k^2 \hat{\vec{e}}_w \cdot^4 \mathbb{C}_{\mathrm{M}}^{\mathrm{mm}} \cdot \hat{\vec{e}}_w & \underline{0} & \underline{0}^{\mathrm{T}} \\ \underline{0}^{\mathrm{T}} & k^4 \hat{\boldsymbol{e}}_w :^4 \mathbb{C}_{\mathrm{M}}^{\mathrm{bb}} : \hat{\boldsymbol{e}}_w \tilde{\vec{e}}^{\mathrm{c}} & \underline{0}^{\mathrm{T}} \\ \underline{0} & \underline{0} & \underline{\omega}_{\mathrm{res}}^2 \end{bmatrix} \tag{4.7a}$$

$$\underline{\mathcal{W}}_{\mathrm{M}}^{\omega(\vec{k})}(\vec{k}) = \begin{bmatrix} \hat{\boldsymbol{\rho}}_{\mathrm{M}}^{\mathrm{ll}} + k^2 \hat{\vec{e}}_w \cdot^4 \mathbb{D}_{\mathrm{M}}^{\mathrm{ll}} \cdot \hat{\vec{e}}_w & \underline{0} & \frac{1}{A_{\mathrm{m,r}}} \left[(\hat{\underline{j}}^{\mathrm{lm}})^{\mathrm{T}} - ik \hat{\vec{e}}_w \cdot (\underline{\mathbf{h}}^{\mathrm{lm}})^{\mathrm{T}} \right] \\ \underline{0}^{\mathrm{T}} & k^4 \hat{\boldsymbol{e}}_w :^4 \mathbb{D}_{\mathrm{M}}^{\mathrm{rr}} : \hat{\boldsymbol{e}}_w \tilde{\vec{e}}^{\mathrm{c}} & \frac{1}{A_{\mathrm{m,r}}} \left[\tilde{\vec{e}}^{\mathrm{c}} \cdot (\tilde{\underline{j}}^{\mathrm{lm}})^{\mathrm{T}} + k^2 \hat{\boldsymbol{e}}_w : (\underline{\mathbf{h}}^{\mathrm{rt}})^{\mathrm{T}} \right] \\ \hat{\underline{j}}^{\mathrm{lm}} + ik \underline{\mathbf{h}}^{\mathrm{lm}} \cdot \hat{\vec{e}}_w & \tilde{\underline{j}}^{\mathrm{lm}} + k^2 \underline{\mathbf{h}}^{\mathrm{rt}} : \hat{\boldsymbol{e}}_w \tilde{\vec{e}}^{\mathrm{c}} & \underline{\mathrm{I}} \end{bmatrix} \tag{4.7b}$$

$$\underline{\mathcal{U}}_{\mathrm{M,tr}}^{\omega(\vec{k})}(\vec{k}) = \begin{bmatrix} \hat{\vec{u}}_{\mathrm{M,r,tr}} \\ \tilde{\vec{u}}_{\mathrm{M,r,tr}} \\ \zeta_{\mathrm{n,tr}} \end{bmatrix} \tag{4.7c}$$

with the tensor $\hat{\boldsymbol{e}}_w$ defined by the dyadic product $\hat{\vec{e}}_w \tilde{\vec{e}}_w$ and $\underline{\mathrm{I}}$ the unit-matrix of dimensions (N_{d}^* x N_{d}^*). Thus, by solving the $\omega(\vec{k})$-form eigenvalue problem, the frequency response ω the reference lamina displacement $\vec{u}_{\mathrm{M,tr}}$ and the modal displacement amplitudes $\zeta_{\mathrm{n,tr}}$ are computed.

4.1.3 Mode selection criterion

To determine the minimum number of modes N_{d}^*, a mode selection criterion was defined in [29] which is an extended criterion introduced and validated in [36]. The extended criterion states that the minimum number of modes should be such that the sum of the modal mass fractions and the modal elastic inertia fractions over this minimum number of modes should be equal to the mass fraction and elastic inertia fraction of the inclusion itself. This is them written as

$$\mu_{\mathrm{inc}}^{\rho,\mathrm{ll}} = \frac{1}{\boldsymbol{\rho}_{\mathrm{M}}^{\mathrm{ll}}} \sum_{n=1}^{N_{\mathrm{d}}^*} \frac{\vec{j}_n^{\mathrm{lm}} \vec{j}_n^{\mathrm{lm}}}{A_{\mathrm{m,r}}} \tag{4.8a}$$

$$\mu_{\mathrm{inc}}^{D,\mathrm{rr}} = \frac{1}{{}^4\mathbb{D}_{\mathrm{M}}^{\mathrm{ll}}} \sum_{n=1}^{N_{\mathrm{d}}^*} \frac{\mathbf{h}_n^{\mathrm{rt}} \mathbf{h}_n^{\mathrm{rt}}}{A_{\mathrm{m,r}}} \tag{4.8b}$$

Regarding the modal mass fraction, only the linear motion related terms ($^{\mathrm{ll}}$ and $^{\mathrm{lm}}$) are taken into account and rotation related terms are neglected. For the elastic inertia related terms however, only the rotation related terms ($^{\mathrm{rr}}$ and $^{\mathrm{rt}}$) are take into account and the linear motion related terms are neglected. The rotational mass inertia is negligible due to the small thickness assumption of the macroscopic shell. The linear elastic inertia fraction of the inclusion is negligible since the membrane stiffness of the matrix is much higher than the one of the heterogeneities. Thus, the minimum number of eigenmodes (reduced basis)

is determined by the set of eigenmodes approximately satisfying eq. (4.8), starting from the lowest eigenfrequency. In practice, the minimum set of eigenmodes will not exactly represent the total inclusion mass fraction or elastic inertia fraction and in [36] a tolerance of $\approx 5\%$ is adopted. However, it is not stated that this tolerance is applicable to any unit-cell design. In the subsequent analysis, the modal mass and elastic inertia fractions will be determined and the deviation with respect to the inclusion mass and elastic inertia fraction is determined.

4.1.4 Limit of homogenization

The frequency limit up to which the homogenization framework is valid can be determined by evaluating the separation of scales introduced in eq. (2.13). The wavelength interfering with the host matrix should be much larger than the smallest representative length-scale of the matrix. In [37] it is suggested to take into account a wavelength which is at least 10 times longer than the smallest representative size l in the unit-cell which leads to an expression for a limitation of the wave number as $k_{\text{lim}} = \pi/5l$. When the wavelength exceeds this limit, neighbouring unit-cells might interfere with each other due to non-local interactions. To this extent, the eigenvalue problem in eq. (4.6) must be solved for the wave number k_{lim} along a wave direction $\vec{e}_{\text{w}}$. Then within the frequency limit, the error in the phase velocity for any flexural or body wave within that range must be smaller than a certain threshold. The error is determined by the difference between the homogenization-based phase velocity and the phase velocity computed by the reference solution.

4.2 The infinite LRAM plate analysis

To validate the homogenization framework on an infinite LRAM plate, the $\omega(\vec{k})$-form eigenvalue problem is solved and compared to a reference solution. The reference solution used in the dispersion analysis is the traditional Bloch Analysis [38, 39]. First of all, the implemented unit-cell design with corresponding material properties is discussed. Consequently, the dispersion spectra obtained from the homogenization framework is compared to the one obtained from Bloch Analysis.

4.2.1 Unit-cell configuration

For the analysis of the infinite LRAM plate, a negative-mass design is employed. In Fig. 4.1 the unit-cell with the in-plane geometry and the discretized unit-cell are shown, respectively. Part of the unit-cell is hidden in Fig. 4.1(a) for visualization purposes only. The unit-cell consists of three constituents, namely the host matrix material, the coating and the cylindrical core, coloured grey, blue and red, respectively, in Fig. 4.1. In the remainder of this thesis, the coating and the core together are referred to as the *inclusion*. The material properties for each constituent are given in Tab. 4.1.

In Section 1 it was stated that the negative-mass design consists of a host material (matrix) which is connected to a resonator (core) through a linear spring (coating). The area of interest for the implementation of the homogenization framework is low-frequency vibration attenuation in lightweight materials. To this extent, the matrix material must be chosen stiff and lightweight and these properties can be attributed to glass. The coating material should have a low stiffness such that it shows the properties of a soft material, hence rubber is chosen. The core should have a resonance frequency in the low-frequency range and therefore the mass density must be high compared to that of the matrix. Therefore, tungsten is chosen as core material. The properties responsible for inducing a local resonance within the current unit-cell configuration are the low Young's modulus of the rubber coating and

Constituent	**Young's modulus** E		**Poisson's ratio** ν		**Mass density** ρ	
	Value	*Unit*	*Value*	*Unit*	*Value*	*Unit*
Matrix [40]	107	[GPa]	0.276	[-]	2050	$[\mathrm{kg}\cdot\mathrm{m}^{-3}]$
Coating [41]	35	[kPa]	0.469	[-]	1300	$[\mathrm{kg}\cdot\mathrm{m}^{-3}]$
Core [42]	411	[GPa]	0.280	[-]	19200	$[\mathrm{kg}\cdot\mathrm{m}^{-3}]$

Table 4.1: *Material properties of the unit-cell constituents*

the high mass density of the core with respect to the corresponding properties of the other constituents. This combination of materials has proven to open up band gaps in the low-frequency regime for symmetric LRAM unit-cells in [42] and for the infinite LRAM beam in [29]. In the upcoming analysis it will be determined if this material combination also provides the desired low-frequency band-gaps for this unit-cell design.

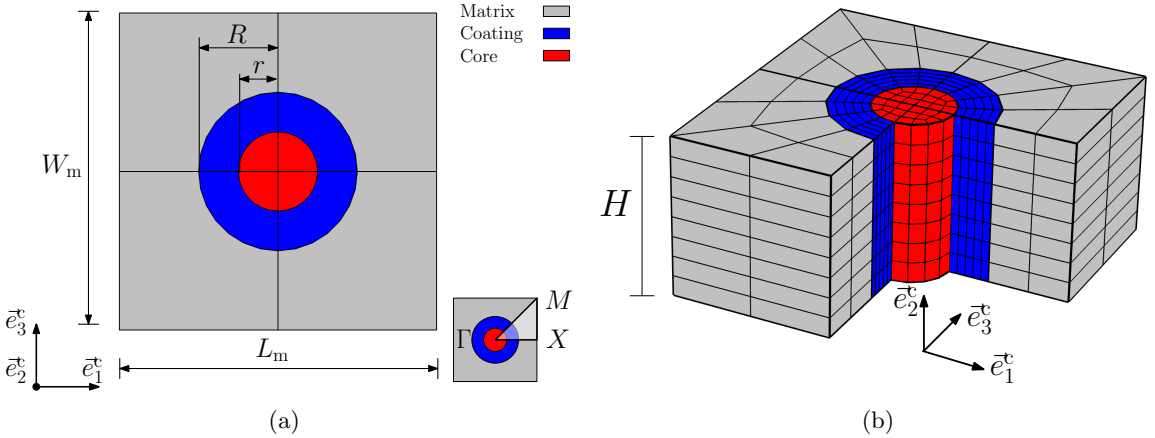

Figure 4.1: *Top-view of the unit-cell geometry with its in-plane dimensions (a) and the first (irreducible) Brillouin zone. The unit-cell is discretized using standard FE-discretization (b).*

Symbol	**Value**	**Unit**	**Property**
L_m	0.01	[m]	Unit-cell length
W_m	0.01	[m]	Unit-cell width
H	0.005	[m]	Unit-cell height / Shell thickness
R	$0.25\cdot L_\mathrm{m}$	[m]	Coating outer radius
r	$0.5\cdot R$	[m]	Core radius

Table 4.2: *Unit-cell dimensions*

The dimensions of the unit-cell and its constituents are shown in Tab. 4.2. The coating and core are of equal height as the unit-cell. Note that when using this unit-cell configuration for LRAM plate analysis, a load at the top or bottom surface of the plate will influence the local resonance effects drastically. This is due to the fact that the load is then applied at the resonator (core) directly which means that Craig-Bampton mode synthesis is not valid. If one wants to apply a load on either the top or bottom surface, a different unit-cell configuration must be chosen, e.g. a square or spherical inclusion fully surrounded by the coating and matrix. However, for the current implementation this configuration is a

valid choice. When using the CBMS for computing the dynamic response it is also important that the matrix boundaries are not deformed by the local resonance, i.e. the local resonance is contained within the unit-cell boundaries. This means that the material should be chosen sufficiently stiff, and the distance between the inclusion and the matrix boundary should be sufficiently large. These requirements on the matrix will make sure that the local resonance is contained inside the unit-cell.

The unit-cell is discretized using 3-dimensional 8-node linear hexahedral elements as can be seen in Fig. 4.1b. Since the matrix material is chosen to be sufficiently stiff, the deformations in the matrix in the low-frequency regime will not be that large. In the coating however, the deformation can become larger because of the low Young's modulus compared to the other two constituents, especially when the localized eigenmode is activated. Hence, the element size in the matrix is chosen relatively large compared to the element size in the coating. Another reason for the relatively large element size in the matrix, is the fact that the same unit-cell configuration is used in the finite panel analysis. Keeping the number of elements in the unit-cell low, will enable one to use the same mesh in the finite panel configuration. In fact, this is further explained in Chap. 5. Finally, the elements in the current mesh are within a range of $0.5 - 2.5$ mm and the total number of degrees of freedom is equal to 4131.

4.2.2 Effective properties

Prior to the actual dispersion analysis, the effective properties (eq. 3.22)) are calculated for the employed unit-cell configuration. The effective properties of the unit-cell and its corresponding eigenmodes are displayed in Tab. 4.3 and 4.4.

Matrix unit-cell					
Property	**Orientation**				**Unit**
	$\vec{e}_{11}{}^{c}$	$\vec{e}_{22}{}^{c}$	$\vec{e}_{33}{}^{c}$		
$\boldsymbol{\rho}_{\mathrm{M}}$	8.29	8.29	8.29		$[\mathrm{kg}\cdot\mathrm{m}^{-2}]$
	$\vec{e}_{1111}{}^{c},\ \vec{e}_{3333}{}^{c}$	$\vec{e}_{1133}{}^{c},\ \vec{e}_{3311}{}^{c}$	$\vec{e}_{1331}{}^{c},\ \vec{e}_{3113}{}^{c}$	$\vec{e}_{1313}{}^{c},\ \vec{e}_{3131}{}^{c}$	
${}^{4}\mathbb{C}_{\mathrm{M}}^{\mathrm{mm}}$	$371.37\cdot10^{6}$	$89.93\cdot10^{6}$	$116.35\cdot10^{6}$	$116.35\cdot10^{6}$	$[\mathrm{kg}\cdot\mathrm{m}^{-2}\cdot\mathrm{s}^{2}]$
${}^{4}\mathbb{C}_{\mathrm{M}}^{\mathrm{bb}}$	816.30	179.25	414.10	1523.30	$[\mathrm{kg}\cdot\mathrm{s}^{2}]$
${}^{4}\mathbb{D}_{\mathrm{M}}^{\mathrm{ll}}$	$1.10\cdot10^{-4}$	$0.11\cdot10^{-4}$	$0.32\cdot10^{-4}$	$1.14\cdot10^{-4}$	$[\mathrm{kg}]$
${}^{4}\mathbb{D}_{\mathrm{M}}^{\mathrm{rr}}$	$0.93\cdot10^{-9}$	$0.56\cdot10^{-9}$	$7.30\cdot10^{-12}$	$1.03\cdot10^{-10}$	$[\mathrm{kg}\cdot\mathrm{m}^{2}]$
LRAM unit-cell					
	$\vec{e}_{11}{}^{c}$	$\vec{e}_{22}{}^{c}$	$\vec{e}_{33}{}^{c}$		
$\boldsymbol{\rho}_{\mathrm{M}}$	13.82	13.82	13.82		$[\mathrm{kg}\cdot\mathrm{m}^{-2}]$
	$\vec{e}_{1111}{}^{c},\ \vec{e}_{3333}{}^{c}$	$\vec{e}_{1133}{}^{c},\ \vec{e}_{3311}{}^{c}$	$\vec{e}_{1331}{}^{c},\ \vec{e}_{3113}{}^{c}$	$\vec{e}_{1313}{}^{c},\ \vec{e}_{3131}{}^{c}$	
${}^{4}\mathbb{C}_{\mathrm{M}}^{\mathrm{mm}}$	$371.37\cdot10^{6}$	$89.93\cdot10^{6}$	$116.35\cdot10^{6}$	$116.35\cdot10^{6}$	$[\mathrm{kg}\cdot\mathrm{m}^{-2}\cdot\mathrm{s}^{2}]$
${}^{4}\mathbb{C}_{\mathrm{M}}^{\mathrm{bb}}$	816.30	179.25	414.10	1523.30	$[\mathrm{kg}\cdot\mathrm{s}^{2}]$
${}^{4}\mathbb{D}_{\mathrm{M}}^{\mathrm{ll}}$	$1.18\cdot10^{-4}$	$0.14\cdot10^{-4}$	$0.35\cdot10^{-4}$	$1.21\cdot10^{-4}$	$[\mathrm{kg}]$
${}^{4}\mathbb{D}_{\mathrm{M}}^{\mathrm{rr}}$	$2.09\cdot10^{-9}$	$1.72\cdot10^{-9}$	$7.90\cdot10^{-12}$	$1.04\cdot10^{-10}$	$[\mathrm{kg}\cdot\mathrm{m}^{2}]$

Table 4.3: *Effective unit-cell properties of a unit-cell without inclusion and those of the LRAM unit-cell from Fig. 4.1.*

Not only are the effective properties used to minimize the reduced eigenmode basis, but evaluating these effective properties will already lead to some insights regarding the microscopic behaviour of each eigenmode. The frequency range of interest is defined from

0 up to 1500 Hz and from an initial eigenmode analysis of the unit-cell, 19 eigenmodes are captured within this range. Inserting the effective properties of the LRAM unit-cell into the selection criterion shows that eq. (4.8) is approximately satisfied if the minimum number of eigenmodes is equal to $N_{\mathrm{d}}^{*} = 13$. In order to compute the inclusion mass fraction and the inclusion elastic inertia fraction, the effective properties of the unit-cell without inclusion (*Matrix unit-cell*) are also computed.

The subscripts $(\bullet)_{iiii},\ i = 1,3$ indicate the dyadic product of the corotational basis vectors $\vec{e}_1{}^{c}$ and $\vec{e}_3{}^{c}$. Evaluating the effective properties for the LRAM unit-cell and the Matrix unit-cell, it can be seen that the addition of the inclusion has an impact on the effective mass density $\boldsymbol{\rho}_{\mathrm{M}}$ and the rotational elastic inertia density ${}^{4}\mathbb{D}_{\mathrm{M}}^{\mathrm{rr}}$. It has hardly any influence on the other effective properties, which is also expected from the current unit-cell design. Due to the soft rubber coating, the effective membrane and bending stiffness are dominated by the matrix material, hence no significant change of ${}^{4}\mathbb{C}_{\mathrm{M}}^{\mathrm{mm}}$ and ${}^{4}\mathbb{C}_{\mathrm{M}}^{\mathrm{bb}}$ is observed. Also the linear elastic inertia density is dominated by the unit-cell matrix.

An important remark must be made on the 1313-component of the bending stiffness. Comparing this entry to the other components, it can be seen that this one is the largest. This component relates the macroscopic twisting moment working on the unit-cell to the twisting curvature of the unit-cell. Due to the choice of the current unit-cell geometry, the effective bending stiffness is anisotropic. Whether this anisotropy of the bending stiffness is of influence on the frequency response of the LRAM unit-cell is investigated in dispersion analysis in the next section.

The effective properties corresponding to the active eigenmodes are shown in Tab. 4.4. From the mode selection criterion it was determined that the reduced basis is composed of the 13 eigenmodes with the lowest eigenfrequencies. Also the sum over the modal mass fractions and modal elastic inertia fractions are shown to prove that the mode selection criterion is satisfied within certain accuracy. The coupling terms $\vec{j}_n^{\mathrm{rt}}$ and $\boldsymbol{h}_n^{\mathrm{lm}}$ are not displayed as they are negligible with respect to the other coupling terms. The coupling term $\vec{j}_n^{\mathrm{rt}}$ couples the modal mass inertia to the macroscopic rotational momentum, but due to the small thickness of the continuum shell, this term is negligible. The coupling term $\boldsymbol{h}_n^{\mathrm{lm}}$ couples the modal linear elastic inertia to the macroscopic in-plane stress resultant. Since the membrane stiffness of the unit-cell is much higher than its linear elastic inertia, this term is also negligible.

The effective properties in Tab. 4.4 need some more attention. First of all, there are several modes for which both coupling terms $\vec{j}_n^{\mathrm{lm}}$ and $\boldsymbol{h}_n^{\mathrm{rt}}$ are zero. These eigenmodes reflect in-plane or out-of-plane rotational motion of the core or the coating. These modes and they do not contribute significantly to the dynamic response of the LRAM unit-cell subjected to flexural or body waves. Also, it can be seen that each non-zero $\vec{\vec{j}}_n^{\mathrm{lm}}$ is accompanied by a non-zero $\boldsymbol{h}_n^{\mathrm{rt}}$. These terms correspond to the macroscopic out-of-plane linear momentum and macroscopic in-plane couple-stress resultant, respectively. The latter one is able to induce negative effective bending stiffness although its influence is small compared to the effective bending stiffness of the unit-cell ${}^{4}\mathbb{C}_{\mathrm{M}}$ for the current unit-cell design. The coupling term $\vec{j}_n^{\mathrm{lm}}$ however, relates to the effective mass density of the unit-cell. This means that a large non-zero $\vec{j}_n^{\mathrm{lm}}$ is able to open up the attenuating negative mass-induced frequency band-gaps. This will be verified in the upcoming dispersion analysis.

At the bottom of Tab. 4.4, the summations over the modal mass and elastic inertia fractions are computed together with the inclusion mass and elastic inertia fractions. First of all, it can be seen that there is a slight difference regarding the modal mass fraction and the inclusion mass fraction. The sum over the modal mass fractions is smaller than the inclusion mass fraction and this means that the mass effects captured by the reduced unit-cell description will not exactly represent the total mass effects of the inclusion. Yet,

the maximum difference is approximately 5%. Considering the linear modal elastic inertia fractions, the resemblance with respect to the inclusion elastic inertia is good. Yet, as discussed previously, the contribution of the inclusion elastic inertia to the full unit-cell response is small with respect to the contribution of the inclusion mass inertia.

Property	**Eigenmode n**				**Unit**
	1	2,3	4	5	
f_{n}	168.3	322.8	352.1	366.0	[Hz]
$\vec{j}_n^{\mathrm{lm}}$	$0.023\vec{e}_2{}^{\mathrm{c}}$	$\approx \vec{0}$	$\approx \vec{0}$	$-0.011\vec{e}_1{}^{\mathrm{c}} - 0.020\vec{e}_3{}^{\mathrm{c}}$	$[\mathrm{kg}^{\frac{1}{2}}]$
$\boldsymbol{h}_n^{\mathrm{rt}}$	$0.330 \cdot 10^{-6}$ $(\vec{e}_1{}^{\mathrm{c}}\vec{e}_1{}^{\mathrm{c}} + \vec{e}_3{}^{\mathrm{c}}\vec{e}_3{}^{\mathrm{c}})$	$\approx \mathbb{O}$	$\approx \mathbb{O}$	$\approx \mathbb{O}$	$[\mathrm{kg}^{\frac{1}{2}} \cdot \mathrm{m}^2]$
	6	7	8,9	10	
f_{n}	366.0	1263.3	1277.7	1350.4	[Hz]
$\vec{j}_n^{\mathrm{lm}}$	$-0.020\vec{e}_1{}^{\mathrm{c}} - -0.012\vec{e}_3{}^{\mathrm{c}}$	$-0.005\vec{e}_2{}^{\mathrm{c}}$	$\approx \vec{0}$	$\approx \vec{0}$	$[\mathrm{kg}^{\frac{1}{2}}]$
$\boldsymbol{h}_n^{\mathrm{rt}}$	$\approx \mathbb{O}$	$-0.068 \cdot 10^{-6}$ $(\vec{e}_1{}^{\mathrm{c}}\vec{e}_1{}^{\mathrm{c}} + \vec{e}_3{}^{\mathrm{c}}\vec{e}_3{}^{\mathrm{c}})$	$\approx \mathbb{O}$	$\approx \mathbb{O}$	$[\mathrm{kg}^{\frac{1}{2}} \cdot \mathrm{m}^2]$
	11	12	13		
f_{n}	1350.5	1410.8	1410.8		[Hz]
$\vec{j}_n^{\mathrm{lm}}$	$\approx \vec{0}$	$0.001\vec{e}_1{}^{\mathrm{c}} - 0.002\vec{e}_3{}^{\mathrm{c}}$	$-0.002\vec{e}_1{}^{\mathrm{c}} - 0.001\vec{e}_3{}^{\mathrm{c}}$		$[\mathrm{kg}^{\frac{1}{2}}]$
$\boldsymbol{h}_n^{\mathrm{rt}}$	$\approx \mathbb{O}$ $(\vec{e}_1{}^{\mathrm{c}}\vec{e}_1{}^{\mathrm{c}} + \vec{e}_3{}^{\mathrm{c}}\vec{e}_3{}^{\mathrm{c}})$	$\approx \mathbb{O}$	$\approx \mathbb{O}$	$\approx \mathbb{O}$	$[\mathrm{kg}^{\frac{1}{2}} \cdot \mathrm{m}^2]$

Fraction	**Orientation**			**Unit**
	$\vec{e}_1{}^{\mathrm{c}}\vec{e}_1{}^{\mathrm{c}}$	$\vec{e}_2{}^{\mathrm{c}}\vec{e}_2{}^{\mathrm{c}}$	$\vec{e}_3{}^{\mathrm{c}}\vec{e}_3{}^{\mathrm{c}}$	
$\mu_{\mathrm{inc}}^{\rho}$	40.1	40.1	40.1	%
$\sum_{n=1}^{\mathrm{N_d^*}} \mu_n^{\rho}$	38.1	38.8	37.9	%
	$\vec{e}_1{}^{\mathrm{c}}\vec{e}_1{}^{\mathrm{c}}\vec{e}_1{}^{\mathrm{c}}\vec{e}_1{}^{\mathrm{c}}$	$\vec{e}_1{}^{\mathrm{c}}\vec{e}_1{}^{\mathrm{c}}\vec{e}_3{}^{\mathrm{c}}\vec{e}_3{}^{\mathrm{c}}$		
$\mu_{\mathrm{inc}}^{\mathrm{D}}$	55.8	67.6		%
$\sum_{n=1}^{\mathrm{N_d^*}} \mu_n^{\mathrm{D}}$	54.3	58.2		%

Table 4.4: *Effective properties corresponding to the reduced eigenmode basis for the unit-cell from Fig. 4.1*

4.2.3 Dispersion analysis

Now that the effective properties of the LRAM unit-cell and the reduced basis are known, the $\omega(\vec{k})$-form eigenvalue problem defined in eq. (4.6) can be solved for given values of $\vec{k}$. Due to the periodicity of the infinite plate, the wave vector $\vec{k}$ is restricted to the first Brillouin zone defined in Fig. 4.1a. Since the wave can only propagate along the in-plane directions, the wave vector is restricted to the domain $\vec{k} = [k\vec{e}_1^{\mathrm{t}}, k\vec{e}_3^{\mathrm{t}}] \in [-\frac{2\pi}{\lambda_{\mathrm{ref}}}, \frac{2\pi}{\lambda_{\mathrm{ref}}}]$. Here, $\lambda_{\mathrm{ref}} = 6.3H$ which is derived from the predicted deviation on the flexural wave phase velocity of 10%. This predicted deviation is taken into account when neglecting the out-of-plane shear effects for thin shells. Moreover, due to the square in-plane periodicity of the unit-cell, the wave vector can be restricted to the first irreducible Brillouin zone (FIBZ) which is denoted by the translucent triangle in Fig. 4.1a. Hence, the wave-direction to be analysed is defined

along the boundary of the FIBZ.

The solution of the homogenization-based dispersion analysis is compared to the standard solution defined by the Bloch Analysis. The Bloch-Floquet theorem is adopted as a reference solution for the dispersion analysis of the infinite LRAM plate. This is a valid approach since this theorem is applicable to infinite media composed of periodic structures (unit-cells). Each point in an infinite medium can be represented as the corresponding point in a reference unit-cell together with a phase shift. This phase shift is related to the distance between the reference unit-cell and the point in the infinite medium. The Bloch-Floquet boundary conditions must be rewritten to apply them to the continuum shell. A more comprehensive description can be found in App. A. Eventually, the modified Bloch-Floquet boundary conditions can be implemented according to FEM.

The resulting dispersion spectra computed by the homogenization method and the reference solution are shown in Fig. 4.2(d-I) together with the dynamic effective mass density of the LRAM unit-cell in Fig. 4.2(d-II) [1]. The negative mass-induced frequency band-gaps are marked by the green and purple areas. From the figure, it can be seen that the first green-marked flexural wave band-gap is related to the negative out-of-plane effective mass density. This indicates that the out-of-plane linear motion of the infinite LRAM-plate is cancelled, leading to the attenuation of the flexural wave. This can be attributed to activation of eigenmode 1; the core and host are moving in opposite out-of-plane phase as can be seen in Fig. 4.2(a). A second flexural wave band-gap is marked by the upper green area. This band-gap is attributed to the coating and the host moving in opposite phase, again cancelling the out-of-plane motion of the infinite LRAM plate. This active eigenmode is illustrated in Fig. 4.2(e).

The purple-marked frequency band-gaps are related to the in-plane negative effective mass density. An in-plane negative effective mass density indicates that the in-plane linear motion of the infinite plate is cancelled, actively attenuating compression waves. The first purple band-gap is related to the opposite in-plane motion of the core with respect to the matrix, whereas the second purple band-gap is related to the opposite in-plane motion of the coating with respect to the matrix. Both phenomena are illustrated in Fig. 4.2(b-c) and 4.2(f-g), respectively. The remaining eigenmodes are not displayed, as they do not contribute to the attenuation of waves propagating through the unit-cell. This is also what was expected from the coupling terms in Tab. 4.4. Only modes that show linear in-plane or out-of-plane motion of either the core or the coating contain non-zero coupling terms and contribute to the attenuation of flexural or body waves.

Comparing the real dispersion spectra of the homogenization method to the reference solution, two ranges are distinguished. The first range is the wave-vector $\vec{k} \in \Gamma - M$ and $\vec{k} \in M - X$. The branches within this range are related to a wave propagating in the $\vec{e}_1^{\mathfrak{t}}$ or $\vec{e}_3^{\mathfrak{t}}$ direction. The branches corresponding to either flexural or compression waves within show a very good match with the reference solution. The deviation on the phase velocity is at is at most 1.58% for the compressive waves and 1.21% for the flexural waves. When the wave number approaches Γ in the FIBZ, the frequency changes very rapidly with decreasing wave number. This large gradient of the frequency leads to a deviation between the homogenization method and the Bloch analysis. Yet, the homogenization method can capture the unit-cell response with great accuracy in this wave number range.

[1] The dynamic effective mass density is a superposition of the effective mass density of the unit-cell $\boldsymbol{\rho}_{\mathrm{M}}$ and the summation of the modal mass fractions. For a detailed description of the dynamic effective density one is referred to [29]

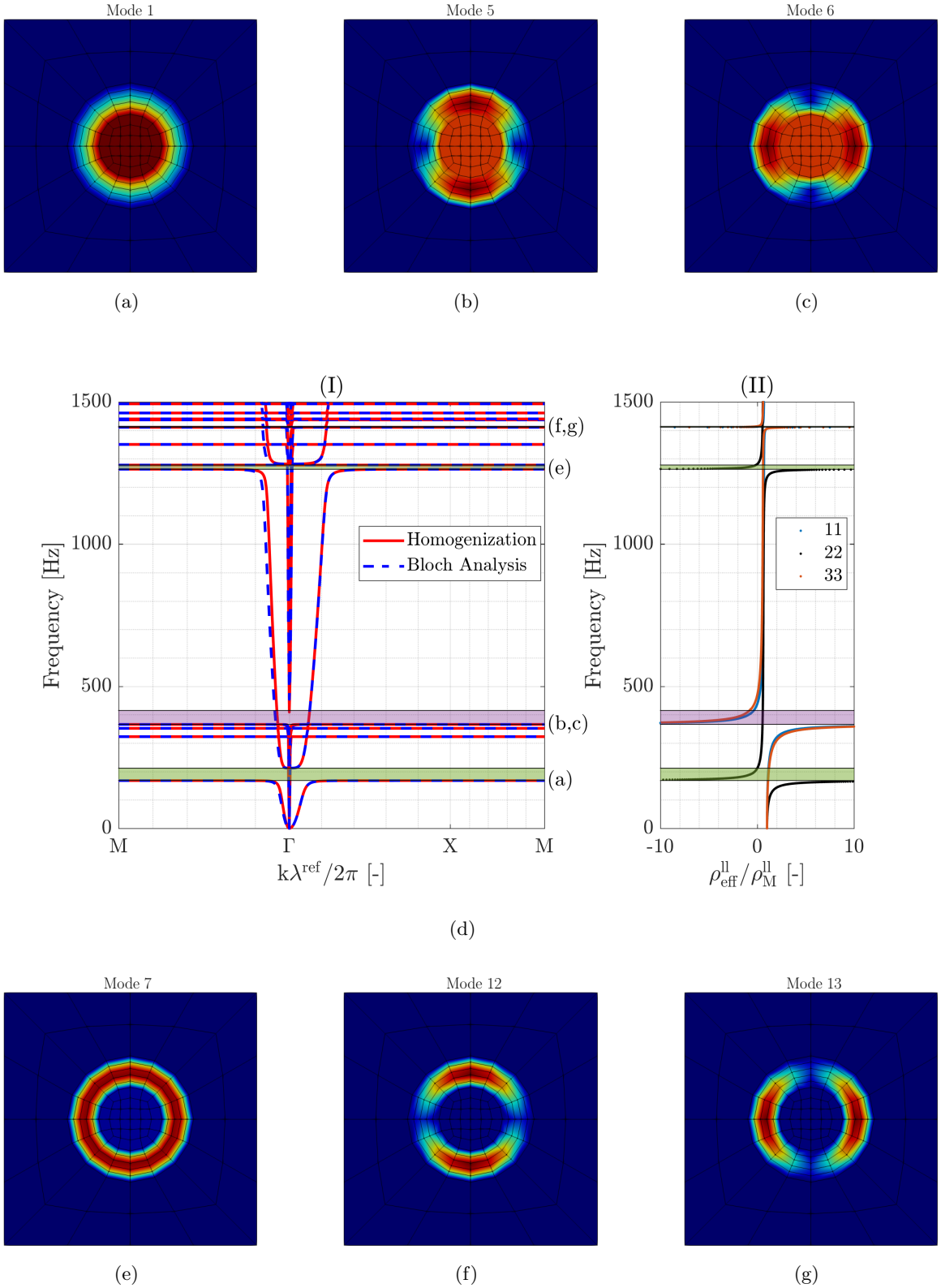

Figure 4.2: *The real dispersion spectra computed by the homogenization method and the Bloch analysis for the infinite LRAM plate (d-I) and the dynamic effective mass density (d-II). The active eigenmodes are shown in (a-c) and (e-g).*

The second range to be discussed, is the wave-vector $\vec{k} \in X - \Gamma$. The compression wave

branches, shows good comparison for the homogenization method compared to the reference solution. However, the flexural wave branches show deviations up to 35% with respect to the reference solution. Looking back at the effective unit-cell properties in Tab. 4.3, one should take a second look at ${}^4\mathbb{C}^{\text{bb}}_{\text{M},1313}$. Since the wave vector along the $X-\Gamma$-path coincides with the 13-direction of the unit-cell, this high torsion-related stiffness due to the anisotropic unit-cell has a major influence on the frequency response of the unit-cell for a wave propagating in that direction. Therefore, the frequency response of the infinite LRAM-plate to a flexural wave along the 13-direction is predicted overly stiff and the flexural wave branch deviates from the reference solution. It is hypothesized that this term is over predicted due to the particular choice of the unit-cell geometry. This then leads to over-constraint effects induced by the lamina-level periodic boundary conditions. Further study into this deviation is performed in the next section.

4.2.4 Scaling factor

It is hypothesized that due to the particular choice of the unit-cell geometry, the torsion-related terms of the unit-cell are over-predicted. This results in the deviation for waves propagating along the $\Gamma - X$ edge of the FIBZ. To investigate the effect on this particular unit-cell, a homogeneous unit-cell is considered first. The top-view of the homogeneous unit-cell is shown in Fig. 4.3(a). The equivalent bending stiffness for bending of the unit-cell along a certain axis $\hat{\vec{e}}_w$ is defined as

$$ {}^4\mathbb{C}^{\text{bb}}_{\text{M,eq}} = \hat{\boldsymbol{e}}_w :^4 \mathbb{C}^{\text{bb}}_{\text{M}} : \hat{\boldsymbol{e}}_w \tag{4.9} $$

with $\hat{\boldsymbol{e}}_w = \hat{\vec{e}}_w \hat{\vec{e}}_w$. Consider the unit-cell embedded in an infinite plate composed of these unit-cells. Then, the equivalent bending stiffness should be isotropic and therefore equal for bending along any in-plane direction $\hat{\vec{e}}_w$. Consider the two axes denoted in Fig. 4.3(a). Bending along the A'-A axis and bending along the B'-B axis corresponds to the respective directions

$$ \hat{\vec{e}}_{\text{w,A}} = \vec{e}^{\,\text{c}}_1 \tag{4.10a} $$

$$ \hat{\vec{e}}_{\text{w,B}} = \tfrac{1}{2}\sqrt{2}\vec{e}^{\,\text{c}}_1 + \tfrac{1}{2}\sqrt{2}\vec{e}^{\,\text{c}}_3 \tag{4.10b} $$

Applying either of these directions to the bending stiffness should result in the same equivalent bending stiffness. However, for the direction $\hat{\vec{e}}_{\text{w,B}}$, one obtains a higher equivalent bending stiffness than for $\hat{\vec{e}}_{\text{w,A}}$ and this can be attributed to over-constraining the square unit-cell according to the lamina-level PBCs. To relax the equivalent bending stiffness, a scaling factor δ is introduced which is applied to the torsion-related components of ${}^4\mathbb{C}^{\text{bb}}_{\text{M}}$. The equivalent bending stiffness for bending along B'-B axis must be the same as bending along the A'-A axis after application of the scaling factor. This results in the following equation, written as

$$ {}^4\mathbb{C}^{\text{bb}}_{\text{M,eq,A}} =^4 \mathbb{C}^{\text{bb}}_{\text{M,eq,B}}(\delta) \tag{4.11} $$

where

$$ {}^4\mathbb{C}_{\text{M,eq,A}} = \hat{\boldsymbol{e}}_{\text{w,A}} :^4 \mathbb{C}^{\text{bb}}_{\text{M}} : \hat{\boldsymbol{e}}_{\text{w,A}} \tag{4.12a} $$

$$ {}^4\mathbb{C}_{\text{M,eq,B}}(\delta) = \hat{\boldsymbol{e}}_{\text{w,B}} :^4 \mathbb{C}^{\text{bb}}_{\text{M,mod}}(\delta) : \hat{\boldsymbol{e}}_{\text{w,B}} \tag{4.12b} $$

Here, ${}^4\mathbb{C}^{\text{bb}}_{\text{M,mod}}(\delta)$ is the modified bending stiffness tensor written in Voigt notation as

$$ {}^4\mathbb{C}^{\text{bb}}_{\text{M,mod}}(\delta) = \begin{bmatrix} \begin{bmatrix} {}^4\mathbb{C}_{\text{M},1111} & {}^4\mathbb{C}_{\text{M},1133} \\ {}^4\mathbb{C}_{\text{M},3311} & {}^4\mathbb{C}_{\text{M},3333} \end{bmatrix} & \begin{matrix} 0 & 0 \\ 0 & 0 \end{matrix} \\ \begin{matrix} 0 & 0 \\ 0 & 0 \end{matrix} & \delta \begin{bmatrix} {}^4\mathbb{C}_{\text{M},1331} & {}^4\mathbb{C}_{\text{M},1313} \\ {}^4\mathbb{C}_{\text{M},3131} & {}^4\mathbb{C}_{\text{M},3113} \end{bmatrix} \end{bmatrix} \tag{4.13} $$

Solving eq. (4.11) yields the scaling factor. Applying δ to the bending stiffness finally yields the modified bending stiffness. The scaling factor is calculated under the assumption that the equivalent bending stiffness is isotropic, i.e., equal for any direction $\vec{e}_{\mathrm{w}}$. To verify whether this assumption is valid, the equivalent bending stiffness is calculated using the modified bending stiffness for varying angle θ. The equivalent bending stiffness should be constant for varying θ since it is assumed to be isotropic. In Fig. 4.3(b) the equivalent modified bending stiffness is shown for varying θ. As one can see from the figure, the equivalent modified bending stiffness does not change. For the sake of comparison, the equivalent bending stiffness without the scaling factor is shown as well which shows the over-constrained effects.

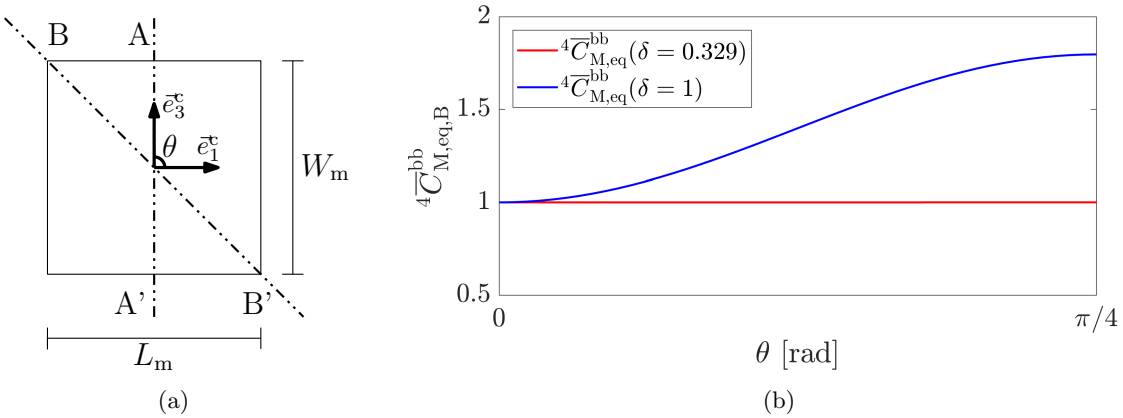

Figure 4.3: *Top-view of a homogeneous unit-cell with two bending axes (a) and the normalized equivalent bending stiffness as function of the θ (b).*

The study on the scaling factor has been performed on a homogeneous unit-cell. However, in Fig. 1.2(a) it was shown that an LRAM unit-cell can be considered as a thin host plate to which a resonator is connected through a linear spring. Hence, the bending stiffness of the plate is dominated by the host material. This means that the scaling factor obtained from the method above can also be applied to the LRAM unit-cell as long as the separation of scales is satisfied. Considering the unit-cell in Fig. 4.1, the tungsten core is surrounded by the soft rubber coating and therefore merely participating in the bending stiffness. This means that also for this configuration, the scaling factor defined above can be applied to relax the bending stiffness.

In Fig. 4.4a the dispersion spectrum along the $\Gamma - X$ direction is shown after application of the scaling factor. Taking a closer look at the flexural wave branches, it can be seen that the response computed by the homogenization method matches the reference solution much better. In Fig. 4.4b the deviations on the phase velocity of the first 5 flexural wave branches are shown and it can be seen that the maximum absolute error is 1.94% for a relaxed bending stiffness. This deviation is comparable to the deviations that were found for the compressive and flexural waves propagating along the $\Gamma - M$ path. Hence, the response of the homogenization method still shows a slight deviation, but the match with the reference solution is much better. In the remainder of this thesis the modified bending stiffness will be used as well.

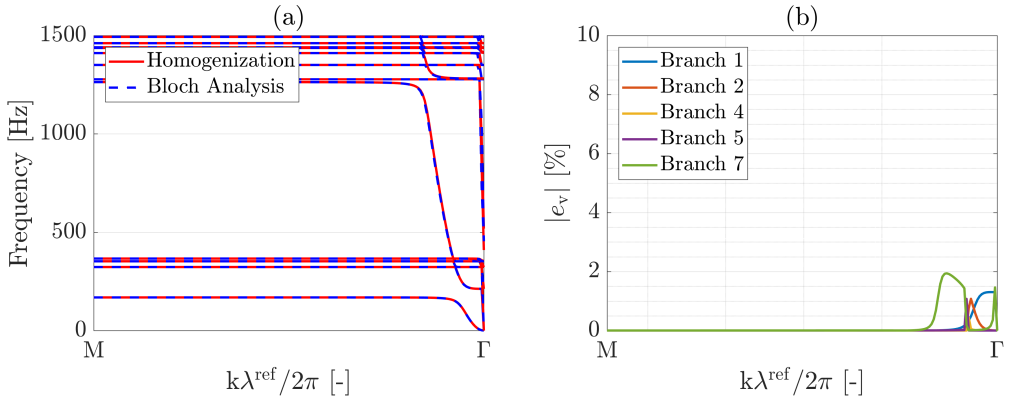

Figure 4.4: *Real dispersion spectra according to a modified bending stiffness (a) and the error on the flexural wave branches (b).*

To conclude the validation of the homogenization framework on the infinite LRAM plate, the computation times for the dispersion analysis by homogenization method and the Bloch Analysis are compared in Tab. 4.5. For comparison, both simulations are performed on the *MaTe*-cluster of the materials technology department of the TU/e. The Matlab version running on this cluster is Matlab v.2014b. The on-line computation time of the homogenization method is composed of the time needed to compute the model reduction (resulting in the reduced dynamic model) and the actual dispersion analysis. Due to the model reduction, the number of DOFs for the homogenized model is much lower and therefore, the computational gain of the homogenization method with respect to the FEM-based Bloch analysis is high. The deviation mentioned in the table is the maximum deviation of the homogenized response with respect to the reference solution within the analysed frequency range. Since the maximum deviation does not exceed 2%, it can be concluded with confidence that the separation of scales is not violated within this frequency range.

Software	**Method**	**Computation time [s]**	**Gain**	**Error [%]**
Matlab v. 2014b	Homogenization method	50.8	162	1.94
Matlab v. 2014b	Bloch analysis	8267.8	-	-

Table 4.5: *Computation times for the dispersion analysis*

In conclusion, the homogenization method yields an accurate description of the dispersion analysis of an infinite LRAM plate for off-diagonal propagation directions in the first Brillouin zone. Moreover, the homogenization framework performs the dispersion analysis much faster compared than the traditional FEM-based Bloch analysis showing the strength of the framework.

Chapter 5

Validation on a finite LRAM plate

In this section, the homogenization framework is validated on a finite LRAM plate. This will lead to a solid validation of the framework, and yield more insights into the macroscopic behaviour of LRAM plates. For the numerical implementation of the macroscopic plate, isogeometric analysis (IGA) will be employed here. The macroscopic problem defined in Section 2.1 is enriched by the upscaled microscopic balance of momentum defined in Section 3.3. The unit-cell analysed in the previous section used here to determine the effective macroscopic material properties and the emergent degrees of freedom to enrich the macroscopic problem. The enriched homogenized macroscopic response (enriched single-scale analysis) of the finite LRAM plate subjected to certain boundary conditions is then compared to a reference solution obtained from FEM-based DNS (full-scale analysis).

5.1 Implementing the enriched macroscopic problem

5.1.1 Weak form problem

The macroscopic weak form problem defined in eq. 2.6 is enriched by the upscaled microscopic balance equation defined in 3.23. First of all, the macroscopic weak form is relaxed by neglecting the rotational inertia $\dot{\vec{Q}}_{\mathrm{M}}$ as it is negligible compared to linear inertia. Also $\tilde{\vec{c}}_{\mathrm{M}}$ is eliminated from the expression by expressing it in terms of $\vec{v}_{\mathrm{M,r}}$ as $\tilde{\vec{c}}_{\mathrm{M}} = -\hat{\tilde{\vec{\nabla}}}_{\mathrm{M}}(\tilde{\vec{e}}^{\mathrm{c}} \cdot \tilde{\vec{v}}_{\mathrm{M,r}})$. This results in the relaxed macroscopic weak form as

$$\begin{aligned}&\int_{\mathcal{A}_{\mathrm{M,r}}} \left[\hat{\tilde{\vec{\nabla}}}_{\mathrm{M}} \vec{v}_{\mathrm{M,r}}\right]^{\mathrm{T}} : \hat{\mathbb{N}}_{\mathrm{M}} \mathrm{d}A_{\mathrm{M}} - \int_{\mathcal{A}_{\mathrm{M,r}}} \left[\hat{\tilde{\boldsymbol{\Delta}}}_{\mathrm{M}} (\tilde{\vec{e}}^{\mathrm{c}} \cdot \tilde{\vec{v}}_{\mathrm{M,r}})\right]^{\mathrm{T}} : \hat{\mathbb{M}}_{\mathrm{M}} \mathrm{d}A_{\mathrm{M}} + \int_{\mathcal{A}_{\mathrm{M,r}}} \vec{v}_{\mathrm{M,r}} \cdot \dot{\vec{P}}_{\mathrm{M}} \mathrm{d}A_{\mathrm{M}} = \\ &\int_{\mathcal{C}_{\mathrm{M,r},t}} \vec{v}_{\mathrm{M,r}} \cdot \vec{t}_{\mathrm{M}} \mathrm{d}C_{\mathrm{M}} - \int_{\mathcal{C}_{\mathrm{M,r},m}} \hat{\tilde{\vec{\nabla}}}_{\mathrm{M}} \left[\tilde{\vec{e}}^{\mathrm{c}} \cdot \tilde{\vec{v}}_{\mathrm{M,r}}\right] \cdot \vec{m}_{\mathrm{M}} \mathrm{d}C_{\mathrm{M}}, \ \forall \vec{v}_{\mathrm{M,r}} \in \mathcal{U}^2\end{aligned} \tag{5.1}$$

where $\hat{\tilde{\boldsymbol{\Delta}}}_{\mathrm{M}} = \hat{\tilde{\vec{\nabla}}}_{\mathrm{M}} \hat{\tilde{\vec{\nabla}}}_{\mathrm{M}}$ and $\mathcal{U}^2$ the second order Sobolev function space. This second order Sobolev function space is necessary because of the double gradient operator on the test function $\vec{v}_{\mathrm{M,r}}$. This means that the test-function must be at-least second order derivable.

To enrich the macroscopic weak form, the weighted residuals form of the upscaled microscopic balance of momentum must be obtained. This is achieved by subsequently multiplying eq. 3.23 by τ_n, the test-function of emergent DOF ζ_n, and integrating the

expression over reference lamina domain $\mathcal{A}_{\mathrm{M,r}}$. This then results in the following expression

$$\begin{aligned}&\int_{\mathcal{A}_{\mathrm{M,r}}} \tau_n \omega_{\mathrm{n}}^2 \zeta_n \mathrm{d}A_{\mathrm{M}} + \int_{\mathcal{A}_{\mathrm{M,r}}} \tau_n \ddot{\zeta}_n \mathrm{d}A_{\mathrm{M}} + \int_{\mathcal{A}_{\mathrm{M,r}}} \tau_n \mathbf{h}_n^{\mathrm{lm}} : \ddot{\hat{\mathbb{H}}}_{\mathrm{M}}^{\mathrm{T}} \mathrm{d}A_{\mathrm{M}} + \int_{\mathcal{A}_{\mathrm{M,r}}} \tau_n \mathbf{h}_n^{\mathrm{rt}} : \ddot{\hat{\mathbb{H}}}_{\mathrm{M}}^{\mathrm{T}} \mathrm{d}A_{\mathrm{M}} \\ &+ \int_{\mathcal{A}_{\mathrm{M,r}}} \tau_n \vec{j}_n^{\mathrm{lm}} \cdot \ddot{\vec{u}}_{\mathrm{M,r}} \mathrm{d}A_{\mathrm{M}} = 0,\ n = 1, 2, .., N_{\mathrm{d}}^*,\ \forall \tau_n \in \mathcal{U}^0\end{aligned} \tag{5.2}$$

with $\mathcal{U}^0$ the zeroth-order Sobolev solution space. By coupling eqs. (5.1) and (5.2), the enriched macroscopic problem can be solved for the unknown macroscopic and emergent displacement variables $\vec{u}_{\mathrm{M,r}}$ and ζ_n.

5.1.2 Isogeometric analysis

For the numerical implementation of the enriched macroscopic problem, isogeometric discretization technique will be employed. Through the IGA implementation of the macroscopic problem, two major advantages are presented compared to standard FEM. First of all, the geometry of the macroscopic problem can be represented exactly using computer-aided design (CAD) basis functions. This means that the design of a particular model can directly be used for analysis purposes without the need of meshing. The basis functions used for the geometric description of the model are also used to discretize the variables describing the deformation field. Another advantage of isgeometric analysis is the higher order continuity over element boundaries compared to Lagrange basis functions often employed in FEM. Due to this property, the basis functions can be used to discretize higher-order differential equations with inter-element continuity, which is the case for the bending equation. For the discretization of the Kirchoff-Love shell description employed at the macroscale, at least C^1 continuity is needed. Due to the recursive definition of the basis functions, the continuity can be chosen sufficiently high such that it fits the model requirements [43, 44].

The macroscopic shell geometry introduced in Chap. 2 is defined in terms of the in-plane coordinate $\vec{\xi}_{\mathrm{M}}$. According to IGA, the coordinate $\vec{\xi}_{\mathrm{M}}$ in 3D physical space is mapped onto the 2D parametric domain by defining it as a linear combination of the bivariate basis-functions R_{M} and a 3D control-net. Alternatively, the macroscopic and emergent displacement fields can also be written in terms of these bivariate basis functions and a corresponding control net as

$$\vec{u}_{\mathrm{M,r}}(\psi_{\mathrm{M}}, \chi_{\mathrm{M}}) = \underset{\sim}{R}_{\mathrm{M}}(\psi_{\mathrm{M}}, \chi_{\mathrm{M}}) \underset{\sim}{\vec{a}}_{\mathrm{M}} \tag{5.3a}$$

$$\zeta_{\mathrm{n}}(\vec{\psi}_{\mathrm{M}}, \vec{\chi}_{\mathrm{M}}) = \underset{\sim}{R}_{\mathrm{M}}(\vec{\psi}_{\mathrm{M}}, \vec{\chi}_{\mathrm{M}}) \underset{\sim}{\kappa}_n,\ n = 1, 2, .., N_{\mathrm{d}}^* \tag{5.3b}$$

where ψ_{M} and χ_{M} are the parametric coordinates in the 2D parametric domain. $\underset{\sim}{R}_{\mathrm{M}}$ is the column with bivariate spline basis functions and $\vec{a}_{\mathrm{M}}$ and κ_n are the control variables of the macroscopic and emergent displacement fields, respectively. These control variables do not have to be located in the physical domain. The bivariate basis functions are defined by the tensor product of two univariate basis functions in parametric dimensions ψ_{M} and χ_{M}.

According to the Galerkin approach, the macroscopic and emergent displacement fields can be expressed in terms of the same basis functions and their corresponding test functions $\vec{v}_{\mathrm{M,r}}$ and τ_{n}. Also the first- and second-order in-plane gradients of the displacement fields and test functions are expressed in terms of the basis functions. Finally, substituting all discretized variables into the enriched macroscopic description, it can be written as a set of discretized balance equations as

$$\underline{\mathcal{B}}_{\mathrm{M}} \cdot \underset{\sim}{\mathcal{U}}_{\mathrm{M}} + \underline{\mathcal{W}}_{\mathrm{M}} \cdot \underset{\sim}{\ddot{\mathcal{U}}}_{\mathrm{M}} = \underset{\sim}{\mathcal{F}}_{\mathrm{M}} \tag{5.4}$$

where $\underline{\mathcal{B}}_{\mathrm{M}}$ and $\underline{\mathcal{W}}_{\mathrm{M}}$ are the assembled stiffness and mass matrix and $\underset{\sim}{\mathcal{U}}_{\mathrm{M}}$ and $\underset{\sim}{\mathcal{F}}_{\mathrm{M}}$ are the assembled displacement and force vector columns defined as

$$\underline{\mathcal{B}}_{\mathrm{M}} = \begin{bmatrix} \underline{\mathcal{B}}_{\mathrm{M},uu} & \vec{\underline{0}} & \vec{\underline{0}} & \vec{\underline{0}} \\ \vec{\underline{0}} & \ddots & \vec{\underline{0}} & \vec{\underline{0}} \\ \vec{\underline{0}} & \vec{\underline{0}} & \underline{\mathcal{B}}_{\mathrm{M},\zeta\zeta,nn} & \vec{\underline{0}} \\ \vec{\underline{0}} & \vec{\underline{0}} & \vec{\underline{0}} & \ddots \end{bmatrix}, \; \underline{\mathcal{W}}_{\mathrm{M}} = \begin{bmatrix} \underline{\mathcal{W}}_{\mathrm{M},uu} & \cdots & \underline{\mathcal{W}}_{\mathrm{M},u\zeta,n} & \vec{\underline{0}} \\ \cdots & \ddots & \vec{\underline{0}} & \vec{\underline{0}} \\ \underline{\mathcal{W}}_{\mathrm{M},\zeta u,n} & \vec{\underline{0}} & \underline{\mathcal{W}}_{\mathrm{M},\zeta\zeta,nn} & \vec{\underline{0}} \\ \vec{\underline{0}} & \vec{\underline{0}} & \vec{\underline{0}} & \ddots \end{bmatrix} \tag{5.5a}$$

$$\underset{\sim}{\mathcal{U}}_{\mathrm{M}} = \begin{bmatrix} \mathcal{U}_{\mathrm{M},u} \\ \cdots \\ \mathcal{U}_{\mathrm{M},\zeta,n} \\ \cdots \end{bmatrix}, \; \underset{\sim}{\mathcal{F}}_{\mathrm{M}} = \begin{bmatrix} \mathcal{F}_{\mathrm{M},u} \\ \cdots \\ \mathcal{F}_{\mathrm{M},\zeta,n} \\ \cdots \end{bmatrix}, \; n = 1, 2, .., N_{\mathrm{d}}^{*} \tag{5.5b}$$

where the subscripts $(\bullet)_{,u}$ and $(\bullet)_{,\zeta}$ are the field variables corresponding to the macroscopic and emergent displacement field, respectively. The subscripts $(\bullet)_{,uu}$ and $(\bullet)_{,\zeta\zeta,nn}$ denote the self-coupling of the displacement fields. Notice the coupling terms in the assembled mass matrix between the macroscopic and the emergent displacement field by the subscripts $(\bullet)_{\zeta n}$ and $(\bullet)_{n\zeta}$. The full description of the matrix- and column-entries of eq. (5.5) can be found in App. B. Notice that in the generalized stiffness and mass matrices in eq. (5.5), each macroscopic displacement degree of freedom is related to each emergent degree of freedom ζ_n.

The entries of the generalized stiffness and mass matrix are calculated by means of numerical integration over the parametric domain according to the Gauss quadrature. The number of integration points for the isogeometric elements is related to the order of the basis functions. Once the discrete system of equations is solved, the desired response fields (force and displacement) must be calculated from the displacements of and forces acting on the control coefficients. This can easily be done by inserting the appropriate fields into eq. (5.3).

5.1.3 Boundary conditions

In order to solve for the macroscopic and emergent displacement fields, the macroscopic boundary conditions must be applied to the discretized system of equations. Starting with the Neumann boundary conditions, they are defined in terms of the in-plane tying tractions and moment resultants $\hat{\vec{t}}_{\mathrm{M}}$ and $\hat{\vec{m}}_{\mathrm{M}}$. From the definition of $\underset{\sim}{\mathcal{F}}_{\mathrm{M},u}$, these boundary conditions can be directly implemented. Secondly, the Dirichlet boundary conditions are to be implemented in $\underset{\sim}{\mathcal{U}}_{\mathrm{M},u}$. By certain choices of the control-net, the Dirichlet boundary conditions can be handily implemented. Finally, partitioning the discretized system in eq. (5.4) into prescribed and free degrees of freedom enables to solve for the unknown quantities.

Solving eq. (5.5) will result in the displacement of the macroscopic control variables. To obtain the physical macroscopic displacement field, one must substitute the solution to eq. (5.3).

5.1.4 Steady-state response

Considering the finite LRAM plate under a harmonic excitation, it is interesting to investigate its steady-state response. When investigating the steady-state response, only the response after sufficiently long time is evaluated. Then the initial conditions do not have an influence on the structural response, and it becomes independent of time. This means that the displacement and force variables do not change with time anymore, and $\underset{\sim}{\mathcal{U}}_{\mathrm{M}}$ and $\underset{\sim}{\mathcal{F}}_{\mathrm{M}}$ are

split into a space- and time-dependent term as

$$\underset{\sim}{\mathcal{U}}_{\mathrm{M}} = \underset{\sim}{\mathcal{U}}^{\mathrm{ss}}_{\mathrm{M}} \exp^{i\omega t} \tag{5.6a}$$

$$\underset{\sim}{\mathcal{F}}_{\mathrm{M}} = \underset{\sim}{\mathcal{F}}^{\mathrm{ss}}_{\mathrm{M}} \exp^{i\omega t} \tag{5.6b}$$

where the superscript $(\bullet)^{\mathrm{ss}}$ denotes the space-dependent part of the solution and $\exp^{i\omega t}$ denotes the time-dependent part. Substituting these conditions into the discretized system in eq. (5.5), the steady-state balance equation is defined as

$$[\underline{\mathcal{B}}_{\mathrm{M}} - \omega^2 \underline{\mathcal{W}}_{\mathrm{M}}] \cdot \underset{\sim}{\mathcal{U}}^{\mathrm{ss}}_{\mathrm{M}} = \underset{\sim}{\mathcal{F}}^{\mathrm{ss}}_{\mathrm{M}} \tag{5.7}$$

The free displacement variables and forces can be solved by eliminating the prescribed quantities from the steady-state balance equations.

5.1.5 Transient response

In many physical applications, analysing the steady-state response alone does not suffice. If a structural vibration is applied to the structure for limited time, the time-dependency should be taken into account as well. To this extent, the transient response of a finite panel is analysed. In [29] the Newmark time-integration scheme is introduced.

The Newmark integration scheme requires the initial and boundary conditions of the system together with the discretized system of equations in eq. (5.5). For each time-step Δt, the scheme predicts the displacement and velocity coefficients. Then the acceleration is solved with these predicted quantities. At last, the predicted quantities are corrected with the calculated acceleration field. This scheme is repeated for each time-step within the defined time range. For the full integration scheme, one is referred to [29].

To avoid any high-frequency noise, two numerical parameters are introduced according to a so-called generalized α-scheme. These parameters β and γ and are dependent on the parameter α. In the analysis which follows, it will be described which value for α is used.

5.2 Finite LRAM plate analysis

In this section the steady-state and transient response of a finite LRAM plate is analysed. The homogenized macroscopic response is computed in Matlab v. 2014b on the *MaTe*-cluster. This response is compared to a reference solution obtained from FEM-based DNS computed by COMSOL v.5.3 also on the MaTe cluster. First of all, the isogeometric basis functions and the control net employed in the isogeometric analysis are defined. Then the results are discussed to conclude the validation of the homogenization framework.

5.2.1 Macroscopic configuration

To compare the macroscopic response computed by the enriched single-scale analysis to the full-scale analysis computed by FEM-based DNS, the finite LRAM plate is composed of an array of LRAM unit-cells which were also employed in the analysis of the infinite LRAM plate. To define the macroscopic in-plane dimensions of the finite plate, the number of degrees of freedom of the full-scale analysis is the limiting factor. From the dispersion analysis, it was determined that the number of DOFs of one unit-cell is equal to 4131. Hence, constructing an array of only a few in-plane unit-cells will already lead to a model of large proportions. Since the enriched continuum shell description is based on the Kirchoff-Love shell, the out-of-plane curvature of the finite plate must be much larger than the in-plane

dimensions of the microscopic unit-cell. It is therefore a trade-off between the large amount of DOFs and the out-of-plane radius of curvature of the plate.

Two case studies are introduced for the validation of the finite LRAM plate. The first case study is illustrated in Fig. 5.1(a-b). A rectangular LRAM plate composed of 40x10 unit-cells is excited by a prescribed displacement $\vec{u}_{\mathrm{M,p}}(t)$ which can be time-dependent. The right edge of the plate is simply supported. The remaining edges and the top and bottom surface of the plate remain free. With this case-study, the homogenization framework is mainly validated for wave propagation in one direction only. Therefore, a second case study is introduced in Fig. 5.1(c-d). A square LRAM plate composed of 25x25 unit-cells is excited with the same prescribed displacement $\vec{u}_{\mathrm{M,p}}(t)$ and the three remaining corners are simply supported. The edges in between the prescribed corners and the top and bottom surface of the plate remain free. With this case-study, the homogenization framework is validated on the finite plate for waves propagating in two directions. Some details on the macroscopic configuration for both case-studies is summarized in Tab. 5.1.

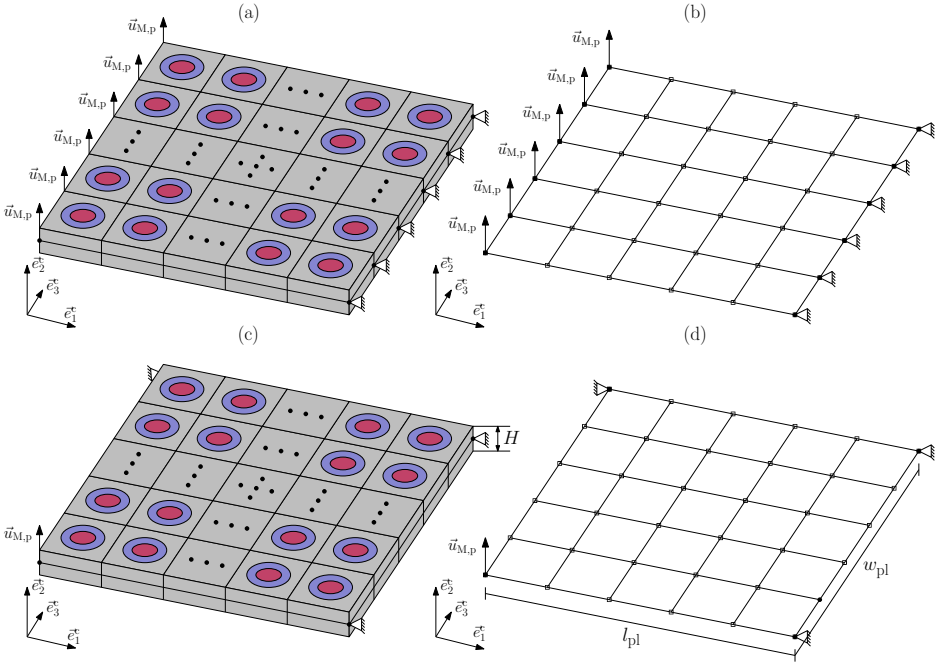

Figure 5.1: *Full-scale finite LRAM plate composed of multiple LRAM unit-cells (a) and its enriched single-scale representation (b) according to case study I. In (c) and (d) the configurations for case study II are shown.*

Quantity	**Unit**	**Case-study I: Edge excitation**	**Case-study II: Corner excitation**
l_{pl}	[mm]	400	250
w_{pl}	[mm]	100	250
H	[mm]	5	5
# unit-cells $\vec{e}_1^{\,t}$	[-]	40	25
# unit-cells $\vec{e}_3^{\,t}$	[-]	10	25
# DOFs	[-]	2079027	3245427

Table 5.1: *Details on the full-scale macroscopic configuration.*

5.2.2 Isogeometric discretization

In Fig. 5.1b, the enriched single-scale representation of the macroscopic LRAM plate is shown. To discretize the finite LRAM plate within IGA, the basis functions and the control net must be defined. For this implementation it is chosen for B-spline basis functions [45]. Although the system of equations in eq. (5.5) requires the basis functions to be at least 2nd order derivable, the B-spline basis functions applied to the finite plate are of order 3. This is chosen for, since the third order basis functions are proven to yield an accurate response for vibrational analysis of beams or plates. The 2D B-spline surface is defined by eq. (5.3a). The basis functions represented by $\underset{\sim}{R}_{\mathrm{M}}(\psi_{\mathrm{M}}, \chi_{\mathrm{M}})$ are a tensor product of two 1D B-spline basis functions $N_p(\psi)$ and $M_q(\chi)$ where p and q are the order of the basis functions (both 3 in this case) and Ψ and X are the knot-vectors over which the basis functions are defined in their corresponding directions. The control net collected in the vector column $\underset{\sim}{\vec{a}}_{\mathrm{M}}$ consists of n x m control points. For B-spline basis functions, each control point requires a weight w. Yet, since only flat LRAM plates are considered, these weights are equal to 1 for each control point. The length of the knot vectors and the number of control points in both in-plane directions depend on the macroscopic dimensions. The number of isogeometric elements in ψ- and χ-direction is defined as v and z, respectively. For a third order B-spline basis function, the knot vector Ψ is of length $n+p+1$ and X is of length $m+q+1$. The first and last knot in this vector have multiplicity $p+1$ and $q+1$, respectively, denoting these vectors as open knot vectors. Due to this property, the application of boundary conditions at the edges and corners of the finite plate becomes easy. The normalized knot vectors for both B-spline basis functions are defined in eq. 5.8(a-b).

$$\Psi = \frac{1}{v}\left[\underbrace{0,\ldots,0}_{p+1}, 1, 2, \ldots, v-1, \underbrace{v,\ldots,v}_{p+1}\right] \tag{5.8a}$$

$$X = \frac{1}{z}\left[\underbrace{0,\ldots,0}_{q+1}, 1, 2, \ldots, z-1, \underbrace{z,\ldots,z}_{q+1}\right] \tag{5.8b}$$

$$\underset{\sim}{\vec{a}}_{\mathrm{M}} \cdot \vec{e}_1^{\,\mathfrak{r}} = \frac{l_{\mathrm{pl}}}{v}\left[0, \frac{1}{3}, 1, 2, \ldots, v-2, v-1, \frac{3v-1}{3}, v\right] \tag{5.8c}$$

$$\underset{\sim}{\vec{a}}_{\mathrm{M}} \cdot \vec{e}_3^{\,\mathfrak{r}} = \frac{w_{\mathrm{pl}}}{z}\left[0, \frac{1}{3}, 1, 2, \ldots, z-2, z-1, \frac{3z-1}{3}, w\right] \tag{5.8d}$$

The control net is constructed by assembling the 1D control nets of both in-plane directions defined in eq. (5.8(c-d). By defining the control net in such a manner, the mapping from the parametric domain to the physical domain is linear. Also, by defining the control net suiting the finite plate dimensions, the constraints on the displacements as shown in Fig. 5.1b, can be directly applied to the corresponding control points at the boundaries. Before the homogenization method is validated on the finite plate, the implementation of the isogeometric framework must be validated. To this extent, an eigenfrequency analysis is performed on a thin plate with equal dimensions as the plates shown in Figs. 5.1(b-d) with homogeneous material properties. The result from isogeometric analysis is compared to analytic solutions. Since the homogeneous plate has the same dimensions as the LRAM plate, a convergence study is simultaneously performed on the isogeometric mesh. After performing the eigenfrequency analysis, the isogeometric implementation is validated and a suitable number of isogeometric elements was determined at $v = 16$,$z = 4$ and $v = z = 12$ for case-study I and II, respectively. The univariate third order B-spline basis-functions defined on the knot vectors Ψ and $X$are shown in Figs. 5.2(a-c). Next to the basis-functions, a

top-view of the discretized LRAM plate is shown in Figs. 5.2(b-d). The black lines on the plate denote the isogeometric elements, separated by the knots. The dashed red lines and the red circles denote the control net and the control points, respectively.

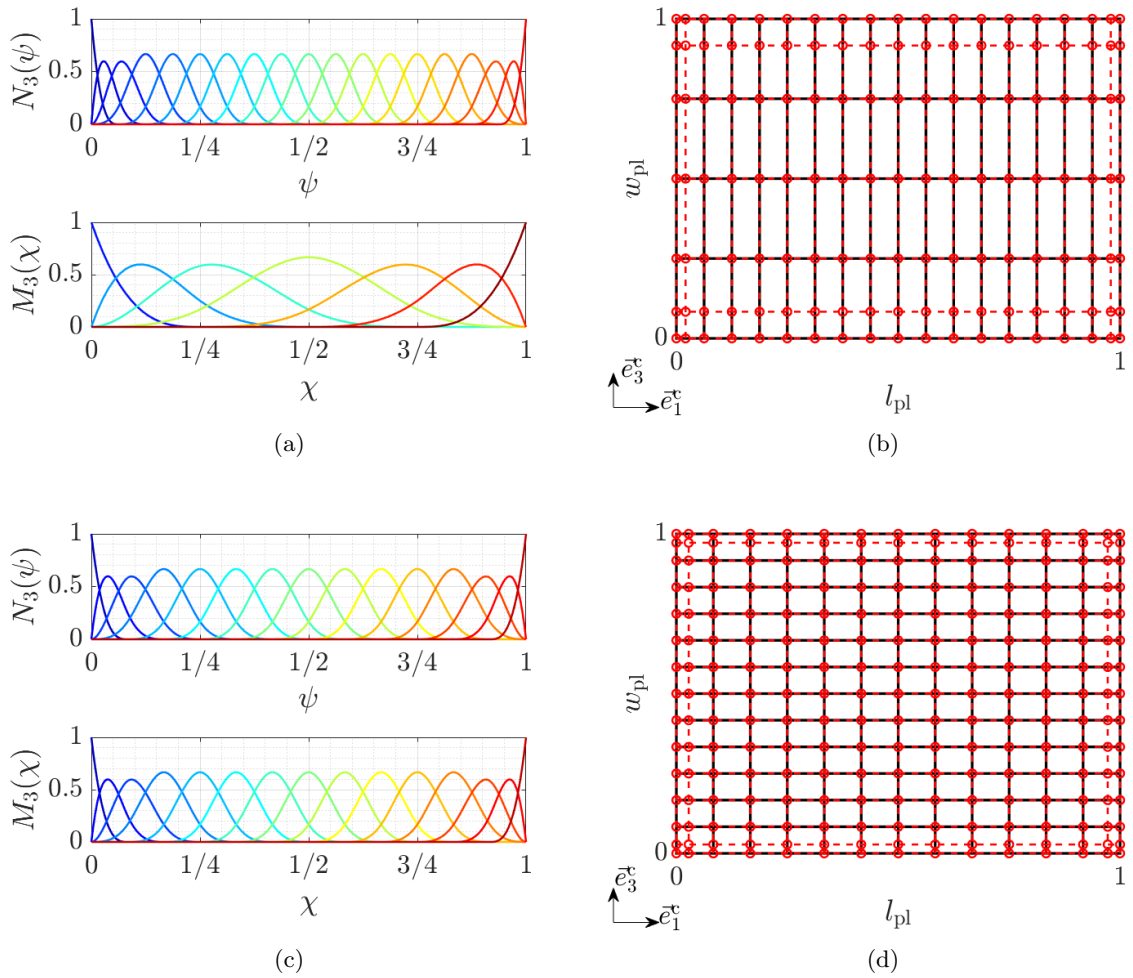

Figure 5.2: *Univariate third order B-spline basis functions and the corresponding discretized LRAM plate corresponding to case study I (a-b) and case study II (c-d).*

5.2.3 Frequency response analysis

The steady-state response of the finite LRAM plate to under certain excitation can be represented in a frequency response plot. This plot shows the response of the plate as function of the excitation frequency of the input signal. The plate is excited at either the left edge or one corner by a vertical displacement U_{in}. From the dispersion analysis it was already derived what eigenmodes have an active contribution to the response of the LRAM plate. To this extent, the same active eigenmodes are employed here to enrich the macroscopic displacement degrees of freedom. Then, by extracting the vertical amplitude U_{out} at certain pre-defined gauge points located within the LRAM plate, a frequency response plot is created. The positions of the gauge points for the two case-studies are shown in Tab. 5.2. Since the plate response computed by the homogenization method is compared to FEM-based DNS, the gauge points are located at the matrix and not at the inclusion.

The frequency response plot only shows the response of the plate at the gauge points,

GP	Case-study I: Edge excitation		Case-study II: Corner excitation	
	$\vec{e}_1^{\mathfrak{t}}$	$\vec{e}_3^{\mathfrak{t}}$	$\vec{e}_1^{\mathfrak{t}}$	$\vec{e}_3^{\mathfrak{t}}$
GP_1	$16L_{\mathrm{m}}$	$5W_{\mathrm{m}}$	$10L_{\mathrm{m}}$	$10W_{\mathrm{m}}$
GP_2	$32L_{\mathrm{m}}$	$5W_{\mathrm{M}}$	$20L_{\mathrm{m}}$	$10W_{\mathrm{m}}$
GP_3	-	-	$20L_{\mathrm{m}}$	$20W_{\mathrm{m}}$

Table 5.2: *Locations of the gauge points on the finite LRAM plate for two macroscopic configurations, respectively.*

i.e. the local deformation. Yet, it is interesting to see the response of the LRAM plate over the entire physical domain, i.e. the global deformation. Therefore, the global deformation of the homogenized plate is shown at certain frequencies in the up-coming analysis. The frequency range over which the steady state response is computed, is taken to be the same as for the dispersion analysis, being $0 - 1500$ Hz. The results of the steady state response are shown in Sec. 5.3.

5.2.4 Transient analysis

To analyse the transient response of the finite LRAM plate, a vertical harmonic input signal of frequency f is subjected to the plate. The input excitation is written as

$$u_{\mathrm{in}}(f,t) = U_{\mathrm{in}}\left[1 - \cos(2\pi f t)\right] \tag{5.9}$$

where U_{in} is the input amplitude, f is the frequency and $t \in [0, 3T]$ is the duration of the input signal. The time-duration is limited by the period T of the frequency and for this study only 3 periods are employed. It is chosen to take 3 periods, since the time-dependent study of the full-scale analysis is computationally expensive. The frequencies at which the simulations are performed are taken to be the same as the frequencies at which the full-field steady-state response is computed. In Sec. 5.1.5 the generalized alpha scheme was introduced. For the up-coming analysis, the governing parameter α is set as $\alpha = 0.2$. To verify whether this is a valid choice, the transient response of a finite plate with homogeneous material properties computed by the Newmark integration scheme has been compared to the full-scale analysis.

As for the stedy-state response of the finite plate, the transient response is initially analysed at the same gauge-points defined in Table 5.2 as function of time. This analysis shows whether the homogenization method is able to accurately capture the transient response at each point in the pre-defined time range. Finally, the global deformation of the LRAM plate is given at the final time $t = 3T$. The results of the transient analysis are shown in Sec. 5.4.

5.3 Case-study I

5.3.1 Steady-state response

The frequency response functions of the out-of-plane displacement at the gauge points for case-study I are shown in Fig. 5.3. The enriched single-scale response is denoted by the solid red line, whereas the full-scale response computed by DNS is denoted by the dashed blue line. The flexural wave band-gaps are marked by the green area and have the same size as those found in the dispersion analysis. U_{out} represents the vertical amplitude at the gauge point.

Comparing the enriched single-scale response at both gauge points to those of the full-scale simulation, it can be concluded that a good match exists. The homogenization method predicts the frequency response within great accuracy. At low frequency the match is very good and as the frequency increases the homogenized response is somewhat overestimated. This results in a shift of the resonance peaks computed by the homogenization method with respect to the results of FEM-based DNS. The deviation becomes more pronounced for higher frequencies since the influence of transverse shear effects on the response are not negligible any more. Although the separation of scales is not violated within this frequency range, the increasing influence of the transverse shear effects are definitely visible. The deviation between the two methods is determined to be at most 2.2% within the analysed frequency range.

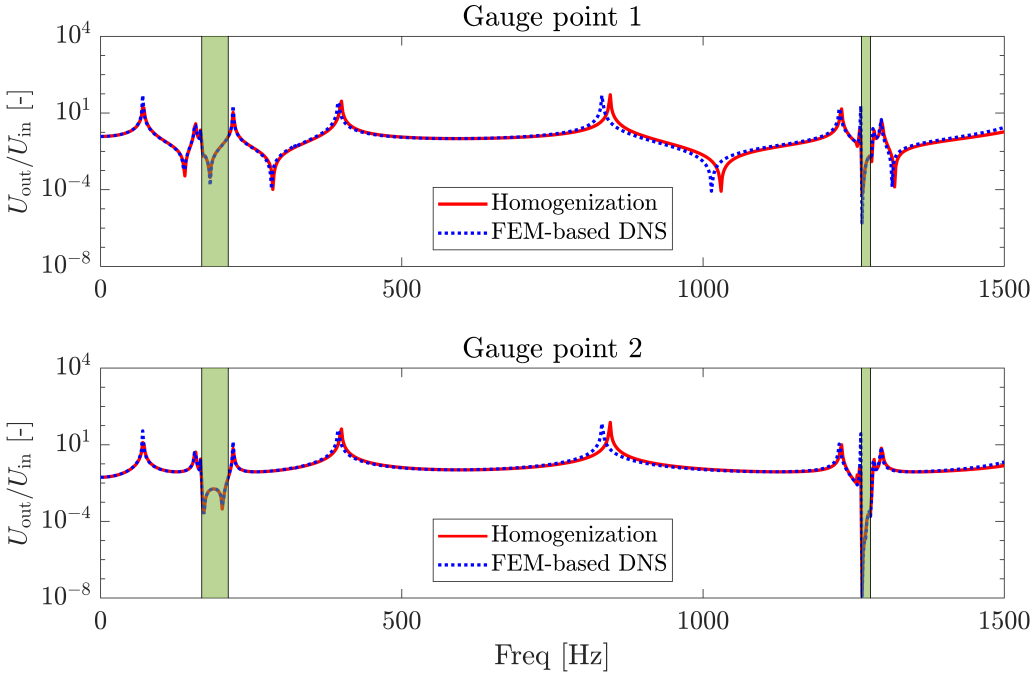

Figure 5.3: *Frequency response functions of the macroscopic out-of-plane displacement of two gauge points according to the configuration of case-study I.*

Comparing the homogenized frequency response at the gauge points one can clearly see that the first flexural wave band-gap is not clearly visible yet at the first gauge point, whereas it is definitely captured at the second gauge point. For the second flexural wave band-gap however, this one is already activated at the first gauge point. The flexural waves being attenuated in the first band-gap have a longer wavelength than the waves attenuated in the second band-gap. This can be the reason that the second flexural wave band-gap is captured at the first gauge point and the first band-gap is only captured at the second gauge-point. Another cause may be the fact that the distance over which the wave propagates is too small to effectively attenuate the flexural wave for the first gauge point. The locations of the flexural wave band-gaps matches the locations in the dispersion spectra, although the size of the first flexural wave band-gap is slightly smaller in the frequency response plot employed here. This might also be attributed to the fact that the in-plane macroscopic dimensions of the finite plate are not large enough to accurately capture the entire band-gap.

Whilst analysing the dispersion spectra in Fig. 4.2(d-I) also two body wave frequency band-gaps could be obtained. When looking at the frequency response plots in Fig. 5.3,

these band-gaps are not observed. This is due to the fact that the finite plate is subjected to an out-of-plane input-excitation. This means that the in-plane eigenmodes are not activated, resulting in the absence of the body-wave induced frequency band-gaps in Fig. 5.3.

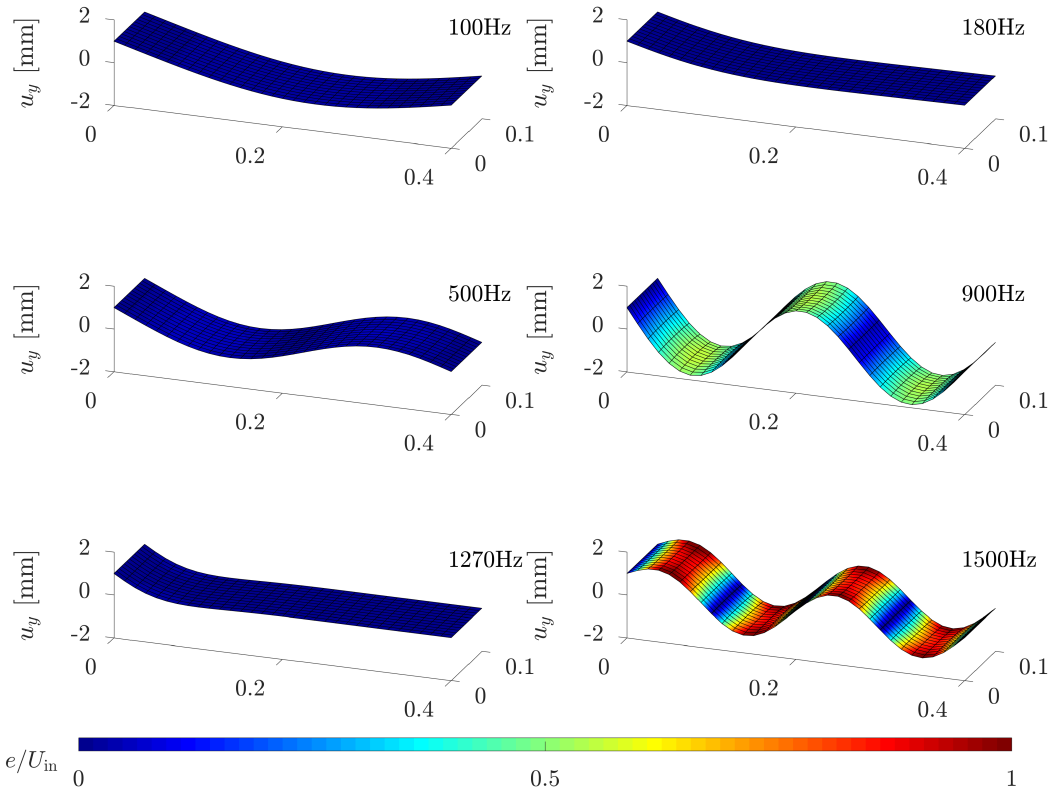

Figure 5.4: *Global steady state deformation at 6 excitation frequencies computed by the homogenization method. The color-scale indicates the absolute normalized deviation with respect to the reference solution.*

The global steady state response is evaluated at a range of excitation frequencies shown in Fig. 5.4. The global deformation computed by the enriched single-scale analysis is revealed with the color-scale expressing the normalized deviation e/U_{in}. The deviation is defined as the absolute difference between the out-of-plane displacement computed by the enriched single-scale response and the full-scale response. Regarding the full-scale response, the out-of-plane displacement of the neutral plane is evaluated at the material points in the matrix material to yield a fair comparison. The global response is computed at 6 frequencies within the defined range, being $f = \{100, 180, 500, 900, 1270, 1500\}$ Hz. The frequencies $f = \{180, 1270\}$ Hz are located inside the first and second flexural wave band-gap, respectively. Starting from the first frequency, it can be seen that the excitation at 100 Hz leads to an out-of-plane distortion of the entire plate. This is due to the fact that the no local resonance is active yet and the response is dominated by the matrix material. Continuing to the global deformation at $f = 180$ Hz, the excitation is attenuated throughout the plate. As the excitation frequency is located inside the frequency band-gap, it activates the first out-of-plane eigenmode (Fig. 4.2(a)) effectively attenuating the out-of-plane displacement. The global response at both 500 Hz and 900 Hz again show a distortion throughout the entire plate dominated by the matrix material as well. Shifting towards the global deformation at

1270 Hz, the second out-of-plane eigenmode is activated (Fig. 4.2(e)) and the decaying effect is even stronger than for the 180 Hz panel. Notice that this difference between the decaying effect for both band-gaps was also observed in the frequency response plots. Moving away form the second band-gap towards the global deformation at 1500 Hz, the out-of-plane distortion throughout the entire plate is clearly visible again.

One may easily compare the enriched single-scale deformation computed by the homogenization method to the full-scale response of FEM-based DNS by evaluating the absolute error. Fig. 5.4 shows a good match at most frequencies. Only at the frequencies 900 Hz and 1500 Hz the response computed by the homogenization method differs significantly from the full-scale analyis. The deviation on the global deformation at 900 Hz can be attributed to a structural resonance in the vicinity of the excitation frequency which is also visible in the frequency response in Fig.5.3. Only a small frequency shift might lead to a different response. As the frequency increases, the frequency shift becomes even more pronounced leading to larger deviations. This may explain the difference of the global response between the single-scale analysis and the full-scale analysis at 1500 Hz. Yet, it might also be possible that another structural resonance occurs at a frequency just beyond the range of interest. Nevertheless, from the preceding analysis it is safe to say that the homogenization method can accurately capture the dynamics of the rectangular finite LRAM plate.

5.3.2 Transient response

In Fig. 5.5 the out-of-plane displacement computed by the single-scale analysis at two gauge points is compared to the full-scale analysis. Once again, the red line indicates the homogenized response and the dashed blue line the full-scale response. The same sample frequencies used for the transient analysis are the same as those used for the steady-state analysis of the global deformation in the previous section.

A first look at the time-dependent displacement at both gauge-points indicates that after 3 periods, not any input excitation is fully attenuated. Even for the input signals with the frequency located inside the flexural wave band-gaps, full attenuation is not achieved. However, the response for both gauge points at frequencies 180 and 1270 Hz indicate that the input excitation is already attenuated due to the activated out-of-plane local eigenmodes.

Comparing the response of the enriched single-scale analysis to that of the full-scale analysis, shows that the first follows the latter within certain tolerance very well. Starting at the transient response for an input excitation of 100 Hz, it can be seen that the response of the finite plate follows the harmonic input-signal. Shifting to the transient response at 180 Hz, it can be seen that the out-of-plane deformation is attenuated somewhat, as could be expected. The same can be seen for the input-signal of 1270 Hz. Yet, from the previous analysis it was observed that the second flexural wave band-gap shows a stronger decay than the first one which seems to be reversed in this example. On the other hand, due to the limited length of the finite plate and the flexural wave bouncing back from the simply supported edge, the dynamic response of such structures is complicated. This emphasizes the need for transient simulations when evaluating the performance of LRAMs. As the frequency increases, the homogenized response seems to be somewhat stiffer than the full-scale response. This is expressed by the deviation between the output-signals of both methods as function of time.

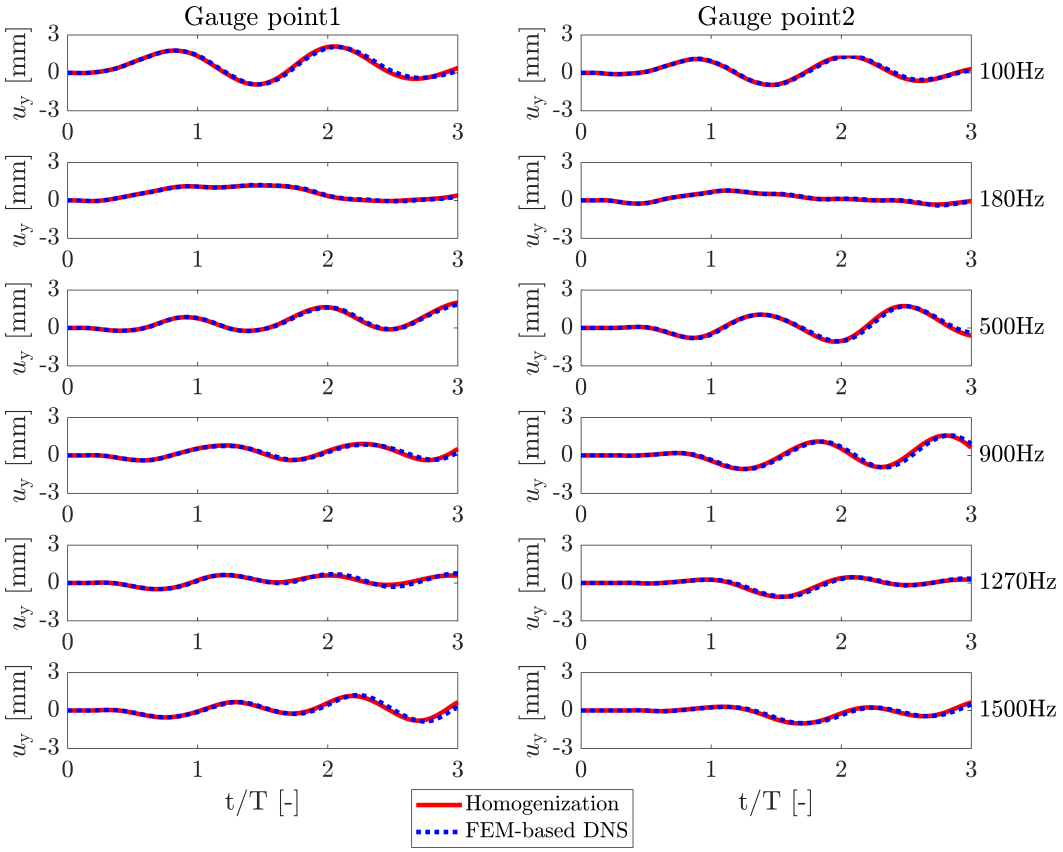

Figure 5.5: *Out-of-plane deformation of the finite LRAM plate subject to a transient input-signal at certain frequencies for the configuration of case-study I. Total simulation-time is* $t \in [0, 3T]$.

In Fig. 5.6 the global deformation of the LRAM plate is shown at $t = 3T$. Here the color-scale indicates the absolute deviation normalized by the input amplitude. Analysing the deformation it is even more convincing to say that the ingoing excitation is not yet fully attenuated. Nevertheless, the global response at 180 Hz and 1270 Hz already shows the attenuating performance of the LRAM plate. The deviation between the enriched single-scale analysis and the full-scale analysis is comparable to that of the steady-state response. Again for the excitation frequencies 900 Hz and 1500 Hz the deviation is largest. For the remaining excitation frequencies the deviation is relatively small compared to the input amplitude.

From this first case-study some primary conclusions on the validation of the homogenization framework can be drawn. The homogenization framework is able to capture both the local and the global response of LRAM plates. This is shown by the validation on both the gauge points and the global deformation. Moreover, the homogenization framework is able to capture the transient response of the finite LRAM plate. It can capture the attenuation effects with great accuracy with respect to the reference solution obtained from FEM-based DNS. The total simulation times of both methods will be compared at the end of this chapter. First, the macroscopic response corresponding to the configuration of case-study II is evaluated to get a complete validation of the homogenization framework on the finite LRAM plate.

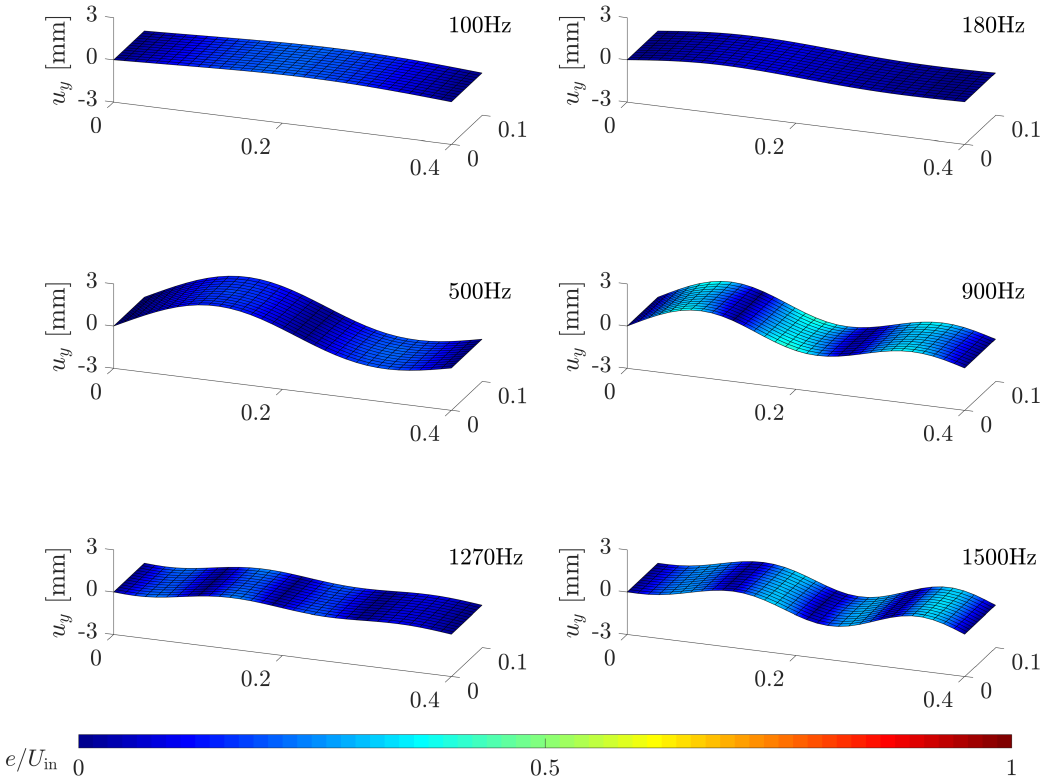

Figure 5.6: *Global transient deformation at several excitation frequencies computed by the homogenization method at time $t = 3T$. The color-scale indicates the absolute normalized deviation with respect to the reference solution.*

5.4 Case-study II

In the dispersion analysis it was figured out that the effective bending stiffness should be multiplied by a scaling factor δ to obtain the proper equivalent bending stiffness. Regarding the evaluation of the rectangular finite LRAM plate the influence of the scaling factor is not significant since the main propagation direction coincided with $\vec{e}_1^{\,\mathrm{c}}$. One should keep in mind however, that for case-study II this scaling factor will definitely be of influence on the response. The analysis of the square LRAM plate is equivalent to that of the rectangular plate. Thus, first the steady-state response is evaluated after which the transient response is analysed.

5.4.1 Steady-state response

In Fig. 5.7 the frequency response plots are shown at three gauge points at locations indicated in Tab. 5.2. The flexural wave band-gaps are indicated by the green-marked area. Comparing the response computed by the homogenization method (red line) to that of FEM-based DNS (blue line), a deviation is clearly visible at each gauge point. In the low-frequency regime, say 0-300 Hz, the deviation is negligible. However, in-between the two band-gaps the frequency shift becomes more pronounced. Approaching the second flexural wave band-gap, the deviation decreases again and within the band-gap it is negligible. Moving away

from the band-gap towards higher frequencies, the deviation increases again as expected from the previous analysis on the rectangular plate.

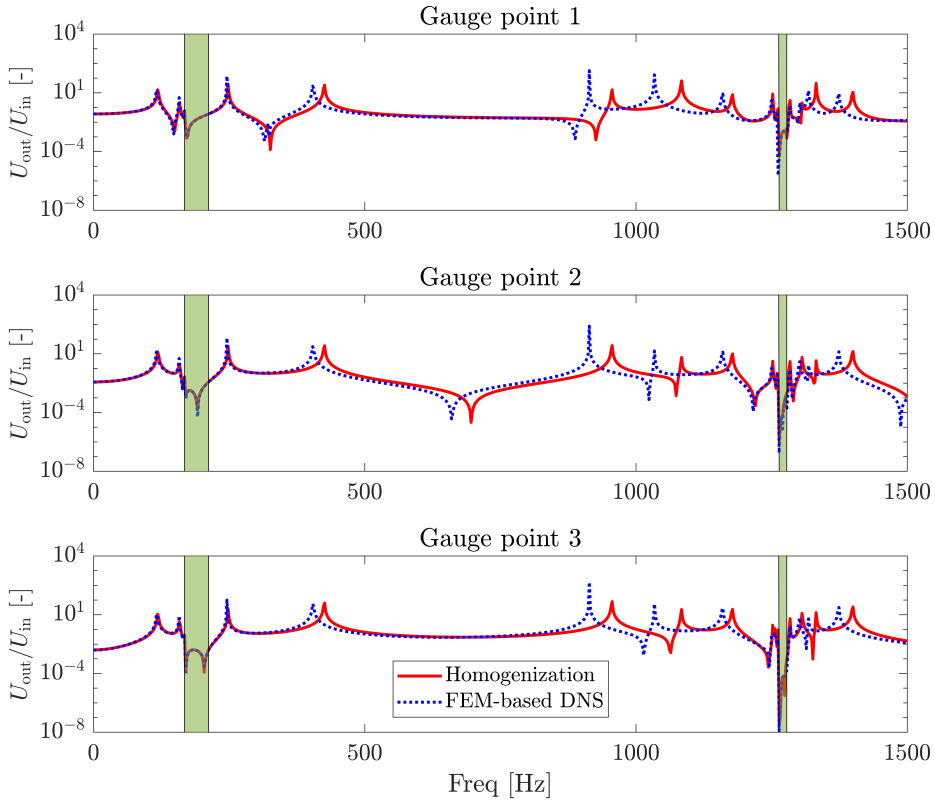

Figure 5.7: *Frequency response functions of the macroscopic out-of-plane displacement at three gauge points according to the configuration of case-study II.*

Evaluating the flexural wave band-gaps, a same fashion can be observed for different gauge points as for the rectangular plate. At gauge point 1 the first frequency band-gap is opened up at the expected frequency but it is closed almost immediately which makes it hardly visible. The second band-gap, on the other hand, is opened up over the full attenuation range and clearly visible. Proceeding to the frequency response at gauge point 2, the first band-gap is opened over a wider range and this can be attributed to the fact that it is located further from the excited corner. The third gauge point shows a stopping band which is almost as wide as the band-gap defined form the dispersion analysis. This is expected as this gauge point is located furthest from the excited corner. The second stopping band is captured well at each gauge point as was the case for the rectangular plate.

The deviation on the frequency looks worse than that for the rectangular plate, although it does not get higher than 5.1% within the evaluated range. The deviation may be caused by several phenomena. First of all, during the steady-state analysis on the rectangular plate, a deviation between the homogenization method and the reference solution was already observed with increasing frequency. This could be attributed to the fact that the transverse shear effects become more important at higher frequencies. For the square plate however, the scaling factor for the effective bending stiffness might be of influence. In Sec. 4.2.4 it could be seen that after application of the scaling factor, the flexural wave branch was still slightly over predicted. A third reason for the higher deviation is on the boundary

conditions applied to the plate. Since only one corner is excited instead of the entire edge, the wave will propagate in multiple directions simultaneously. This may result in multiple boundary reflections and a higher complexity of wave interferences. This is also shown in the frequency response plot as more resonance and anti-resonance peaks show up compared to the the rectangular plate, especially at higher frequencies. Taking all these possible causes into account, the deviation in the frequency response plots can be rationalized.

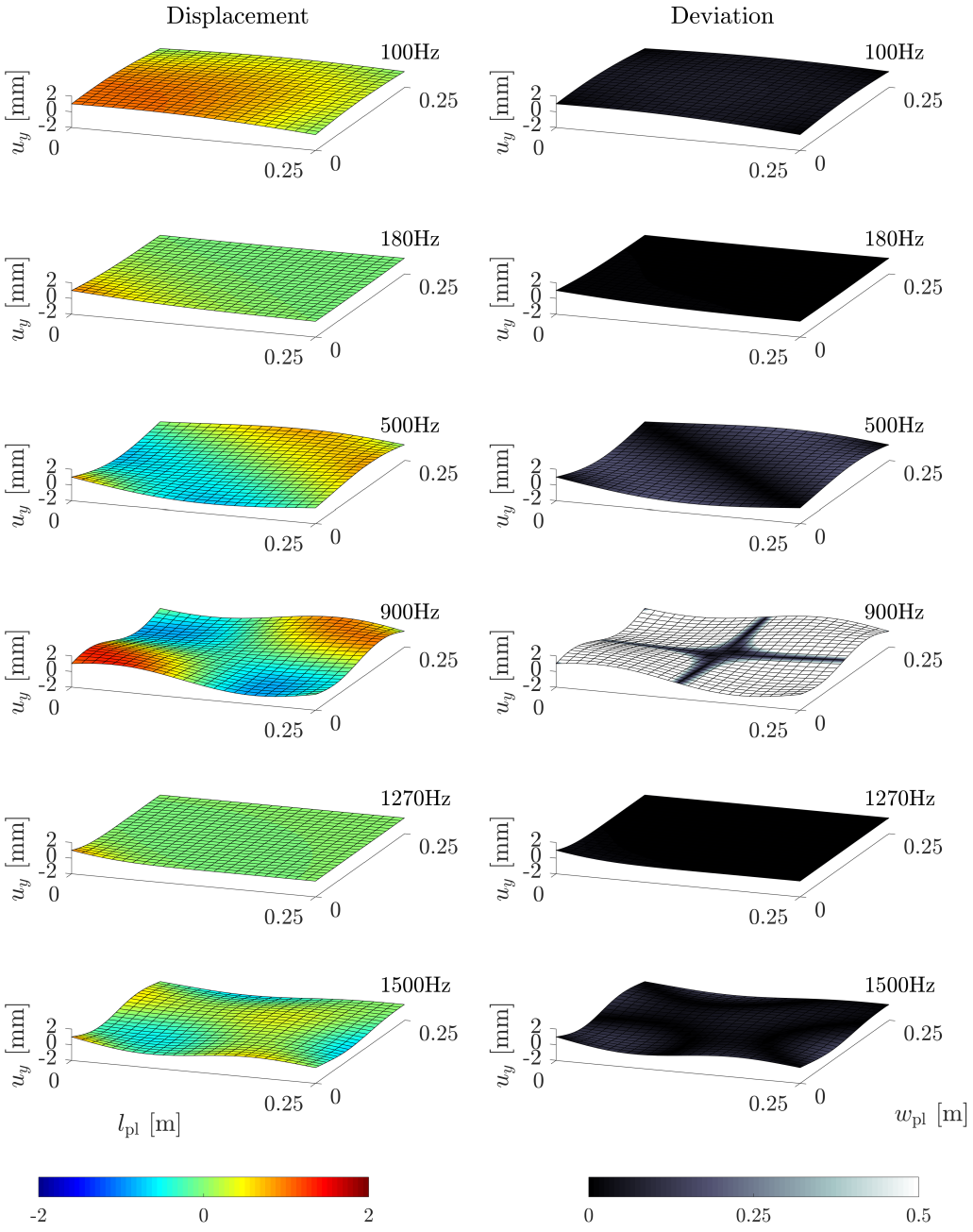

Figure 5.8: *Global steady state deformation at several excitation frequencies computed by the homogenization method. The color-scale at the left indicates the out-of-plane displacement and the color-scale at the right indicates the absolute normalized deviation with respect to the reference solution.*

In Fig. 5.8 the global deformation of the square LRAM plate at certain excitation frequencies computed by the homogenization method is shown. The deformation presented in the left and right column are both the result of the enriched single-scale analysis. However, the color-scale in both columns denote different quantities. The color-scale in the left column denotes the out-of-plane displacement of the square plate as the color-scale in the right column denotes the absolute normalized deviation. This error is defined the same as for the rectangular plate. Again, the deformation of the neutral plane of the full-scale analysis is used as a reference solution.

Looking at the left column, the corner excitation results in the global distortion for the frequencies located outside the stopping bands. For frequencies inside the band-gap the input excitation is attenuated. Again, the decaying effect for the excitation frequency of 1270 Hz is stronger than that of 180 Hz. This is also what was expected from the rectangular plate analysis and the frequency response plots in Fig. 5.8. The global deformation at each excitation frequency is symmetric along the diagonal of the plate as expected from the symmetry of the macroscopic configuration.

Shifting the scope of attention towards the deviation of the global deformation, two cases can be distinguished. Most deformed contours show good comparison to the reference solution indicated by the low deviation. However, for an excitation frequency of 900 Hz, the deviation is very large. Looking at the frequency response in Fig. 5.7, the reference solution shows a structural resonance at this frequency whereas the homogenized response shows this equivalent resonance peak at a higher frequency. This mismatch therefore results in the large deviation of the global deformation.

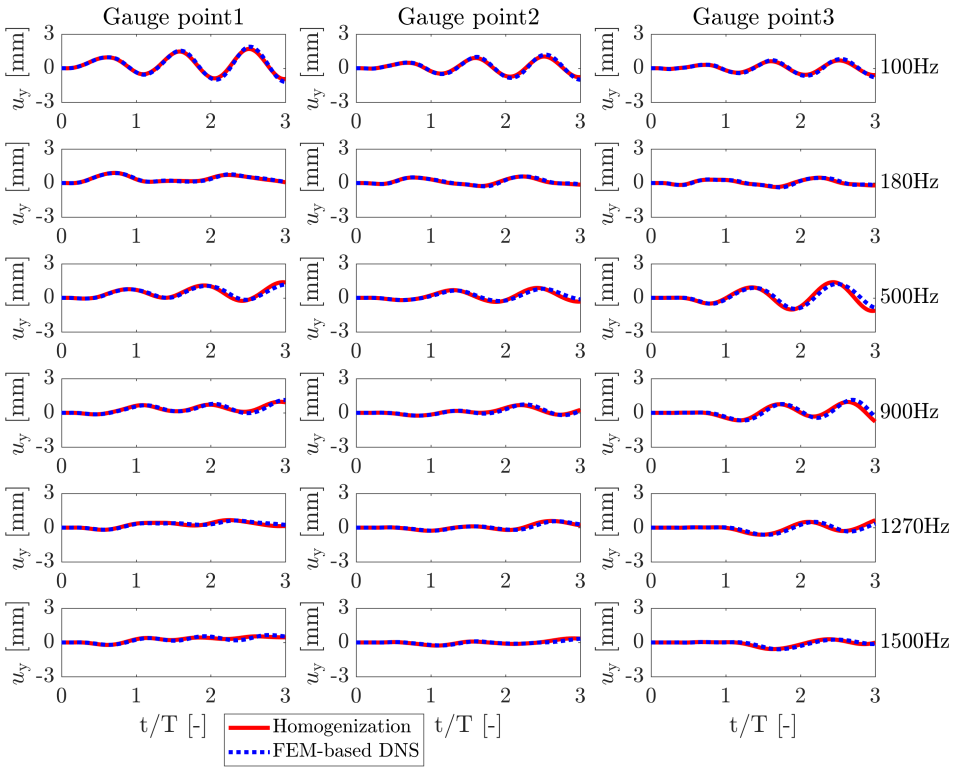

Figure 5.9: *Out-of-plane deformation according to the transient response of the finite LRAM plate at certain frequencies for the configuration of case-study II. Total simulation-time is* $t \in [0, 3T]$.

5.4.2 Transient response

To evaluate the transient response of the square plate, the same gauge points and frequencies are evaluated as for the steady-state response. The local transient response at the gauge points is displayed in Fig. 5.9. The homogenized response is denoted by the red line and the reference solution is denoted by the dashed blue line. Comparing the transient response between different gauge points shows a great variety for equal input frequency. This may again be attributed to multiple boundary effects and waves interfering from different directions simultaneously. This then results in a complex interference pattern. For the frequencies within the band-gaps an attenuating effect can be observed. However, for the frequency of 1500 Hz, the input excitation seems to be attenuated as well. Looking back at the frequency response plot in Fig. 5.7 and then especially at gauge point 2, a structural anti-resonance is observed near 1500 Hz. Off course, this anti-resonance will also lead to a decay, but this is not related to the activation of localized eigenmodes of the LRAM plate.

The transient response computed by the homogenization method seems to follow the reference solution very well for gauge points 1 and 2. At gauge point 3, the homogenized transient response is reacting overly stiff, especially for the input frequencies 500 Hz and 900 Hz. As argued before, this may be caused by several reasons among which the influence of the scaling factor is most obvious.

The global response of the square plate to a transient excitation at time $t = 3T$ is shown in Fig. 5.10. In the left column the color-scale denotes the out-of-plane displacement and in the right column the color-scale represents the absolute normalized deviation. From the global deformation plots it can be seen that the out-of-plane deformation of the plates at 180 Hz, 1270 Hz and 1500 Hz is not that very large. This strokes with the observations made on the local transient response in Fig. 5.9 and the frequency response in Fig. 5.7. For an excitation frequency of 500 Hz and 900 Hz, the out-of-plane deformation is much larger.

Focusing on the absolute deviation between the enriched single-scale analysis and the full-scale analysis, it is comparable to that for the rectangular plate. As for the steady-state global deformation, the global deformation for both 500 Hz and 900 Hz show the largest deviation. The deformation at 1270 Hz also shows a slight deviation in a particular area of the plate which strokes with Fig. 5.9. Nevertheless, a relatively good match exists between the response obtained form the homogenization method and that computed by FEM-based DNS.

With the evaluation of the square plate completed, the validation of the homogenization framework on the finite plate is complete. It can be concluded that for case-study I, the homogenization framework is able to accurately capture the dynamic response for both the steady-state and the transient analysis. Regarding case-study II, the homogenization framework can capture the dynamics relatively well although the deviation with respect to the reference solution is somewhat larger than for case-study I. Yet, the application of the scaling factor yields a better comparison to the reference. However, a further understanding on the over-constraint torsional stiffness is needed such that this cause of deviation can be omitted in further validations.

5.5 The ultimate comparison

The main motivation for the development of the homogenization framework is its advantage with respect to on-line computational costs compared to full-scale analysis. The enriched single-scale description only has to evaluate the micro-structure once in an off-line mode, drastically reducing the total number of DOFs and thereby the on-line computation time. The macroscopic configurations for case-study I and II are composed of 1197 and 2025 DOFs,

respectively. In this computation, both the displacement and emergent macroscopic degrees of freedom are taken into accounted. Comparing this to the full-scale analysis employed in FEM-based DNS with 2,079,027 and 3,245,427 DOFs respectively, the computational advantage is shown already.

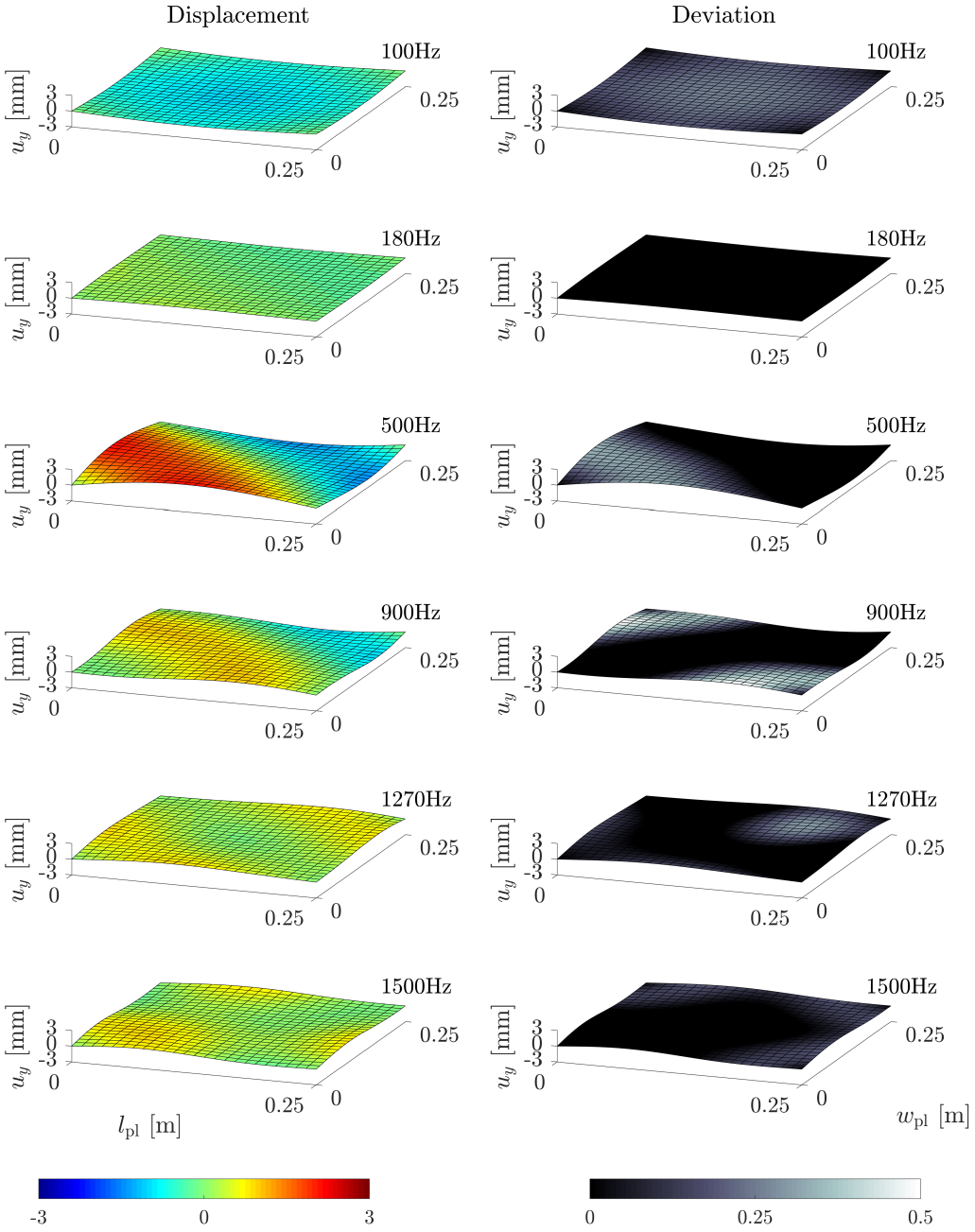

Figure 5.10: *Global transient deformation at 6 excitation frequencies computed by the homogenization method at time $t = 3T$. The color-scale at the left indicates the out-of-plane displacement and the color-scale at the right indicates the absolute normalized deviation with respect to the reference solution.*

For the sake of ultimate comparison, the computation times regarding the enriched

single-scale analysis and the full-scale analysis are shown in Tab. 5.3. The time for computing the transient analysis, is a summation over the times needed to calculate the response for each frequency. The computation times for the simulations performed by the homogenization method include the assembly of the stiffness and mass matrices as well as time needed for post-processing. Both the assembly and the post-processing are the dominating factor with respect to the total computation time. The times needed to merely compute either the frequency response or the transient response using the homogenization method is much lower than the values in Tab. 5.3. However, the gain displayed in the table already shows the great potential of the homogenization framework.

Method	**Software**	**Study**	**Case-study I**		**Case-study II**	
			Time [s]	*Gain*	*Time [s]*	*Gain*
Homogenization	Matlab v.2014b	SS	2981	44	6179	41
		TR	850	55	2308	33
FEM-based DNS	COMSOL v5.3	SS	130710	-	253128	-
		TR	46803	-	75835	-

Table 5.3: *Computation times for the macroscopic analyses.*

Chapter 6

From validation to application

In Chaps. 4 and 5 the homogenization framework was validated on an infinite and finite LRAM plate. It could be concluded that the framework is able to capture the local and global dynamic response accurately. After the completion of the validation of the homogenization framework flat LRAM plates, it might be interesting to look at a more general excitation subjected to a finite LRAM plate. To this extent, a general input-signal is applied to the plate and the dynamic response will be analysed.

6.1 Case study

6.1.1 Gauss pulse

A clean harmonic signal as was used in the transient analysis in Section 5 will hardly ever occur in real-life applications. Often structural vibrations can be represented by a summation of multiple harmonic waves of different frequencies and amplitudes. To show the strength of the homogenization framework, a simple LRAM plate can be subjected to a general input signal composed of multiple frequencies. The input signal which is subjected to the plate is composed of multiple Gauss-pulses.

A Gauss pulse is composed of a standard Gaussian function and multiplied by a harmonic signal. By multiplying the harmonic signal with the Gaussian function, the single frequency signal becomes a singal containing multiple frequencies. The input signal can therefore be defined as

$$u_{\text{in}}(t) = U_{\text{amp}} \cos[2\pi f_{\text{c}}(t - t_0)] e^{-\frac{1}{4} f_{\text{c}}^2 (t-t_0)^2} \tag{6.1}$$

with U_{in} the amplitude, f_{c} the center-frequency, $t \in [0, (N-1)\Delta t]$ the time with Δt the time step and t_0 the time to center the input signal. The frequency f_{c} in the Gauss pulse denotes the frequency with the highest magnitude in the pulse and it is positioned at time $t = t_0$. To evaluate the frequencies that appear in this signal, the signal can be transformed into the frequency domain by applying the discrete Fourier transform (DFT). With the discrete Fourier transform the signal that is defined at a certain number of samples N in the time-interval $t \in [0, (N-1)\Delta t]$ can be transformed into a signal defined over a certain frequency-interval. This is written as

$$U_{\text{in}}(n) = \sum_{k=1}^{N} u_{\text{in}}(k) e^{\frac{i2\pi}{N} kn} \tag{6.2}$$

where N denotes the number of samples in the time-domain, n a sample in the frequency domain, k a sample in the time domain and U_{in} is the transformed quantity of the input

signal u_{in}. Then for a Gaussian input signal for certain center frequency f_{c}, the Fourier transform can be obtained to evaluate the magnitude of all frequencies of which the signal is composed. In Fig. 6.1 a Gaussian input signal and the corresponding DFT is shown. The signal is padded with zeros to get a smoother DFT out of the signal. This is due to the fact that the transformed quantity is only defined over the number of samples N in the time-domain.

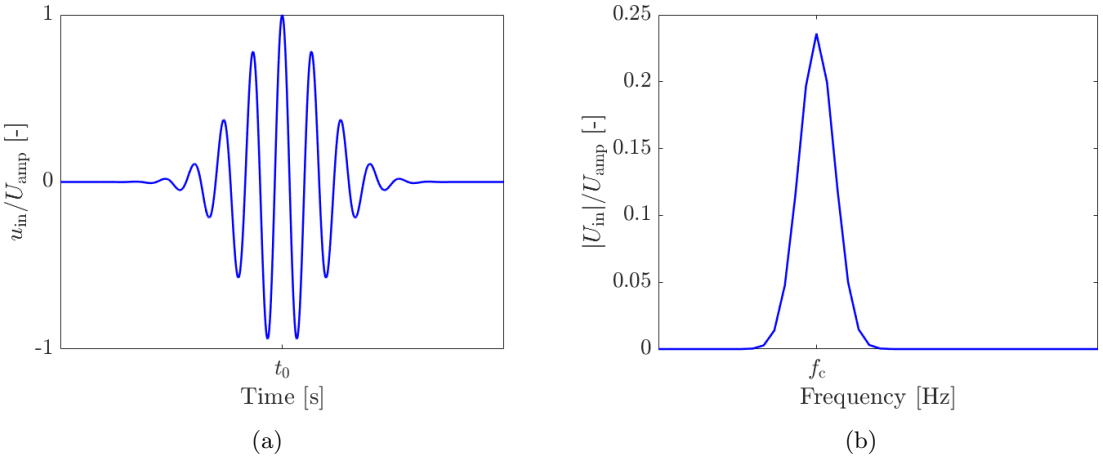

Figure 6.1: *Gaussian input signal (a) and its Fourier transform (b).*

6.1.2 Simulation set-up

Pulse-train

The input signal subjected to the finite LRAM plate can be composed of multiple Gaussian pulses forming a pulse-train. The pulse train consists of multiple center frequencies which will show up as separate peaks in the magnitude plot of the DFT. To show the attenuation performance of the LRAM plate, a pulse-train with multiple frequencies is subjected to the plate. It is expected that the frequencies located inside the frequency band-gaps are attenuated and will not show up in the DFT (or with lower magnitude), while frequencies outside these band-gaps still show up. During the validation of the framework, the unit-cell configuration in Fig. 4.1 was embedded in the finite LRAM plate. This particular unit-cell design shows two distinct flexural wave band-gaps. Therefore, the same unit-cell configuration is used in this application since the locations of the band-gaps are known. The pulse-train subjected to the finite LRAM plate consists of two Gaussian pulses with the center frequency inside the first and the second, respectively, and one frequency in-between the two band-gaps such that $f_{\text{c}} = \{180, 500, 1270\}$. The input signal and its DFT are shown in Fig. 6.2. The signal is composed of $N = 7949$ samples.

Macroscopic configuration

During the validation of the homogenization framework, the enormous amount of DOFs in the full-scale analysis led to a restriction on the macroscopic dimensions of the finite LRAM plate. However, for the current application the response will not be verified to a full-scale analysis. Therefore the in-plane macroscopic dimensions of the LRAM plate are increased to emphasize the strength of the homogenization framework.

Two case-studies are introduced to show the potential of the homogenization frame-

work. Both show some resemblance to the case-studies employed in Chap. 5 and are shown in Fig. 6.3.

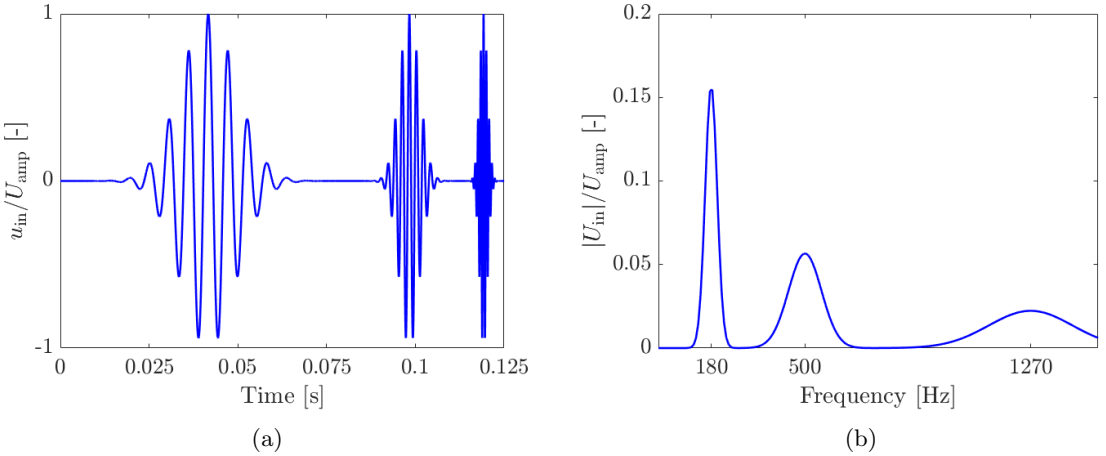

Figure 6.2: *Pulse-train composed of three Gaussian pulses (a) and its discrete Fourier transform (b).*

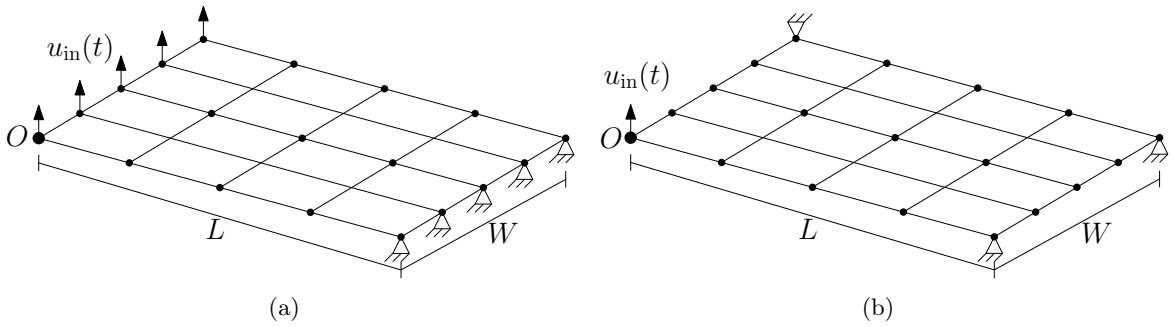

Figure 6.3: *Macroscopic configuration for case-study I (a) and case-study II (b).*

For case-study I, a rectangular LRAM plate composed of 60x10 unit-cells is used. One short edge of the plate is simply supported and the other short edge is subjected to an out-of-plane excitation following the displacement of the pulse-train in Fig. 6.2(a). The two remaining long edges and the top and bottom of the plate remain free. The number of isogeometric elements used to discretize the plate is equal to 24 in the long direction of the plate and 4 elements in the short direction. Taking into account both the macroscopic and emergent degrees of freedom, the discretized LRAM plate is composed of a total number of 1701 DOFs. For case-study II, a rectangular LRAM plate composed of 50x30 unit-cells is employed. Here, one corner is subjected to the out-of-plane excitation according to the pulse-train. The three remaining corners are simply supported and all edges and the top and bottom surface remain free. To discretize the LRAM plate, 20 isogeometric elements are used in the long direction and 12 elements in the short direction. A summation over the macroscopic and emergent degrees of freedom results in a total of 3105 DOFs. The B-spline basis functions and the control mesh are defined according to eq. (5.8). Since an out-of-plane excitation is applied to either one edge or one corner, it is valid to take into account only those local resonance modes that were also used in the validation on the finite LRAM plate. Hence local resonance modes $n = \{1, 5, 6, 7, 12, 13\}$ are implemented in the macroscopic configuration. The

most important information on the macroscopic configurations for the two case studies is summarized in Tab. 6.1.

To compute the DFT of the out-of-plane displacement of the plate, three gauge points are defined for both case-studies. At these gauge points the out-of-plane displacement is measured along the full time domain. The coordinates of the gauge points for the corresponding case-study are mentioned in Tab. 6.1. The locations of these gauge points is measured from the origin defined at the corner of the plate.

Quantity	**Unit**	**Case-study I**	**Case-study II**
L	[mm]	600	500
W	[mm]	100	300
H	[mm]	5	5
# elements $\vec{e}_1^{\mathfrak{c}}$	[-]	24	20
# elements $\vec{e}_3^{\mathfrak{c}}$	[-]	4	12
# DOFs	[-]	1701	3105
GP 1	[mm]	(100,50)	(200,10)
GP 2	[mm]	(300,50)	(200,20)
GP 3	[mm]	(500,50)	(400,10)
GP 4	[mm]	-	(400,20)

Table 6.1: *Details on the macroscopic configurations.*

This case-study shows the strength of the homogenization framework if one compares the macroscopic configurations employed in the homogenization method to those employed in the full-scale analysis. Regarding case-study I, the full-scale plate could be discretized within reasonable time as it has approximately the same number of DOFs as the square plate employed in Chap. 5. However, if one wanted to perform the transient analysis for the pulse-train this would be a cumbersome and computational expensive task. The transient simulation for the full-scale analysis of the square plate in Sec. 5.4 consisted of 400 time-steps and it almost took 4 hours to compute the response to only one input frequency. Taking into account the number of samples of which the pulse-train is composed ($N = 7494$) one could imagine that it is hardly feasible to perform this task at the full-scale. Regarding case-study II, the number of unit-cells in a full-scale configuration is 2.5 times as high as for case-study I. If one would succeed to discretize the plate, solving the time-dependent problem would take days.

6.2 Results

To assess the attenuation performance of the LRAM plate, the discrete Fourier transform is performed on the transverse displacement of at the gauge points mentioned in Tab. 6.1. In Fig. 6.4 the DFT-spectra are shown for the input signal, the gauge points of case-study I and the gauge points of case-study II, respectively. The frequency band-gaps obtained form the early dispersion analysis in Chap. 4 are marked in the figures by the green areas.

From the DFT-spectrum of the input signal, it is observed that the center frequency of two Gaussian pulses is indeed located inside the frequency band-gaps. The magnitude plot of the Gauss pulse with center frequency at 180 Hz is almost entirely located inside the first band-gap. Regarding the Gauss-pulse at 1270 Hz, only part of the magnitude spectrum is located inside the second band-gap. Firstly, the magnitude-plot for case-study I is analysed. It is observed that the magnitude at each gauge point for nearly all frequencies is lower

compared to the input signal. As expected, the input signal is attenuated inside the first band-gap due to the activated local eigenmodes coupling with the out-of-plane displacement of the plate. Interesting is the fact that for frequencies just outside the band-gap hardly any attenuation is visible. Shifting the scope of attention towards the second band-gap, the same trends can be seen with respect to the attenuation of the out-of-plane displacement. Moreover, the attenuation of the input signal is strongest for gauge point 3 which makes sense as it is located furthest form the input excitation. The Gauss pulse at 500 Hz shows a rather mixed image. At the right-hand side of the center frequency, the input signal seems to be somewhat attenuated while this is not the case at the left-hand side. This may be due to the fact that the Gauss pulse at 180 Hz might interfere with the Gauss-pulse at 500 Hz leading to the mixed response.

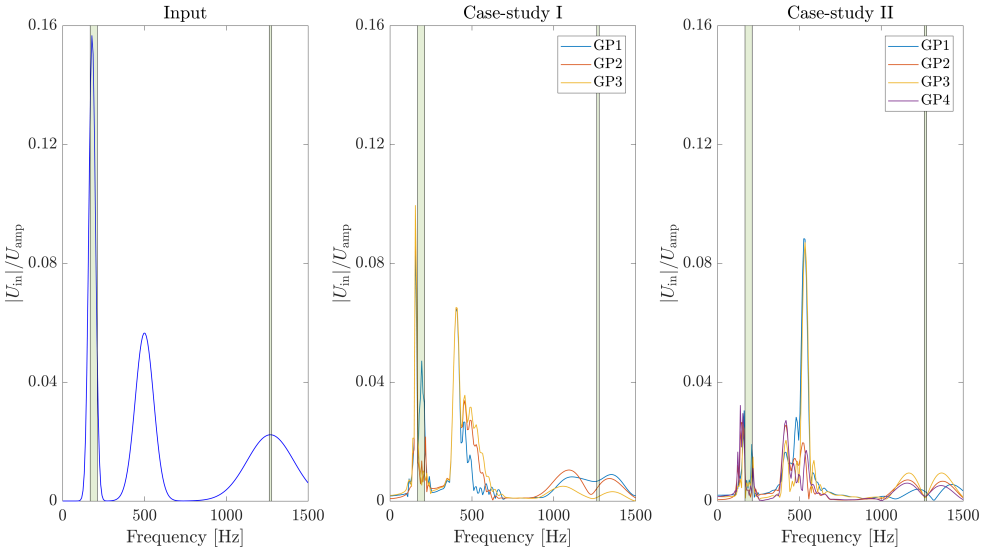

Figure 6.4: *Magnitude of the DFT-spectra for the out-of-plane displacement at the input and at the gauge points for the corresponding case-studies.*

Taking a look at the magnitude plot for case-study II, similar trends are observed as for the first case-study. The wave attenuation seems to be more effective in the first and second flexural wave band-gap compared to case-study I. The strongest attenuation is observed for the gauge point located furthest from the input excitation.

The computation times for case-study I and case-study II are 2689 [s] and 16631 [s], respectively. Although these times seem large, it must be emphasized that the transient analysis was performed at 7949 time steps. From both case-studies it can be concluded that the homogenization framework can capture the attenuating performance of the LRAM plates well within reasonable computational time.

Chapter 7

Conclusions and recommendations

This thesis presented the implementation and validation of the dynamic computational homogenization framework developed in [29] for flat LRAM plates. Moreover, its application potential towards more complicated cases was also demonstrated, through analyzing a finite LRAM plate of large macroscopic dimensions, excited by a multi-frequency input signal.

With respect to the infinite flat LRAM plate, the homogenization method yielded a great agreement with the reference solution, for studying the wave propagation in the principal directions. For the wave propagation in-between the principal directions a good match between homogenization method and FEM-based DNS still hold, through introducing a scaling factor on torsion-related terms in the effective bending stiffness matrix. This was found necessary to compensate for the overestimated torsion stiffness, which is hypothesized as being induced by inappropriate selection of unit-cell geometry such that the lamina-level periodic boundary conditions lead to over-constraint effects. Similar trends are investigated in the validation on a finite LRAM plate as well, where the macroscopic boundary effects further play a role on influencing the accuracy of the homogenization method. In all, when the seperation of scales holds, the homogenization method is able to provide satisfactory accuracy, compared to FEM-based DNS.

In aspect of computational cost, the homogenization method displays a great potential, especially for LRAM structures of large macroscopic dimensions composed of complex unit-cells. This was confirmed in the final study, where a time-dependent vibration was further considered for generality. The transient response of the plate was indeed determined in a reasonable cheap fashion, while the attenuating performance of the finite plate was captured accurately.

A few recommendations for future work are made below.

- Further understanding on the overestimated torsion stiffness from the homogenization method, together with a systematic way to determine its scaling factor.
- Validations on more complex unit-cell designs employing e.g. negative effective stiffness effects as well as double-negative effects.
- Validations on more complex macroscopic configurations e.g. curved shell structures and other resemble real-life applications.
- Validation on thin plates or structures composed of multiple materials e.g. a mixture of normal materials and metamaterials.

Bibliography

[1] Euro Composites. Glass Fiber Honeycomb. URL: `https://www.euro-composites.com/en/glasfaser-wabe`. 2013. Accessed 6-February-2019.

[2] T. Yildiz. Design and analysis of a lightweight composite shipping container made of carbon fiber laminates. *Logistics*, 3, 18, 2019.

[3] Osaka Japon. Maritime Museum. URL: `http://www.hda-paris.com/project/maritime-museum-osaka-japon/`. Accessed 17-August-2019.

[4] Visitez Liège. Gare de Guillemins. URL: `https://www.visitezliege.be/nl/gare-des-guillemins`. Accessed 17-August-2019.

[5] F. Fahy and P. Gardonio. Sound and structural vibration. *Academic Press*, January 2007.

[6] L. Cveticanin, M. Zukovic and D. Cveticanin. On the elastic metamaterial with negative effective mass. *Journal of Sound and Vibration*, 436:295-309, 2018.

[7] H.H. Huang, C.T. Sun and G.L. Huang. On the negative effective mass density in acoustic metamaterials. *International Journal of Engineering Science*, 47(4):610-617, 2009.

[8] M. Oudich, Y. Li, B.M. Assouar and Z. Hou. A sonic band gap based on the locally resonant phononic plates with stubs. *New Journal of Physics*, 12:083049, 2010.

[9] V.E. Gusev and O.B. Wright. Double-negative flexural acoustic metamaterial. *New Journal of Physics*, 16, 2014.

[10] Z. Li, C. Wang and X. Wang. Modelling of elastic metamaterials with negative mass and modulus based on translational resonance. *International Journal of Solids and Structures*, 17:40, 2018.

[11] X. Zhou, X. Liu and G. Hu. Elastic metamaterials with local resonances: an overview. *Theoretical & Applied Mechanics Letters 2*, 041001, 2012.

[12] B.Xia, N. Chen, L. Xie, Y. Qin and D. Yu. Temperture-controlled tunable acoustic metamaterial with active band gap and negative bulk modulus. *Applied Acoustics*, 112:1-9, 2019.

[13] H. Tian, X. Wang and Y. Zhou. Theoretical model and analytical approach for a circular membrane-ring structure of locally resonant acoustic metamaterial. *Applied Physics A*, 114:985-990, 2014.

[14] Y. Zhang, J. Wen, Y. Xiao, X. Wen and J. Wang. Theoretical investigation of the sound attenuation of membrane-type acoustic metamaterials. *Physics Letters A*, 376: 1489-1494, 2012.

[15] X. Zhou and G. Hu. Analytic model of elastic metamaterials with local resonances. *Physical review B*, 79:195109, 2009.

[16] A. Natgehi, L. van Belle, C. Claeys, E. Deckers, B. Pluymers and W. Desmet. Wave propagation in locally resonant cylindrically curved metamaterial panels. *International Journal of Mechanical Sciences*, 127:73-90, 2017.

[17] S. Yeh and R.L. Harne. Tailoring concurrent shear and translational vibration control mechanisms in elastomeric metamaterials for cylindrical structures. *Mechanical Systems and Signal Processing*, 117:609-633, 2019.

[18] C. Sugino, S. Leadenham, M. Ruzzene and A. Erturk. On the mechanism of bandgap formation in locally resonant finite elastic metamaterial. *Journal of Applied Physics*, 120:134501, 2016.

[19] D. Beli, J.R.F. Arruda and M. Ruzzene. Wave propagation in elastic metamaterial beams and plates with interconnected resonators. *International Journal of Solids and Structures*, 139-140:105-120, 2018.

[20] S. Zouari, J. Brocail and J.M. Génevaux. Flexural wave band gaps in metamaterial plates: A numerical and experimental study form infinite to finite models. *Journal of Sound and Vibration*, 435:246-263, 2018.

[21] J. He and H. Huang. Complete vibrational bandgap in thin elastic metamaterial plates with periodically slot-embedded local resonators. *Archive of Applied Mechanics*, 88:1263-1274, 2018.

[22] J. Zhao, Y. Li and W.M. Liu. Predicting band structure of 3D mechanical metamatrials with complex geometry via XFEM. *Computational Mechanics*, 55: 659-672, 2015.

[23] H. Peng and P.F. Pai. Acoustic metamaterial plates for elastic wave absorption and structural vibration suppression. *International Journal of Mechanics Sciences*, 89:350-361, 2014.

[24] Y. Xiao, J. Wen, D. Yu and X. Wen. Flexural wave propagation in beams with periodically attached vibration absorbers: Band-gap behavior and band formation mechanisms. *Journal of Sound and Vibration*, 332: 867-893, 2013.

[25] Y. Xiao, J. Wen and X. Wen. Flexural wave band gaps in locally resonant thin plates with periodically attached spring-mass resonators. *Journal of Physics D: Applied Physics*, 45:195401, 2012.

[26] K. Pham, V.G. Kouznetsova and M.G.D Geers. Transient computational homogenization for heterogeneous materials under dynamic excitation. *Journal of the Mechanics and Physics of Solids*, 61:2125-2146, 2013.

[27] D. Roca, D. Yago, J. Canter, O. Lloberas-Valls and J. Oliver. Computational design of locally resonant acoustic metamaterials. *Computer Methods in Applied Mechanics and Engineering*, 345:161-182, 2019.

[28] D. Roca, O. Lloberas-Valls, J. Cante and J. Oliver. A computational multiscale homogenization framework accounting for inertial effects: Application to acoustic metamaterials modelling. *Computer Methods in Applied Mechanics and Engineering*, 330:415-446, 2018.

[29] L. Liu, A. Sridhar, M.G.D. Geers and V.G. Kouznetsova. Computational homogenization of locally resonant acoustic metamaterial panels towards enriched continuum beam/shell description, Sept 2019.

[30] E.W.C. Coenen, V.G. Kouznetsova and M.G.D. Geers. Computational homogenization for heterogeneous thin sheets. *International Journal for Numerical Methods in Engineering*, 83:1180-1205, 2010.

[31] A. Sridhar, V.G. Kouznetsova and M.G.D. Geers. Homogenization of locally resonant acoustic metamaterials towards an emergent enriched continuum. *Computational Mechanics*, 57:423-435, 2016.

[32] E.J.P. Miranda, E.D. Nobrega, A.H.R. Ferreira and J.M.C. Dos Santos. Flexural wave band gaps in a multi-resonator elastic metamaterial plate using Kirchoff-Love theory. *Mechanical Systems and Signal Processing*, 116:480-504, 2019.

[33] V. Kouznetsova, M.G.D Geers and W.A.M. Brekelmans. Size of a representative volume element in a second-order computational homogenization framework. *International Journal for Multiscale Computational Engineering*, 2(4):575-598,2004.

[34] R. Hill. Elastic properties of reinforced solids: some theoretical principles. *Journal of the Mechanics and Physics and Solids*, 11:357-372, 1963.

[35] R. Craig and M. Bampton. Coupling of substructures for dynamic analyses. *AIAA Journal, American Institute of Aeronautics and Astronautics*, 6:1313-1319, 1968.

[36] A. Sridhar, L. Liu, V.G. Kouznetsova and M.G.D. Geers. Homogenized enriched continuum analysis of acoustic metamaterials with negative stiffness and double negative effects. *Journal of the Mechanics and Physics of Solids*, 119:104-117, 2018.

[37] A. Sridhar, V.G. Kouznetsova and M.G.D. Geers. A semi-analytical approach towards plane wave analysis of local resonance metamaterial using a multiscale enriched continuum description. *International Journal of Mechanical Sciences*, 133:188-198, 2017.

[38] F. Farzbod and M.J. Leamy. Analysis of Bloch's method and the propagation technique in periodic structures. *Journal of Vibration and Acoustics*, 133,2011

[39] I.A. Veres, T. Berer and O. Matsuda. Complex band structures of two dimensional phononic crystals: Analysis by the finite element method. *Journal of Applied Physics*, 114,083519,2013.

[40] A. Makishima and J.D. Mackenzie. Calculation of bulk modulus, shear modulus and poisson's ratio of glass. *Journal of Non-Crystalline Solids*, 17:147-157,1975.

[41] A. Markidou, W.Y. Shih and W.H. Shih. Soft-materials elastic and shear moduli measurement using piezoelectric cantilevers. *Review of Scientific Instruments*, 76:064302,2005.

[42] A.O. Krushynska, V.G. Kouznetsova and M.G.D. Geers. Towards optimal design of locally resonant acoustic metamaterials. *Journal of the Mechanics and Physics of Solids*, 71:179-196,2014.

[43] D.J. Benson, Y. Bazilevs, E. de Luycker, M.C. Hsu, M. Scott, T.J.R. Hughes and T. Belytschko. A generalized finite element formulation for arbitrary basis functions: From isogeometric analysis to XFEM. *International Journal for Numerical Methods in Engineering*, 83:765-785, 2010.

[44] J.A. Cottrell, A. Reali, Y. Bazilevs and T.J.R. Hughes. Isogeometric analysis of structural vibrations. *Computer Methods in Applied Mechanics and Engineering*, 195:5257-5296, 2006.

[45] C.V. Verhoosel and K.G. van der Zee. Advanced discretization techniques.

Appendix A

Applying the Bloch-Floquet boundary conditions to the continuum shell

A.1 Bloch-Floquet theorem

The Bloch-Floquet theorem can be applied to an infinite 3D continuous medium that is build up by periodic unit-cells. Then any point in this infinite medium can be expressed in terms of the corresponding point in the reference unit-cell and a complex phase shift. The phase shift is related to the distance between the reference unit-cell and to be analysed point in the medium. The Bloch-Floquet boundary conditions can be adjusted to apply the theorem to the continuum shell description. In the continuum shell, the waves can not propagate in the out-of-plane direction. Consider Fig. A.1 where the Bloch-Floquet theorem for a shell is illustrated. The displacement of point p in the infinite shell can be expressed in terms of the corresponding point u in the reference unit-cell and a phase shift as

$$\vec{u}_{\mathrm{m,p}} = \vec{u}_{\mathrm{m},0} e^{i\hat{\vec{k}} \cdot (\hat{\vec{x}}_{\mathrm{m,p}} - \hat{\vec{x}}_{\mathrm{m},0})} \tag{A.1}$$

where $\vec{u}_{\mathrm{m,p}}$ and $\vec{u}_{\mathrm{m},0}$ denote the displacement of point p and the displacement of the corresponding point in the reference unit-cell [16].

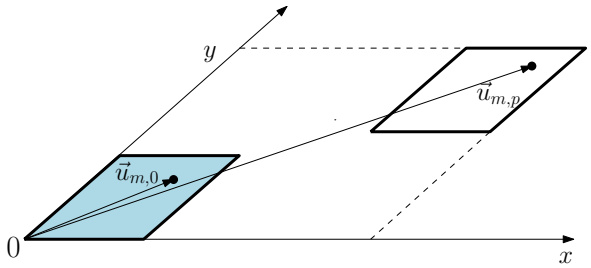

Figure A.1: *Illustration of the modified Bloch-Floquet boundary conditions.*

Applying the plane-wave transformation (eq. (4.4)) and eq. (A.1) to the discrete microscopic balance of linear momentum (eq. (3.2)), the dispersion analysis of the reference unit-cell can be written as as

$$[\underline{\mathbb{B}}_{\mathrm{m}} - \omega^2 \underline{\mathbb{W}}_{\mathrm{m}}] \cdot \underset{\sim}{\vec{u}}_{\mathrm{m,tr}} = \underset{\sim}{\vec{f}}_{\mathrm{m,tr}} \tag{A.2}$$

The lamina-level Bloch-Floquet boundary conditions are correspondingly written as

$$\vec{u}_{\mathrm{m}}^{+} = \vec{u}_{\mathrm{m}}^{-} e^{i\hat{\vec{k}} \cdot (\hat{\vec{x}}_{\mathrm{m}}^{+} - \hat{\vec{x}}_{\mathrm{m}}^{+})} \tag{A.3}$$

where the superscripts $(\bullet)^{+}$, $(\bullet)^{-}$ denote transverse in-plane boundaries of the unit-cell employed in Fig. 4.1(a).

Through application of eq. (A.3) a tying constraint between the independent and dependent transverse boundaries is defined. Collecting all tying constraints in a tying matrix $\underline{\Gamma}_{\mathrm{m,di}}$, the dependent nodes are tied to the independent nodes as

$$\underset{\sim}{\vec{u}}_{\mathrm{m,d}} = \underline{\Gamma}_{\mathrm{m,di}} \underset{\sim}{\vec{u}}_{\mathrm{m,i}} \tag{A.4}$$

where the subscripts $(\bullet)_{\mathrm{i,d}}$ denote the independent and dependent nodes respectively. Eq. (A.4) is alternately substituted into eq. (A.2) and partitioned into dependent and independent nodes. One will then end up with the $\omega(\vec{k})$-form eigenvalue problem under the modified Bloch-Floquet boundary conditions as

$$\left[\underline{\mathbb{B}}_{\mathrm{m}}^{\omega(\vec{k})} - \omega^2 \underline{\mathbb{W}}_{\mathrm{m}}^{\omega(\vec{k})} \right] \cdot \underset{\sim}{\vec{u}}_{\mathrm{m,i,tr}}^{\omega(\vec{k})} = \underset{\sim}{\vec{0}}_{\mathrm{m,i,tr}}^{\omega(\vec{k})} \tag{A.5}$$

Solving the $\omega(\vec{k})$-form eigenvalue problem, yields the frequency response of the infinite shell to a certain wavetype. Through the application of the tying matrix $\underline{\Gamma}$, the eigenvalue-problem can be easily solved by implementing it in a standard FEM framework. This is what makes the Bloch Analysis a straightforward verification method.

Appendix B

Generalized system finite panel analysis

The discretized system of equations represented in eq. (5.4) is partitioned into a few sub-matrices and -columns. This exercise was performed to split the macroscopic and emergent displacement fields. The sub-matrices and columns are shown individually in eq. (5.5). For clarification, the components in this equation are described separately in terms of the effective unit-cell properties.

B.1 Generalized stiffness matrix

The generalized stiffness matrix $\underline{\mathcal{B}}_{\mathrm{M}}$ is composed of two components. The component $\underline{\mathcal{B}}_{\mathrm{M},uu}$ is related to the macroscopic displacement field and $\underline{\mathcal{B}}_{\mathrm{M},\zeta\zeta,nn}$ is related to the emergent displacement field. They are defined in eq. (B.1)-(B.2). The top left entry in eq. (B.1) is related to the in-plane macroscopic displacement field and the bottom right entry is related to the out-of-plane macroscopic displacement field. The entries in eq. (B.2) are related to the emergent displacement field.

$$\underline{\mathcal{B}}_{\mathrm{M},uu} = \begin{bmatrix} \underline{\hat{\mathcal{B}}}_{\mathrm{M},uu} & \underline{\mathbb{O}} \\ \underline{\mathbb{O}} & \underline{\tilde{\mathcal{B}}}_{\mathrm{M},uu} \end{bmatrix} \tag{B.1a}$$

$$\underline{\hat{\mathcal{B}}}_{\mathrm{M},uu} = \int_{\mathcal{A}_{\mathrm{M,r}}} \left[\hat{\nabla}_{\mathrm{M}} \underset{\sim}{R}_{\mathrm{M}} \right] \cdot {}^{4}\mathbb{C}^{\mathrm{mm}}_{\mathrm{M}} \cdot \left[\hat{\nabla}_{\mathrm{M}} \underset{\sim}{R}_{\mathrm{M}} \right]^{\mathrm{T}} \mathrm{d}A_{\mathrm{M}} \tag{B.1b}$$

$$\underline{\tilde{\mathcal{B}}}_{\mathrm{M},uu} = \int_{\mathcal{A}_{\mathrm{M,r}}} \tilde{\vec{e}}^{\,\mathrm{c}} \left[\hat{\boldsymbol{\Delta}}_{\mathrm{M}} \underset{\sim}{R}_{\mathrm{M}} \right] : {}^{4}\mathbb{C}^{\mathrm{bb}}_{\mathrm{M}} : \left[\hat{\boldsymbol{\Delta}}_{\mathrm{M}} \underset{\sim}{R}_{\mathrm{M}} \right]^{\mathrm{T}} \tilde{\vec{e}}^{\,\mathrm{c}} \mathrm{d}A_{\mathrm{M}} \tag{B.1c}$$

$$\underline{\mathcal{B}}_{\mathrm{M},\zeta\zeta,nn} = \int_{\mathcal{A}_{\mathrm{M,r}}} \underset{\sim}{R}_{\mathrm{M}} \omega_n^2 \underset{\sim}{R}_{\mathrm{M}}^{\mathrm{T}} \mathrm{d}A_{\mathrm{M}} \tag{B.2}$$

B.2 Generalized mass matrix

Compared to the generalized stiffness matrix, the generalized mass matrix $\underline{\mathcal{W}}_{\mathrm{M}}$ is composed of four components. The component $\underline{\mathcal{B}}_{\mathrm{M},uu}$ is related to the macroscopic displacement field and $\underline{\mathcal{B}}_{\mathrm{M},\zeta\zeta,nn}$ is related to the emergent displacement field. The components $\underline{\mathcal{B}}_{\mathrm{M},u\zeta,n}$ and $\underline{\mathcal{B}}_{\mathrm{M},\zeta u,n}$ define the coupling between the macroscopic and emergent degrees of freedom. They are defined in eq. (B.3)-(B.6). The top left entry in eq. (B.3) is related to the in-plane

macroscopic displacement field and the bottom right entry is related to the out-of-plane macroscopic displacement field. The entries in eq. (B.4) are related to the emergent displacement field. The entries in eq. (B.5) represent the coupling between the two fields.

$$\underline{\underline{\mathcal{W}}}_{\mathrm{M},uu} = \begin{bmatrix} \underline{\underline{\hat{\mathcal{W}}}}_{\mathrm{M},uu} & \underline{\underline{\mathbb{O}}} \\ \underline{\underline{\mathbb{O}}} & \underline{\underline{\tilde{\mathcal{W}}}}_{\mathrm{M},uu} \end{bmatrix} \tag{B.3a}$$

$$\underline{\underline{\hat{\mathcal{W}}}}_{\mathrm{M},uu} = \int_{\mathcal{A}_{\mathrm{M,r}}} \left[\hat{\vec{\nabla}}_{\mathrm{M}} \underset{\sim}{R}_{\mathrm{M}} \right] \cdot {}^{4}\mathbb{D}^{\mathrm{ll}}_{\mathrm{M}} \cdot \left[\hat{\vec{\nabla}}_{\mathrm{M}} \underset{\sim}{R}_{\mathrm{M}} \right]^{\mathrm{T}} \mathrm{d}A_{\mathrm{M}} + \int_{\mathcal{A}_{\mathrm{M,r}}} \underset{\sim}{R}_{\mathrm{M}} \hat{\boldsymbol{\rho}}^{\,\mathrm{ll}}_{\mathrm{M}} \underset{\sim}{R}^{\mathrm{T}}_{\mathrm{M}} \mathrm{d}A_{\mathrm{M}} \tag{B.3b}$$

$$\underline{\underline{\tilde{\mathcal{W}}}}_{\mathrm{M},uu} = \int_{\mathcal{A}_{\mathrm{M,r}}} \tilde{\vec{e}}^{\,\mathrm{c}} \left[\hat{\boldsymbol{\Delta}}_{\mathrm{M}} \underset{\sim}{R}_{\mathrm{M}} \right] : {}^{4}\mathbb{D}^{\mathrm{rr}}_{\mathrm{M}} : \left[\hat{\boldsymbol{\Delta}}_{\mathrm{M}} \underset{\sim}{R}_{\mathrm{M}} \right]^{\mathrm{T}} \tilde{\vec{e}}^{\,\mathrm{c}} \mathrm{d}A_{\mathrm{M}} + \int_{\mathcal{A}_{\mathrm{M,r}}} \underset{\sim}{R}_{\mathrm{M}} \tilde{\boldsymbol{\rho}}^{\,\mathrm{ll}}_{\mathrm{M}} \underset{\sim}{R}^{\mathrm{T}}_{\mathrm{M}} \mathrm{d}A_{\mathrm{M}} \tag{B.3c}$$

$$\underline{\underline{\mathcal{W}}}_{\mathrm{M},\zeta\zeta,nn} = \int_{\mathcal{A}_{\mathrm{M,r}}} \underset{\sim}{R}_{\mathrm{M}} \underset{\sim}{R}^{\mathrm{T}}_{\mathrm{M}} \mathrm{d}A_{\mathrm{M}} \tag{B.4}$$

$$\underline{\mathcal{W}}_{\mathrm{M},u\zeta,n} = \frac{1}{A_{\mathrm{M,r}}} \begin{bmatrix} \underline{\hat{\mathcal{W}}}_{\mathrm{M},u\zeta,n} \\ \underline{\tilde{\mathcal{W}}}_{\mathrm{M},u\zeta,n} \end{bmatrix} \tag{B.5a}$$

$$\underline{\hat{\mathcal{W}}}_{\mathrm{M},u\zeta,n} = \int_{\mathcal{A}_{\mathrm{M,r}}} \left[\hat{\vec{\nabla}}_{\mathrm{M}} \underset{\sim}{R}_{\mathrm{M}} \right] \cdot \boldsymbol{h}^{\mathrm{lm}}_{n} \underset{\sim}{R}^{\mathrm{T}}_{\mathrm{M}} \mathrm{d}A_{\mathrm{M}} + \int_{\mathcal{A}_{\mathrm{M,r}}} \underset{\sim}{R}_{\mathrm{M}} \hat{\vec{j}}^{\,\mathrm{lm}}_{n} \underset{\sim}{R}^{\mathrm{T}}_{\mathrm{M}} \mathrm{d}A_{\mathrm{M}} \tag{B.5b}$$

$$\underline{\tilde{\mathcal{W}}}_{\mathrm{M},u\zeta,n} = -\int_{\mathcal{A}_{\mathrm{M,r}}} \tilde{\vec{e}}^{\,\mathrm{c}} \left[\hat{\boldsymbol{\Delta}}_{\mathrm{M}} \underset{\sim}{R}_{\mathrm{M}} \right] : \boldsymbol{h}^{\mathrm{rt}}_{n} : \underset{\sim}{R}^{\mathrm{T}}_{\mathrm{M}} \mathrm{d}A_{\mathrm{M}} + \int_{\mathcal{A}_{\mathrm{M,r}}} \underset{\sim}{R}_{\mathrm{M}} \tilde{\vec{j}}^{\,\mathrm{lm}}_{n} \underset{\sim}{R}^{\mathrm{T}}_{\mathrm{M}} \mathrm{d}A_{\mathrm{M}} \tag{B.5c}$$

$$\underline{\mathcal{W}}_{\mathrm{M},\zeta u,n} = A_{\mathrm{M,r}} \underline{\mathcal{W}}^{\mathrm{T}}_{\mathrm{M},u\zeta,n} \tag{B.6}$$

B.3 Generalized force column

The generalized force column is shown in eq. (B.7).

$$\underset{\sim}{\mathcal{F}}_{\mathrm{M},u} = \begin{bmatrix} \hat{\mathcal{F}}_{\mathrm{M},u} \\ \tilde{\mathcal{F}}_{\mathrm{M},u} \end{bmatrix} \tag{B.7a}$$

$$\underset{\sim}{\hat{\mathcal{F}}}_{\mathrm{M}} = \int_{\mathcal{C}_{\mathrm{M,r},t}} \underset{\sim}{R}_{\mathrm{M}} \hat{\vec{t}}_{\,\mathrm{M}} \mathrm{d}C_{\mathrm{M}} \tag{B.7b}$$

$$\underset{\sim}{\tilde{\mathcal{F}}}_{\mathrm{M}} = \int_{\mathcal{C}_{\mathrm{M,r},t}} \underset{\sim}{R}_{\mathrm{M}} \tilde{\vec{t}}_{\,\mathrm{M}} \mathrm{d}C_{\mathrm{M}} - \int_{\mathcal{C}_{\mathrm{M,r},m}} \tilde{\vec{e}}^{\,\mathrm{c}} \left[\hat{\vec{\nabla}}_{\mathrm{M}} \underset{\sim}{R}_{\mathrm{M}} \right] \cdot \hat{\vec{m}}_{\,\mathrm{M}} \mathrm{d}C_{\mathrm{M}} \tag{B.7c}$$

Obviously, no external forces act on the emergent degrees of freedom. Therefore, $\underset{\sim}{\mathcal{F}}_{\mathrm{M},\zeta,\mathrm{n}} = \underline{0}$.

B.4 Generalized displacement column

The generalized displacement column is shown in eq. (B.8).

$$\underset{\sim}{\mathcal{U}}_{\mathrm{M,u}} = \begin{bmatrix} \hat{\vec{u}}_{\,\mathrm{M}} \\ \tilde{\vec{u}}_{\,\mathrm{M}} \end{bmatrix} \tag{B.8a}$$

$$\underset{\sim}{\mathcal{U}}_{\mathrm{M},\zeta,n} = \underset{\sim}{\kappa}_{n} \tag{B.8b}$$